

**DEVELOPMENT OF A COMPREHENSIVE MAGNETOHYDRODYNAMIC
MODEL OF SOLAR-TERRESTRIAL INTERACTION**

by

**Stephen S. Stahara, Richard R. Rachlele,
Gregory A. Molvik, and John R. Spreiter**

AD-A222 612

FINAL REPORT

AFOSR Contract No. F49620-86-C-0035

December 1988

**DTIC
ELECTE
MAY 30 1990
S B D**

prepared for

**Air Force Office of Scientific Research
Bolling AFB, D.C.**

RMA Aerospace, Inc.

**883 North Shoreline Blvd., Suite B200, Mountain View, CA 94043
Telephone (415) 961-0560**

DISTRIBUTION STATEMENT A
**Approved for public release
Distribution Unlimited**

REPORT DOCUMENTATION PAGE

Form Approved
OMB No. 0704-0188

Public reporting burden for this collection of information is estimated to average 1 hour per response, including the time for reviewing instructions, searching existing data sources, gathering and maintaining the data needed, and completing and reviewing the collection of information. Send comments regarding this burden estimate or any other aspect of this collection of information, including suggestions for reducing this burden, to Washington Headquarters Services, Directorate for Information Operations and Reports, 1215 Jefferson Davis Highway, Suite 1204, Arlington, VA 22202-4302, and to the Office of Management and Budget, Paperwork Reduction Project (0704-0188), Washington, DC 20503.

1. AGENCY USE ONLY (Leave blank) 2. REPORT DATE: December 1988 3. REPORT TYPE AND DATES COVERED: Final Report/1 Mar 86-30 Sep 88

4. TITLE AND SUBTITLE
Development Of A Comprehensive Magnetohydrodynamic Model of Solar-Terrestrial Interaction

5. FUNDING NUMBERS
61102F/2311/A1

6. AUTHOR(S)
Stephen S. Stahara

7. PERFORMING ORGANIZATION NAME(S) AND ADDRESS(ES)
RMA Aerospace, Inc.
883 North Shoreline Blvd., Suite B200
Mountain View, CA 94043

8. PERFORMING ORGANIZATION REPORT NUMBER
APOSR-TR-90-0534

9. SPONSORING/MONITORING AGENCY NAME(S) AND ADDRESS(ES)
AFOSR/NP Bldg 416
Bolling AFB DC 20332-6448

10. SPONSORING/MONITORING AGENCY REPORT NUMBER
F49620-86-C-0035

11. SUPPLEMENTARY NOTES

12a. DISTRIBUTION/AVAILABILITY STATEMENT
Approved for public release; distribution is unlimited.

12b. DISTRIBUTION CODE

13. ABSTRACT (Maximum 200 words)
The work relates to the preliminary development of a comprehensive, multi-level, 3-D magnetohydrodynamic model that seeks to describe the detailed, global interaction of the solar wind plasma and magnetic field with the Earth's geospace. The development of five separate advanced computational submodels of the complete interaction model involves approximately 42,000 lines of fortran source code. These submodels provide the capability for quantitatively simulating a variety of steady and unsteady phenomena associated with the solar wind-terrestrial environment interaction process to a degree previously unattainable. A number of these new developments have been incorporated into a core interaction submodel that can be structured to work in both a rapid warning mode for spacecraft protection as well as in a detailed scientific analysis mode for fundamental studies. The other submodels developed either simulate similar phenomena of the solar wind-terrestrial environment interaction process as the core interaction submodel but at a higher level of simulation accuracy or simulate additional interaction phenomena.

14. SUBJECT TERMS
sun, magnetosphere, interaction

15. NUMBER OF PAGES
108

16. PRICE CODE

17. SECURITY CLASSIFICATION OF REPORT
UNCLASSIFIED

18. SECURITY CLASSIFICATION OF THIS PAGE
UNCLASSIFIED

19. SECURITY CLASSIFICATION OF ABSTRACT
UNCLASSIFIED

20. LIMITATION OF ABSTRACT
UL
SAR

DEVELOPMENT OF A COMPREHENSIVE MAGNETOHYDRODYNAMIC
MODEL OF SOLAR-TERRESTRIAL INTERACTION

by

Stephen S. Stahara, Richard R. Rachiele,
Gregory A. Molvik, and John R. Spreiter

FINAL REPORT

RMA TR 0103

DECEMBER 1988

Prepared Under Contract No. F49620-86-C-0035

for

Air Force Office of Scientific Research
Bolling AFB, D. C. 20332-6448

by

RMA Aerospace, Inc.
883 North Shoreline Blvd., Suite B200
Mountain View, CA 94043
(415) 961-0560

TABLE OF CONTENTS

	PAGE
1. EXECUTIVE SUMMARY	1
2. INTRODUCTION	2
3. TECHNICAL OVERVIEW	4
3.1 Overview of Solar-Terrestrial System	4
3.2 Global Interaction Submodels of Total Interaction Model	5
4. SUMMARY OF GLOBAL INTERACTION MODEL DEVELOPMENTS	7
4.1 Development of Core Interaction Model	7
4.2 Development of Full 3-D Interaction Model	16
4.3 Development of Aligned Flow Full MHD Interaction Model	19
4.4 Development of Continuous Flow Transient Interaction Model	21
4.5 Development of Discontinuous Flow Transient Interaction Model	23
5. PRESENTATIONS AND PUBLICATIONS	27
REFERENCES	29
APPENDIX-COPIES OF PUBLICATIONS	30



Accession For	
NTIS GRA&I	<input checked="" type="checkbox"/>
DTIC TAB	<input type="checkbox"/>
Unannounced	<input type="checkbox"/>
Justification	
By _____	
Distribution/	
Availability Codes	
Dist	Avail and/or Special
A-1	

DEVELOPMENT OF A COMPREHENSIVE MAGNETOHYDRODYNAMIC MODEL OF SOLAR-TERRESTRIAL INTERACTION

1. EXECUTIVE SUMMARY

A final summary report is provided of the work performed under AFOSR Contract No. F49620-86-C-0035. The work under this contract relates to the preliminary development of a comprehensive, multi-level, 3-D magnetohydrodynamic model that seeks to describe the detailed, global interaction of the solar wind plasma and magnetic field with the Earth's geospace. The overall technical objective of the present work is the development of a model capable of quantitatively describing and routinely predicting many of the most important space plasma and field phenomena associated with the interaction of the solar wind plasma with the terrestrial environment. The ultimate importance of such a model for Air Force missions in the Earth's geospace lies in its capability to function as an accurate and reliable predictor of the solar-terrestrial plasma weather and, most importantly, its ability to rapidly warn of impending major changes.

Because of the complexity of such solutions and the detail required, the methodology for such a model must necessarily be computational. In the current work, we have successfully accomplished the development of five separate advanced computational submodels of the complete interaction model involving approximately 42,000 lines of fortran source code. These submodels in total provide the capability for quantitatively simulating a variety of steady and unsteady phenomena associated with the solar wind-terrestrial environment interaction process to a degree previously unattainable. A number of these new developments have been incorporated into a core interaction submodel that can be structured to work in both a rapid warning mode for spacecraft protection as well as in a detailed scientific analysis mode for fundamental studies. The other submodels developed either simulate similar phenomena of the solar wind-terrestrial environment interaction process as the core interaction submodel but at a higher level of simulation accuracy or simulate additional interaction phenomena.

All of the important results from the research performed under this contract have been reported in the open literature, both in scientific archival journals and as technical papers at scientific meetings with appropriate acknowledgement of AFOSR support. This report provides a synopsis of all the model developments accomplished, a summary of the important research results, a reference list of the publications and presentations resulting from the research, and copies of all the publications.

2. INTRODUCTION

The space era has provided great advances in the understanding of the many and varied phenomena involved in solar terrestrial physics, in particular, those involving plasma and magnetic fields of solar origin. With the numerous manned and unmanned Air Force missions currently being planned for the near-Earth space environment, the need has become quite evident for procedures to describe and predict plasma and field phenomena associated with the coupled solar-interplanetary medium-terrestrial environment system. Essentially all of these future space missions will require a reliable on-going forecast of solar-terrestrial plasma "weather" and warning of impending major changes, both for better utilization of observational opportunities as well as for the safety and protection of spacecraft. In addition, many important terrestrial-based activities such as communications and other atmospheric dependent applications are also strongly affected by high levels of solar plasma and magnetic field activity. As the space station and associated space activities are initiated in the near future, the need for such a capability will become even more critical.

Although there have been numerous and significant advances in our ability to predict various segments of the coupled solar-interplanetary medium-terrestrial environment system, the overall quantitative predictive capability presently remains limited and disjointed. While there currently are numerous models, some highly quantitative and verified by comparisons with observations, that deal with various components of the total system, these models normally exist as separate entities and have not been unified with others to any significant degree. Additionally, even fewer models deal with their component processes with the generality required to make the prediction usually desired, particularly with respect to transient phenomena.

Additionally and perhaps of most importance, the major advancements that have been achieved in fluid dynamic computational methods in the past 15 years have not been applied to any significant degree to space physics problems. Because most of the important problems associated with the solar-terrestrial environment interaction concern plasma phenomena that are complex, interrelated, and time-dependent, and because the solutions for these phenomena require both a fine detail for resolution as well as a global extent, the ultimate solution methods must necessarily be computationally based. A primary objective of this study has been the introduction of new and advanced computational development and numerical modeling to a variety of detailed and advanced aspects of the 3-D solar-terrestrial interaction system. A unique feature of our model is that certain segments contain a hierarchy of computational submodels for solving the same plasma physics problem but at different accuracy-of-simulation levels. This multi-level hierarchy enables use of our model in at least two different modes: (1) a rapid analysis mode necessary for use in a warning or preliminary analyses capability, and (2) a detailed analysis mode for use in in-depth scientific studies. This feature enables accurate simulation of a variety of complex nonlinear field and plasma phenomena, while simultaneously providing the means to control the potentially prohibitive computer

costs associated with detailed studies of 3-D solar-terrestrial phenomena.

During this phase of the investigation, we have successfully developed several completely new computational submodels for simulating different aspects of the solar wind interaction problem. In addition, we have also developed a number of significant extensions and enhancements to our previously-developed solar wind/terrestrial interaction model (Refs. 1-3). These developments, taken in total, now allow us to quantitatively predict details of the plasma and field properties associated with a variety of interaction phenomena, both steady and unsteady, to a degree of accuracy and routineness that was heretofore unachievable. These modeling developments, which are described in detail in the following sections, have been incorporated into a core interaction model that even at this preliminary stage of development establishes a comprehensive, practical, user-oriented, working model for ourselves and other interested space scientists to study various aspects of the global 3-D solar wind/terrestrial interaction.

3. TECHNICAL OVERVIEW

3.1 Overview of Solar-Terrestrial System

The physical foundation of the ideas, morphology and methodology underlying the current development program is illustrated in Figure 1 below, where the three primary segments of the coupled solar-terrestrial system are identified:

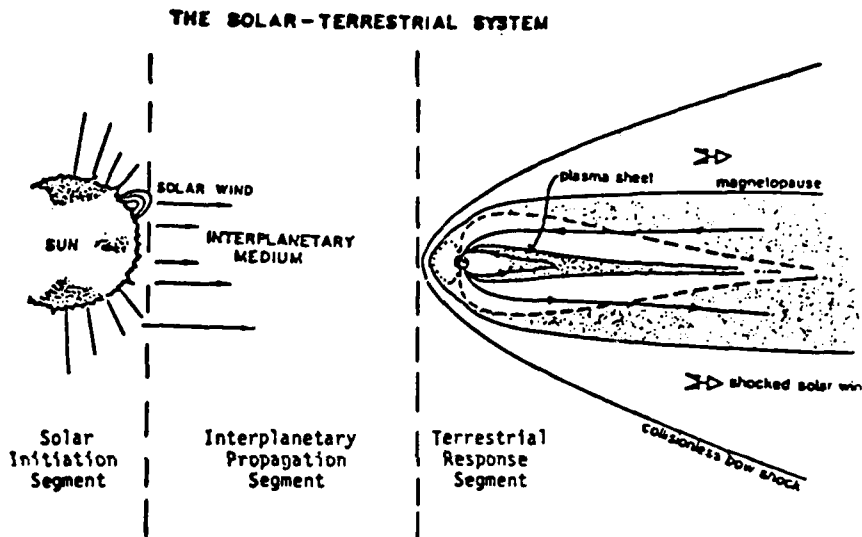


Figure 1. Illustration of the Three Primary Segments of the Coupled Solar-Terrestrial System

The outer layers of the sun are a convection heat engine that produce both large- and small-scale hydromagnetic motions on the solar surface. This activity at the solar surface creates the first segment of the solar-terrestrial system by generating the solar wind--the underlying medium that couples the solar-terrestrial system. The solar wind itself arises from the hydromagnetic motions on the solar surface which provide a complex magnetic topology from which the heated solar plasma ultimately escapes into interplanetary space. The solar wind plasma thus created carries a portion of the solar magnetic field as it subsequently flows from the solar corona out into the solar system. The solar wind itself is a supersonic, super-Alfvénic, strongly ionized plasma that transports plasma, energy, angular momentum, and magnetic field from the sun past all the planets of the solar system. The second segment of the solar-terrestrial system is the interplanetary propagation segment. It involves the transport through the solar wind media of both steady and quasi-steady processes commonly occurring in the solar wind, as well as the propagation of high energy transient

phenomena such as solar flare initiated disturbances. This segment initiates at the solar corona and and, for our purposes, ends in the near-vicinity of the Earth's geospace. The final segment of the coupled solar-terrestrial system is the terrestrial response segment. This segment involves the global interaction and subsequent response of the Earth's environment to both the steady state and transient plasma and field phenomena that have been transported and modified by the solar wind plasma from the surface of the sun, through the interplanetary medium, and finally impact on the Earth's geospace.

Each of the three segments encompasses varied and complex plasma and magnetic field phenomena, and each in itself actually represents an important subdiscipline of solar-system plasma physics. The ultimate predictive capability for the coupled solar-terrestrial system will involve detailed predictive models for all three segments integrated with each other and coupled with simultaneous observational input data provided by multiple spacecraft in the environments of the near-sun, interplanetary space, and near-Earth. The focus for the current study is on the terrestrial response segment and represents the logical first step in achieving the complete predictive capability for the sun-terrestrial system. The initiating input data for the interaction models developed here is assumed to be provided by one or more monitoring spacecraft located some distance upstream of the Earth toward the sun. That observational data is then projected via use of the interaction model to predict plasma and field properties from the spacecraft monitor location through the bow shock and magnetosheath region down to the terrestrial magnetopause boundary.

3.2 Global Interaction Submodels of Total Interaction Model

Because of the many and varied plasma and field phenomena that we intend to describe, it is neither convenient nor efficient for the terrestrial interaction model to be composed of a single, large, all-encompassing computational element. We have chosen instead to configure the total model as a modularized assemblage of individual submodels that are linked together to form the complete interaction model. In addition to this modularization, we have also intentionally constructed the model to contain a hierarchy of different accuracy-of-simulation levels and associated computational algorithms in order to simulate, when necessary and at the appropriate level of simulation accuracy, specific plasma and magnetic field phenomena associated with the global solar wind-terrestrial magneosphere interaction process.

In broad summary, the investigation completed here has resulted in a comprehensive interaction model in preliminary form that provides, on a single-fluid continuum rather than multi-component particle basis, a quantitative three-dimensional description of the spatially and temporally varying properties of the plasma and magnetic fields that link the near-Earth interplanetary medium with the terrestrial magnetopause. The complete interaction model is capable of predicting the global plasma and magnetic field properties associated with the transport of the interplanetary solar wind plasma from an arbitrary location of a spacecraft monitor placed upstream of the terrestrial bow

shock to and through the bow shock and intervening magnetosheath region and down to the magnetopause boundary. The model consists of several distinct but interactive modules that quantitatively predict various steady and dynamic aspects of the interaction. The model employs advanced computational procedures, many of which are of recent development.

In a conceptual but directly realizable operational mode, the entire model calculation can be configured to be carried out at a pace that is at least two orders of magnitude faster than the actual physical events evolve in space. We view such an operational mode of the final interaction model as a pilot system capable of providing a solar-terrestrial plasma weather prediction service analogous partly to the global weather forecasting system, and partly to the Pacific Ocean tsunami warning system. The complete implementation of the prediction and warning mode of the model will require that the interplanetary inputs be continually monitored and provided in an on-line mode to the interaction model. Both the slowly varying pseudo-steady state of the interplanetary medium and the propagation of disturbances through it can then be simulated and routinely and accurately predicted via use of the interaction model.

In order to realize such a quantitative predictive capability of the global interaction process, we have proceeded in this contract to both extend previously existing interaction submodels and to develop entirely new interaction submodels. The effort has involved the successful development and implementation of several important extensions in the submodel that we have termed the basic or core interaction model, in particular the prediction of time-dependent dynamic processes involving the interplanetary magnetic field. In addition, we have successfully developed a number of new interaction submodels. During this contract effort, four completely new computational submodels have been developed which provide predictive capabilities beyond the basic core interaction model. Each of these new submodels employs different advanced numerical algorithms, and solves in detail a different aspect of the solar wind-terrestrial environment interaction problem. These new interaction submodels are:

- 3-D steady flow interaction model
- Aligned flow full MHD interaction model
- Continuous flow transient interaction model
- Discontinuous flow transient interaction model

The developments associated with these new submodels as well as those of the core interaction model are discussed in detail in the following section.

4. SUMMARY OF INTERACTION MODEL DEVELOPMENTS

4.1 Development of Core Interaction Model

Central to the predictive model being developed here is the submodel that we have termed the core interaction model. The core interaction model represents the basic or first-order computational model of the complete multi-level interaction model for predicting the global 3-D interaction of the solar wind with the Earth's magnetosphere. For the current program, the core model provides the fundamental computational tool for determining the detailed plasma and field properties in the magnetosheath region between the Earth's bow shock and magnetopause.

The theoretical and computational basis of the current model is described in detail in Refs. 1-3. Here we present only some salient features of the model convenient for the present discussion. The fundamental assumption of the model is that the bulk properties of solar wind flow past planetary magnetopause obstacles can be adequately described by solutions of the continuum equations of magnetohydrodynamics for a single-component perfect gas having infinite electrical conductivity and zero viscosity and thermal conductivity. The governing equations express the conservation of mass, momentum, energy, and magnetic field, augmented by jump conditions appropriate for a fast shock wave and a tangential discontinuity at, respectively, the bow shock wave and magnetopause surface. The model determines the magnetopause and bow shock locations and the magnetosheath plasma and field properties. Justification of the theoretical basis rests primarily on the outstanding agreement between results calculated in this way and observations made in space for the Earth and other planets over the past 25 years. This basis is now well established.

The basic or core interaction model does not solve the general unsteady 3-D MHD equations but a simplified subset based on:

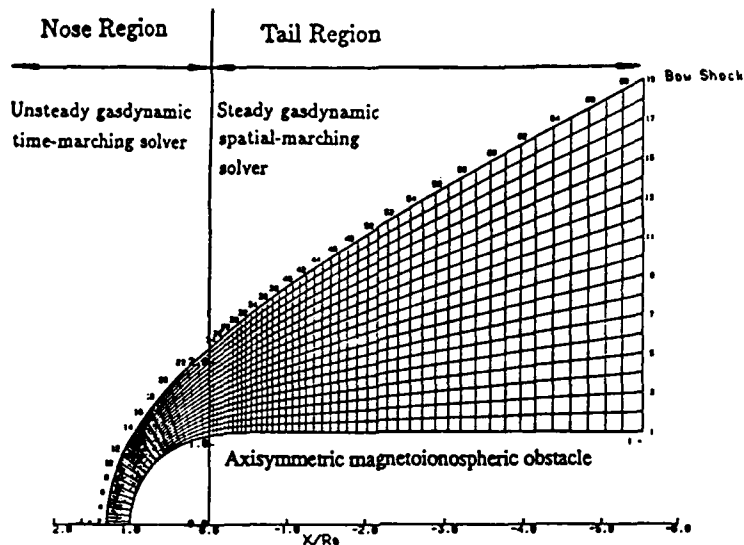
- steady flow
- predetermined magnetopause obstacle
- high Alfvénic Mach number

The last assumption, typical of solar wind flows past the planets, results in the magnetic terms in the momentum and energy equations being significantly smaller than the gas dynamic terms. This implies that the solution for the fluid motion can be decoupled from the magnetic field. The simplified equations governing the flow field then reduce to the familiar gas dynamic Euler equations. The magnetic field can then be determined subsequently based upon the calculated flow field. It has been shown that the magnetic field determined in this manner--when using the exact MHD rather than approximate gas dynamic flow field--obeys the conservation principle that the magnetic flux passing through an arbitrary surface moving with the fluid is conserved or, in more picturesque

terms, that the magnetic field is convected with the fluid. It is generally regarded that the magnetic field calculated in this way i.e., when employing the approximate gas dynamic flow field, accurately predicts the general features as well as many details of the observations. This has been overwhelmingly confirmed with the current model by the many comparisons now made of convected field results with observations at Earth, Venus, and Mars (see Refs. 4-8). The interaction solution determined in this fashion is now commonly referred to as the gas dynamic-convected field approximation.

The decoupling of the B field calculation from the flow field determination is a particularly convenient and valuable feature in the basic interaction model. The flow field determination is the most time consuming portion (~90% CPU time) of the total computational process for a single case. However, once the flow field is determined and stored, many different magnetosheath fields due, for example, to different IMF's can be quickly and inexpensively determined as a separate process. Because the B calculation is extremely rapid, this feature, now imbedded in the model, has been exploited in a number of recent investigations, for example Refs. 4-8.

In order to determine the flow field, two separate gas dynamic solvers, as shown in Figure 2 below, have been incorporated in the model and linked together.



Nose Region Solver

- Beam and Warming implicit algorithm
- Transient and asymptotic steady state solution capabilities
- Fitted bow shock and obstacle discontinuity surfaces
- Fully implicit boundary conditions

Tail Region Solver

- Shiff and Steger implicit algorithm
- One step steady state solver
- Fitted bow shock and obstacle discontinuity surfaces
- Fully implicit boundary conditions

Figure 2. Illustration of NOSE/TAIL Subdivision of Flow Field and Associated Solvers Incorporated into Present Core Interaction Model

These flow solvers are:

NOSE Region Solver - to determine the flow field in the subsolar region and sufficiently far downstream to encompass the entire subsonic flow portion of the flow field

TAIL Region Solver - to determine the flow field downstream of the nose region to any arbitrary downstream distance

The core model has the capability for use in both a rapid warning mode to warn of impending changes in the magnetosheath plasma and field due to observed solar disturbances propagating in the interplanetary media, and also for use in a more detailed scientific analysis mode for fundamental research studies. In the current development of the core model, we have now extended and greatly enhanced the original model that was previously developed (Refs. 1-3). The model was completely rewritten to incorporate refined computational flow and magnetic field solvers. It has now been developed into a completely user-oriented structure, and has been extensively tested to insure robustness, generality, and ease of operation. An extensive graphics capability has been added so as to allow the complete and detailed examination of all plasma and field quantities in the interaction region. Importantly, the core model also contains the capability for providing time histories of the model-predicted plasma and field properties along any arbitrary spacecraft trajectory passing through the magnetosheath flow field. We and others have found this particular feature to be invaluable for comparative studies with observational data.

Included in the output capability of the core interaction model are the following:

- Contours of:
 - * Plasma temperature
 - * Plasma pressure
 - * Plasma density
 - * Plasma velocity magnitude
 - * Plasma sonic Mach number
 - * Magnetic field components
- Plasma flow streamlines
- Plasma flow characteristic lines
- Vector plots of:
 - * Plasma velocity
 - * Magnetic field
- Spacecraft trajectory plots:
 - * Ecliptic plane view
 - * Cylindrical plane view
- Time histories along spacecraft trajectory
 - * Plasma pressure, temperature, density
 - * Velocity magnitude and components
 - * Magnetic field magnitude and components

- Diagnostic analysis plots along any segment of the computational grid:

- * Plasma pressure, temperature, density
- * Velocity magnitude and components
- * Magnetic field magnitude and components

A brief subset of the detailed graphics output is provided in Figures 3 and 4.

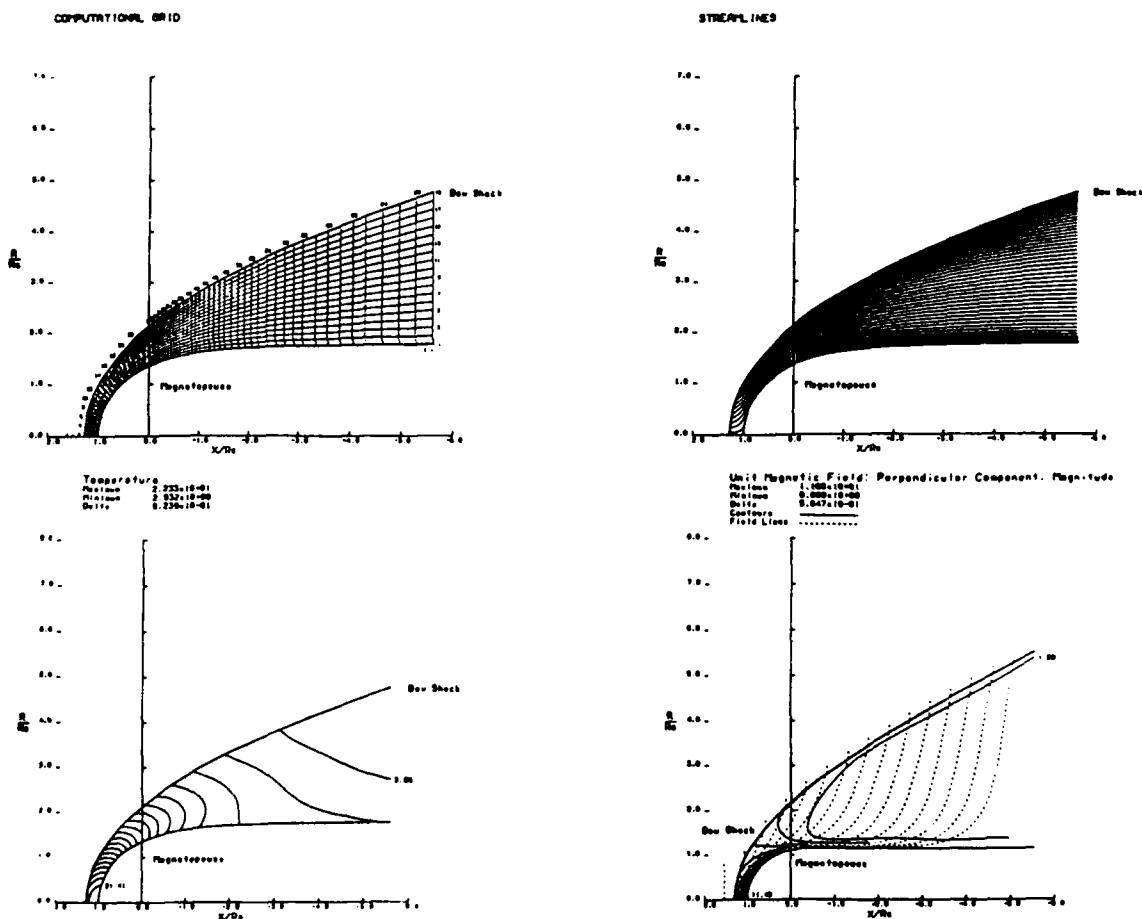


Figure 3. Sample of Selected Graphic Plasma and Field Results Provided by the Core Interaction Model

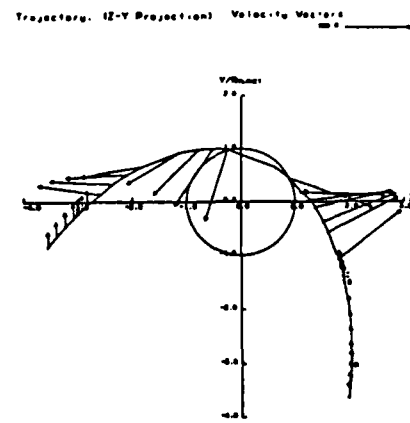
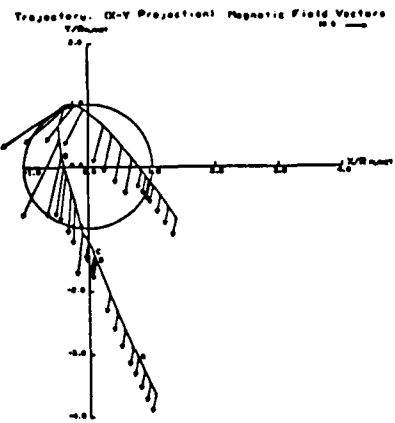
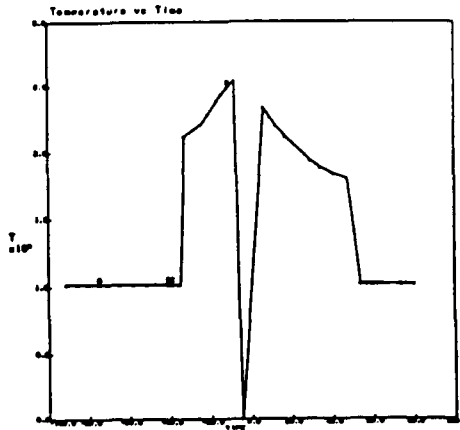
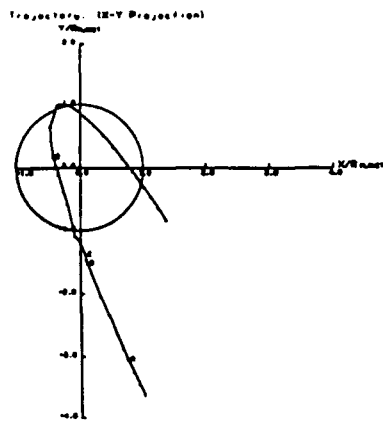


Figure 4. Example of Plasma and Field Results Standardly Provided by the Core Model as Time Histories and Vector Plots Along a Spacecraft Trajectory

Figures 5 and 6 provide examples of the actual use of such results from the core model that were directly employed in two recent space physics applications (Refs. 4, 5). Figure 5 displays a comparison of model-predicted magnetic field vectors with observations along a spacecraft trajectory, while Figure 6 displays a prediction of locations of magnetic merging sites on the Earth's magnetopause as a function of IMF orientation. As a final note, the source code for the graphics drivers was intentionally written by us rather than developed from proprietary routines. This was done to enable the entire package of numerical plus graphics routines embodied in the core model to be directly transportable without restriction to interested Air Force space scientists and others.

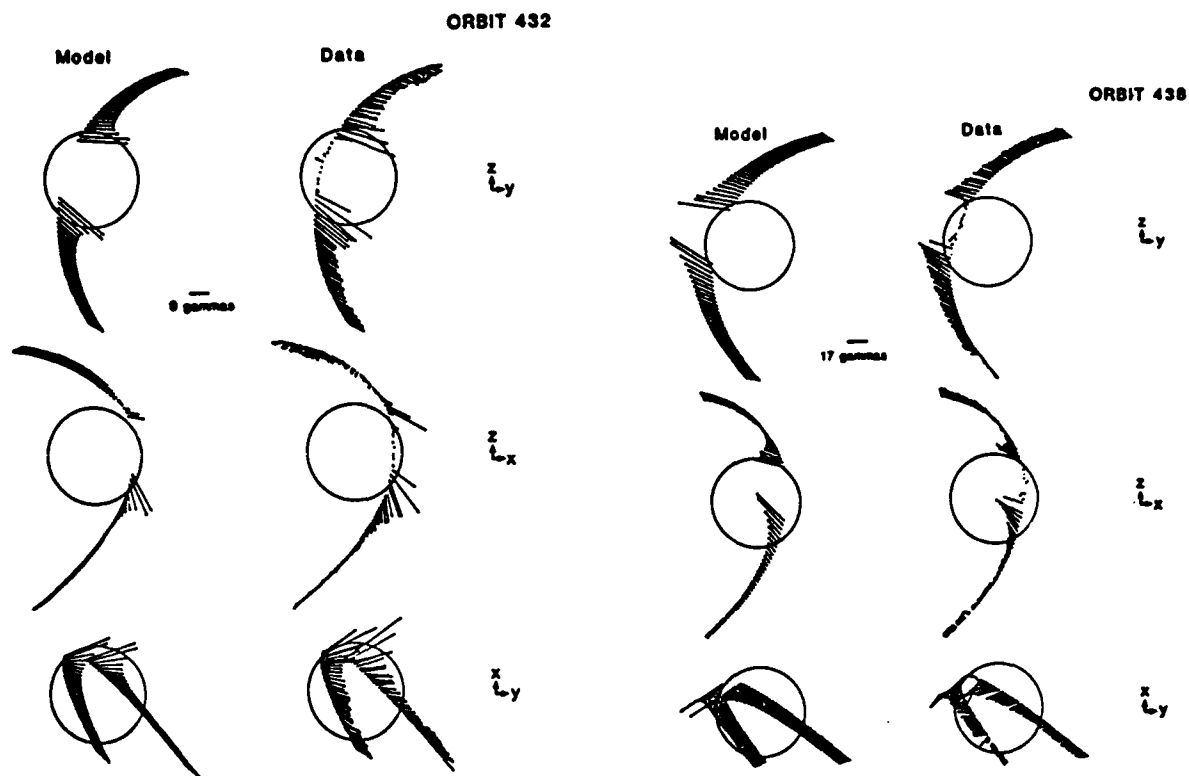
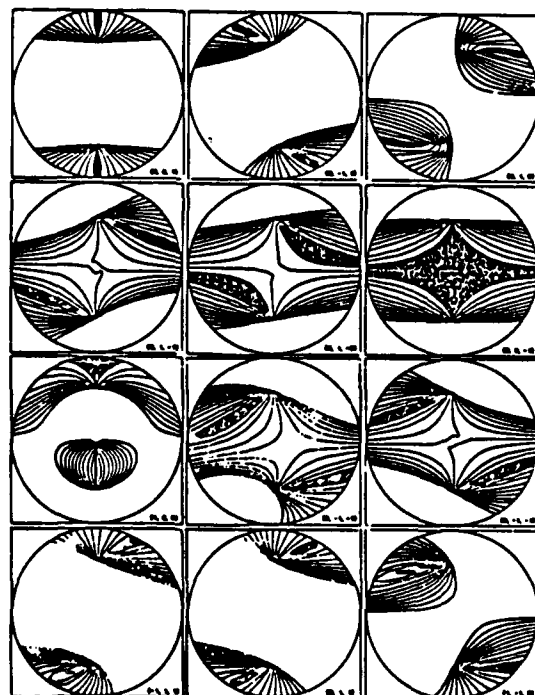


Figure 5. Example of Core Model Results for Magnetic Field Directly Compared With Actual Spacecraft Observations (Ref. 4)



Contours of equal values of the cosine of the angle between the magnetospheric and the magnetosheath magnetic fields for various values (B_x, B_y, B_z) of the IMF

Figure 6. Example of Core Model Results for Magnetic Merging Site Locations on the Earth's Magnetopause as Viewed From the Sun for Various IMF Orientations (Ref. 5)

In addition, a new computational module has now been developed to extend the capability of the core model to predict the time-dependent magnetic field anywhere in the global interaction region due to an unsteady IMF propagating past the magnetopause. This procedure is capable of handling both a continuously varying or discontinuous IMF. The computational submodel employs the basic core model for the flow field and applies a general convected-field calculation procedure for determining the unsteady B field anywhere in the magnetosheath. Figure 7 provides an example of this capability and displays the predicted unsteady magnetic field at several points in the magnetosheath due to the sinusoidally time-varying IMF indicated. In addition to this direct prediction capability, whereby based upon a given unsteady IMF the resultant unsteady B field can be predicted anywhere in the magnetosheath, we have also developed a computational module for the inverse problem. In this mode, if the unsteady B field is measured by a spacecraft at any point in the magnetosheath, the inverse procedure can determine the IMF time history. This provides a convenient means to estimate the unsteadiness in the IMF based upon single spacecraft measurements, and a direct comparative capability of prediction and observation for a two spacecraft system where one spacecraft serves as an upstream monitor. As in all of the convected-field computations in the core model, this procedure is extremely rapid requiring less than a minute on any superminicomputer system for an entire trajectory computation. The complete core interaction model, including the unsteady magnetic field prediction module and the display graphics, comprises approximately 20,000 lines of fortran source code.

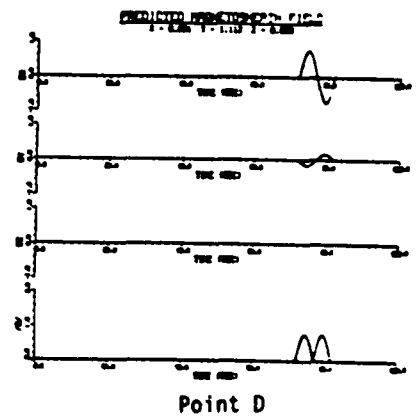
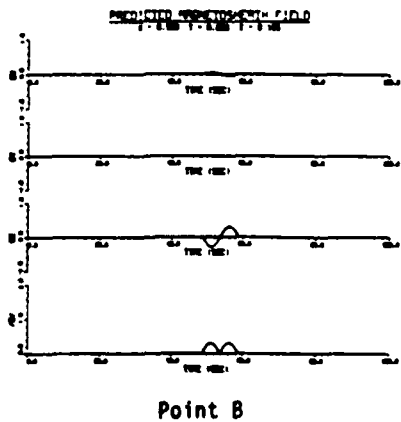
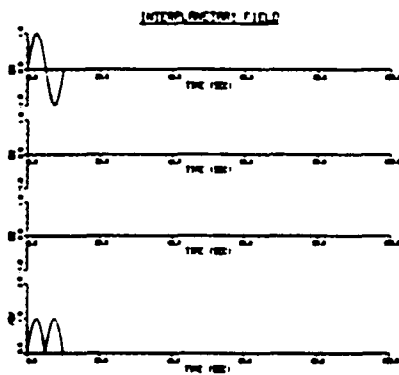
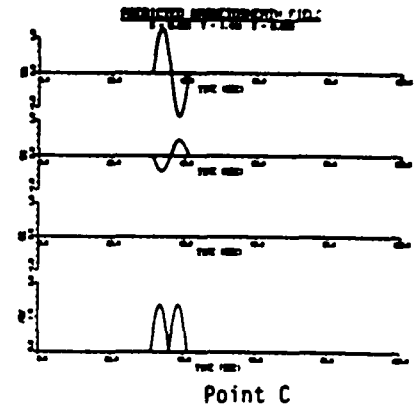
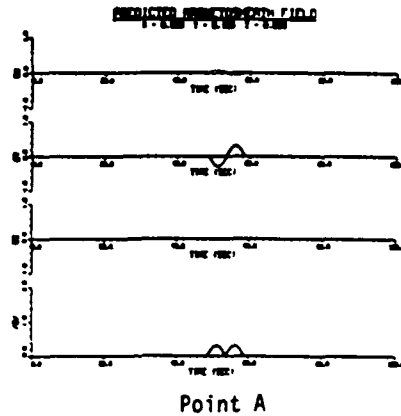
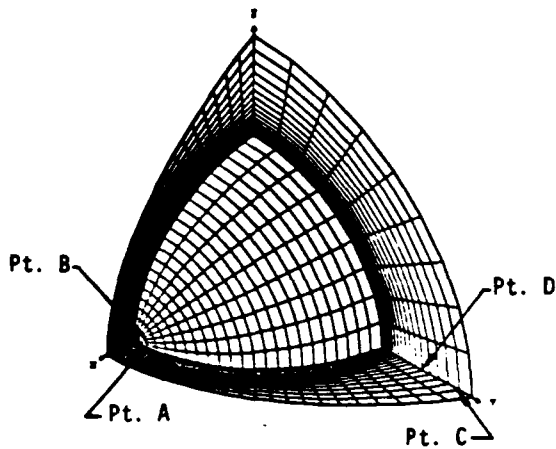


Figure 7. Illustration of the Capability of the Extended Core Interaction Model to Predict Unsteady Magnetic Fields in the Magnetosheath as a Function of a Time-Varying IMF

4.2 Development of Full 3-D Interaction Model

One of the major developments of the modeling effort planned for this program was the extension of the numerical solvers embodied in the core model, which apply to an axisymmetric magnetopause obstacle geometry, to a full arbitrary 3-D magnetopause geometry capability. For reasons of computational efficiency as pointed out in the previous section discussing the core interaction model, all of the various interaction models developed in this investigation have been developed to contain two separate and distinct flow field solvers. This particular computational feature is unique to the current model in comparison to all existing MHD models, and provides a number of important capabilities in our model that are unattainable with any of the other existing MHD models. The first flow field solver is an asymptotic time-marching solver and is employed to determine the flow field in the subsolar-to-terminator region (NOSE solver), while the other solver spatially marches that solution downstream from the terminator plane as far as required (TAIL solver).

We have now completed the development of both of the flow solvers for the 3-D model. In order to test and verify these solvers, we have performed extensive numerical tests of the 3-D model on several classes of 3-D magnetospheric shapes. Figure 8 provides results of one such application that was related to a study of the effect of asymmetry in the Earth's magnetopause on the bow shock location and shape. The insert in the bottom of that figure provides a prospective view of one quadrant of the typical computational grid employed in the 3-D model. Illustrated in that insert are the complete computational grids in the equatorial (X,Y) and polar (X,Z) azimuthal planes, together with the intersection of the grids in the other azimuthal planes with the magnetopause surface. Shown next to the computational grid is a sketch illustrating the distortion from circular symmetry in the cross sectional shape of the Earth's magnetopause that was systematically varied in this study. The three plots in the upper part of Figure 8 provide the calculated 3-D model results for the bow shock locations and the corresponding magnetopause locations in the 10 equally-spaced azimuthal planes shown in the computational grid. The results in those plots are for Mach = 8.0 flow past a terrestrial magnetopause shape whose cross-section has been distorted from a circular shape into an elliptic shape in which the ellipse has its major axis in the polar meridian and its minor axis in the equatorial plane. The plot on the upper left of Figure 8 is for a cross sectional shape with a major/minor axis ratio $A/B = 1.05$. Corresponding results for modeled magnetopauses that have elliptic cross sections with major/minor axis ratios of $A/B = 1.10$ and 1.15 are illustrated in the middle and right-hand plots, respectively for these various elliptic shapes. The two plots on the bottom left and right of Figure 8 display a summary of the bow shock and magnetopause locations in the equatorial and polar meridian planes, respectively. These results taken in total show that the typical bow shock surface displacement from axisymmetry that occurs due to asymmetry effects in the magnetopause surface is somewhat less than approximately 50% of the corresponding displacement from axisymmetry of the magnetopause, an important result to know when trying to evaluate or

ascertain 3-D geometry distortions in the Earth's bow shock and magnetopause shapes.

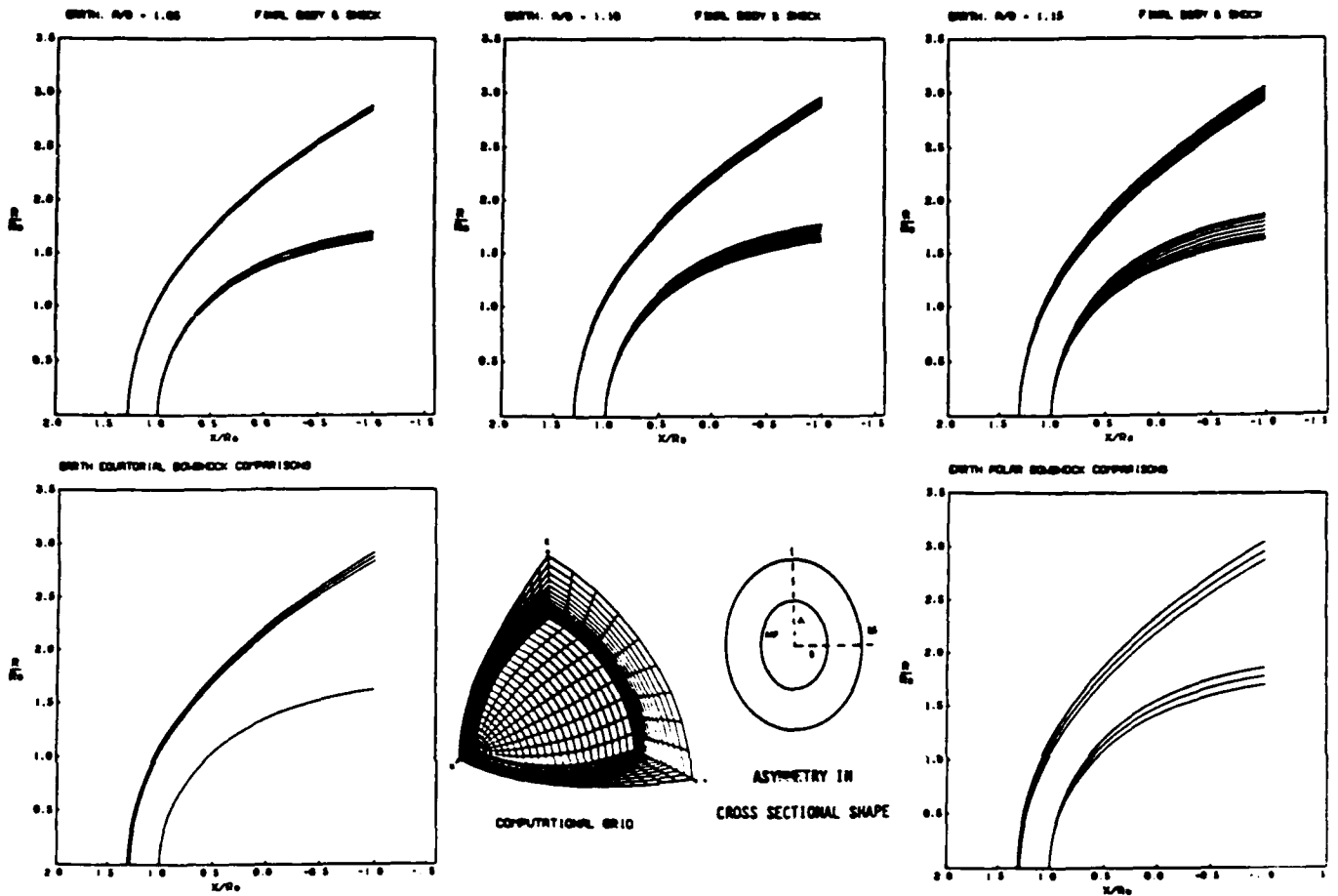


Figure 8. Results from the 3-D Terrestrial Interaction Model Illustrating the Effect of Asymmetry in the Earth's Magnetopause Cross Sectional Shape on the Terrestrial Bow Shock Shape and Location

Since the 3-D geometric distortion of the Earth's magnetopause is not as severe as those of some other planets in the solar system, we have used joint NASA support to provide the means to carry out a more severe test and verification of the 3-D model. Employing observational data obtained for Jupiter and Saturn, we have used the 3-D model to determine the flow fields and corresponding bow shock surfaces that exist about these highly three-dimensional obstacles. The computational model performed exceptionally well in these tests, and we observed no convergence difficulties for all of the extensive numerical testing performed. Furthermore, based on the parametric studies that were carried out involving the systematic variation of the 3-D magnetopause geometry, the 3-D predictive model was able to quantitatively determine the amount of 3-D distortion that must exist in these magnetopauses and, as a consequence, resolve the anomaly previously noted (Ref. 9) with regard to the observed equatorial bow shock locations for these planets.

The results of this study were reported in Ref. 10, and were also presented at the Spring 1987 AGU and Summer AIAA meetings. A complete description of the details of the numerical algorithms employed in the 3-D model is provided in Ref. 10. Finally, a revised version of Ref. 10 is presently in review for publication in the JGR.

4.3 Development of Aligned Flow Full MHD Interaction Model

The final steady state computational interaction submodel that has been developed extends the level of simulation accuracy beyond the gas dynamic-convected field approximation employed in the other interaction submodels to that of full MHD. This submodel is capable of predicting the global solar wind-planetary interaction at the full MHD accuracy level for situations when the IMF is aligned with the oncoming flow direction. The submodel is appropriate for determining supersonic, super-Alfvénic solar wind flows past general axisymmetric magnetosphere obstacle shapes. As with all the other submodels developed, this computational model also employs two separate but coupled flow field solvers to determine the steady flow field: an asymptotic time-marching procedure for the subsolar to terminator region, and a spatially-marching procedure for post-terminator locations. Both of these new computational procedures are based on current, fully-implicit numerical algorithms, and both employ fitted discontinuity representations for the bow shock and magnetospheric obstacle surfaces. Initial applications of the model have now been successfully made to Earth and Venus. Some results of application of the new aligned flow MHD model to Earth are provided in Figure 9. In that figure, results from the new model are compared to a selected number of comparable results previously determined by Spreiter and Rizzi (Ref. 11) using a completely different computational method. The new model predicts the identical variation of the bow shock shape as a function of Alfvén Mach number in the oncoming solar wind that was previously obtained, that is, as the oncoming Alfvén Mach number decreases, the bow shock simultaneously moves inward toward the magnetopause in the nose region and flares outward away from the magnetopause along its flanks. Moreover, it attains in a much more effective and general way than before the capability for routinely calculating exact MHD solutions for aligned flows past a planetary magnetosphere. Such results from the new model demonstrate a new capability for quantitatively determining the sensitivity of the terrestrial bow shock to MHD effects. In particular, the new model provides a direct means for evaluating the dependence of the bow shock location and shape on the Alfvén Mach number of the oncoming interplanetary solar wind. More recent studies with the new model have unequivocally demonstrated the parametric importance of the magnetosonic Mach number for characterizing MHD effects in planetary bow shocks.

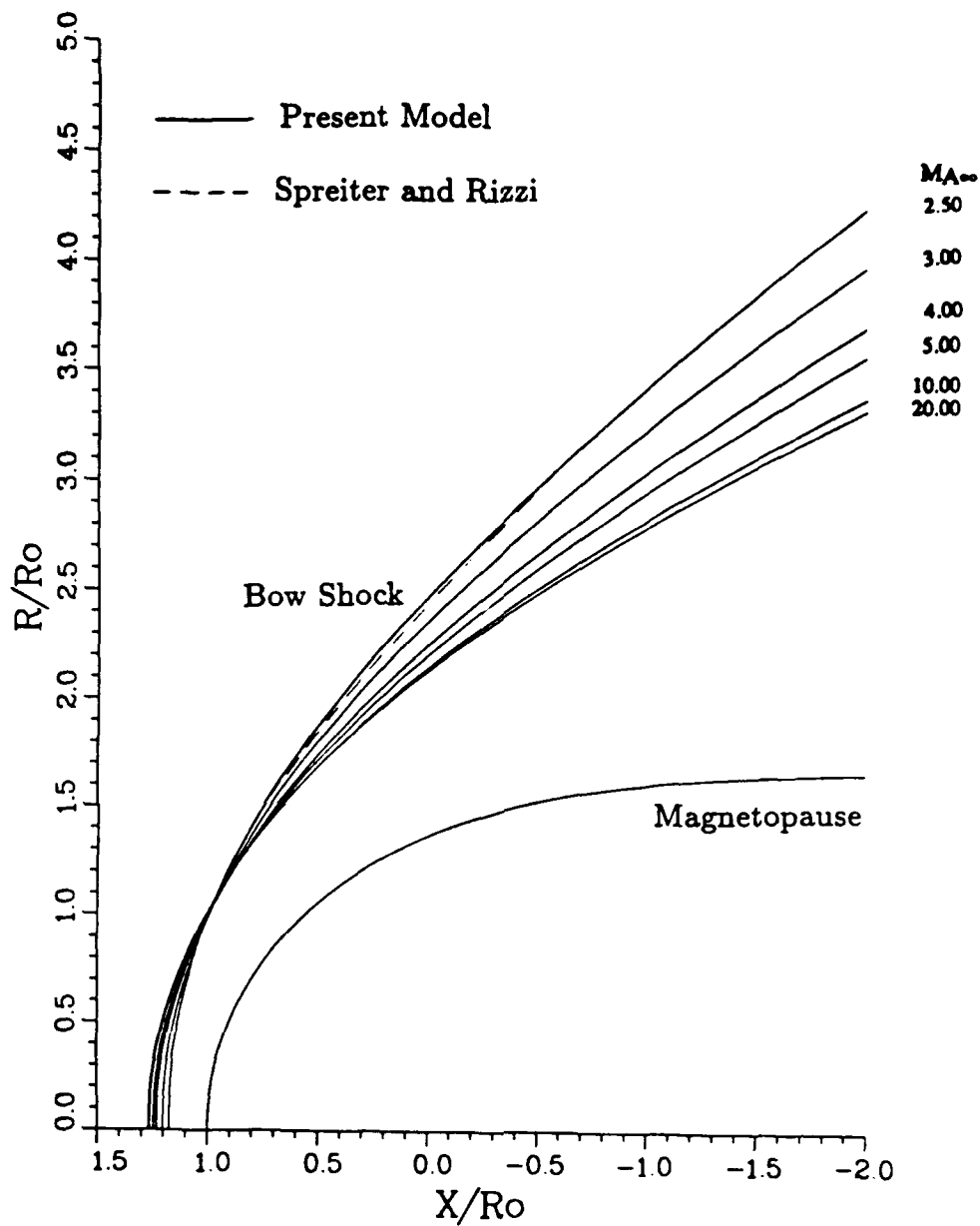


Figure 9. Bow Shock Locations Predicted by the New Aligned Flow Submodel Compared With Spreiter and Rizzi (Ref. 11) for Aligned Flow Past the Earth's Magnetopause with Sonic Mach Number $M_\infty = 10$, $\gamma = 5/3$, and Various Alfvén Mach Numbers $M_{A\infty}$

4.4 Development of Continuous Flow Transient Interaction Model

The continuous flow transient interaction model provides the capability for accounting for transients that may occur in the oncoming interplanetary plasma flow that propagate into an established bow shock and magnetosheath flow field. The model employs two, new, fully-implicit computational solvers coupled in the familiar NOSE/TAIL combination employed in the core model. Additionally, a new computational module has been added to determine the convected B field in a highly refined manner employing a dense streamline coverage and a grid clustering capability. This important feature will be integrated into the core interaction model in the near future. Figure 10 illustrates the extended upstream grid employed in the new model to account for the propagation of these transients into the bow shock and magnetosheath, and the high resolution and detail in the predicted flow magnetic field in the magnetosheath region that is achievable from this model.

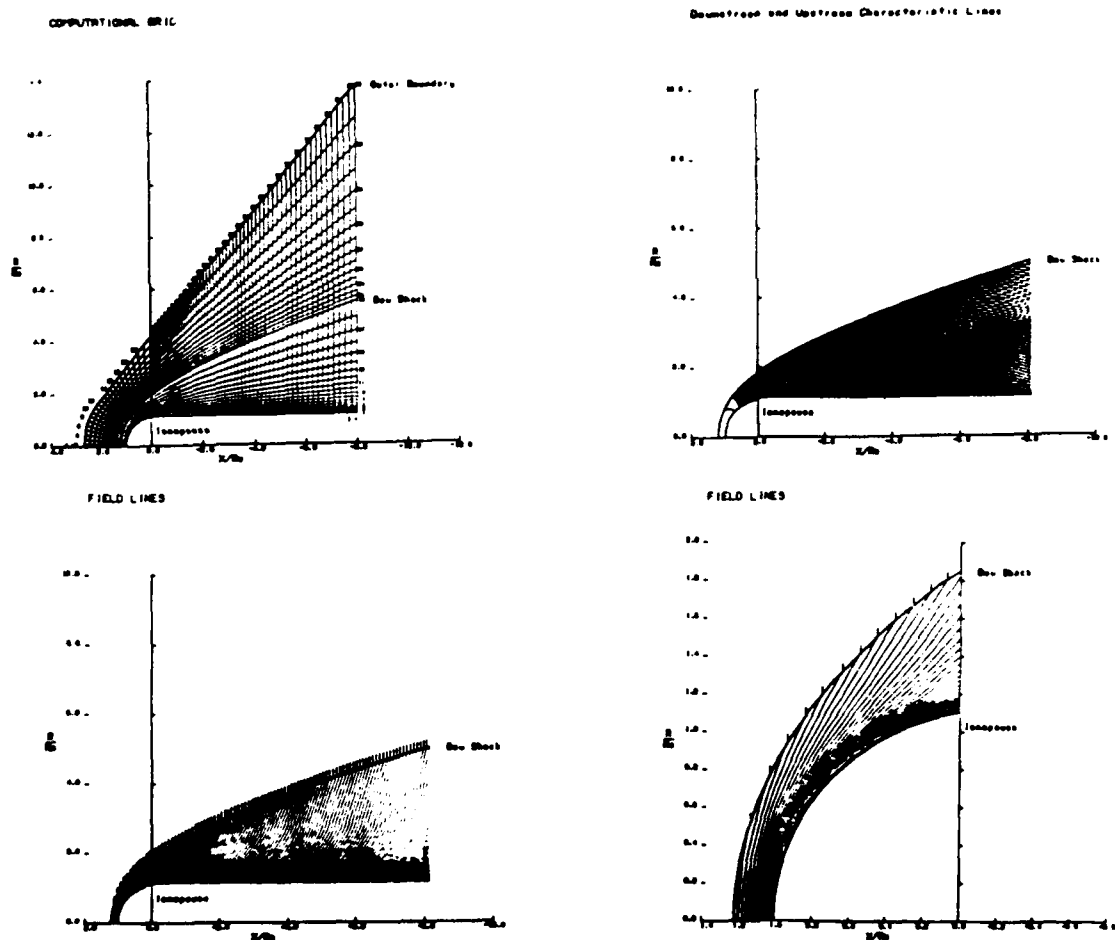


Figure 10. Illustration of the Extended Upstream Grid and High-Resolution Plasma and Field Predictive Capability of the Continuous Flow Transient Interaction Submodel

The significance of the continuous flow transient interaction model to this development effort is threefold: first, the model provides an important upgrade of the computational flow models employed in the basic core interaction model; second, it provides the capability for an extremely refined computation of the plasma and convected magnetic field properties in the vicinity of the magnetopause obstacle, particularly in the subsolar region; and third, it provides an accurate numerical model for quantitatively testing simpler rational unsteady interaction models for predicting time-dependent dynamic plasma properties due to unsteady behavior in the oncoming solar wind plasma. One of the most important results of this modeling effort has been the unambiguous demonstration that simulations of unsteady dynamic processes involving the interaction of the solar wind with the Earth's magnetopause involve so much computational resources with regard to computational time and memory that for such dynamic interaction models to be useful they must be computationally simplified. As discussed previously with regard to the core interaction model, development of a time-dependent dynamic model to predict the behavior of the convected magnetic field based upon the underlying plasma flow properties remaining steady is relatively straightforward, and has now been accomplished within the core interaction model. However, the corresponding development of a time-dependent dynamic model for predicting the plasma properties in the interaction region is more involved. Nevertheless, the continuous flow transient interaction model, and the discontinuous flow transient interaction model discussed in the following section, provide the means to develop and quantitatively verify such dynamic models. We view the development of more efficient time-dependent plasma and magnetic field models as the next most important step in modeling the solar wind-terrestrial interaction process.

4.5 Development of Discontinuous Flow Transient Interaction Model

The discontinuous flow transient interaction model is capable of predicting the unsteady global interaction that occurs when discontinuous transients, such as interplanetary shocks, impinge on the terrestrial environment and subsequently interact with an established bow shock and magnetopause configuration. This interaction submodel also employs an extended upstream grid, but instead of using a fitted discontinuity representation for the bow wave, as is used in both the core and continuous flow transient interaction models, this model uses a shock capturing procedure to capture all shocks in the flow field. This is necessary as shock-on-shock interactions are too cumbersome to treat with a fitted discontinuity representation. While the theoretical basis underlying this model is the same as that employed in the core model, the new procedure employs a completely different computational flow field solver from that used in both the core model and the continuous flow transient interaction model. This state-of-the-art computational solver employs an implicit, upwind, flux-differenced total variation diminishing (TVD) algorithm, and is extremely efficient and capable of providing highly-detailed, time-accurate descriptions of the plasma and field properties in the interaction region of the solar wind with the Earth's magnetosphere at modest supercomputer computational cost (approximately 15 CRAY XMP CPU min/case). The new model allows the complete time-accurate determination of the discontinuous changes in the bow shock and magnetosheath flow field that result from the impingement of an interplanetary shock wave generated by solar flares or other occurrences on a previously established steady state terrestrial bow shock/magnetopause flow configuration.

As an indication of the capability of the new discontinuous flow model, we provide results in Figure 11 of an application of the model. Shown in that figure are a sequence of plots displaying the predicted plasma pressure contours in the magnetosheath region that result from the impingement of an interplanetary shock followed by Mach = 12.0 flow on a previously established steady Mach = 8.0 flow pattern about the Earth's magnetopause. Beginning with the plot in the upper left hand corner of the figure, the internal shock patterns that are created and reflected between the bow shock and the magnetopause in the magnetosheath region as the interplanetary shock impacts on and then moves downstream along the flanks of Earth's magnetopause can be readily discerned. Notable in the results is the relatively rapid establishment of the new steady state flow pattern as the interplanetary shock moves past the magnetopause.

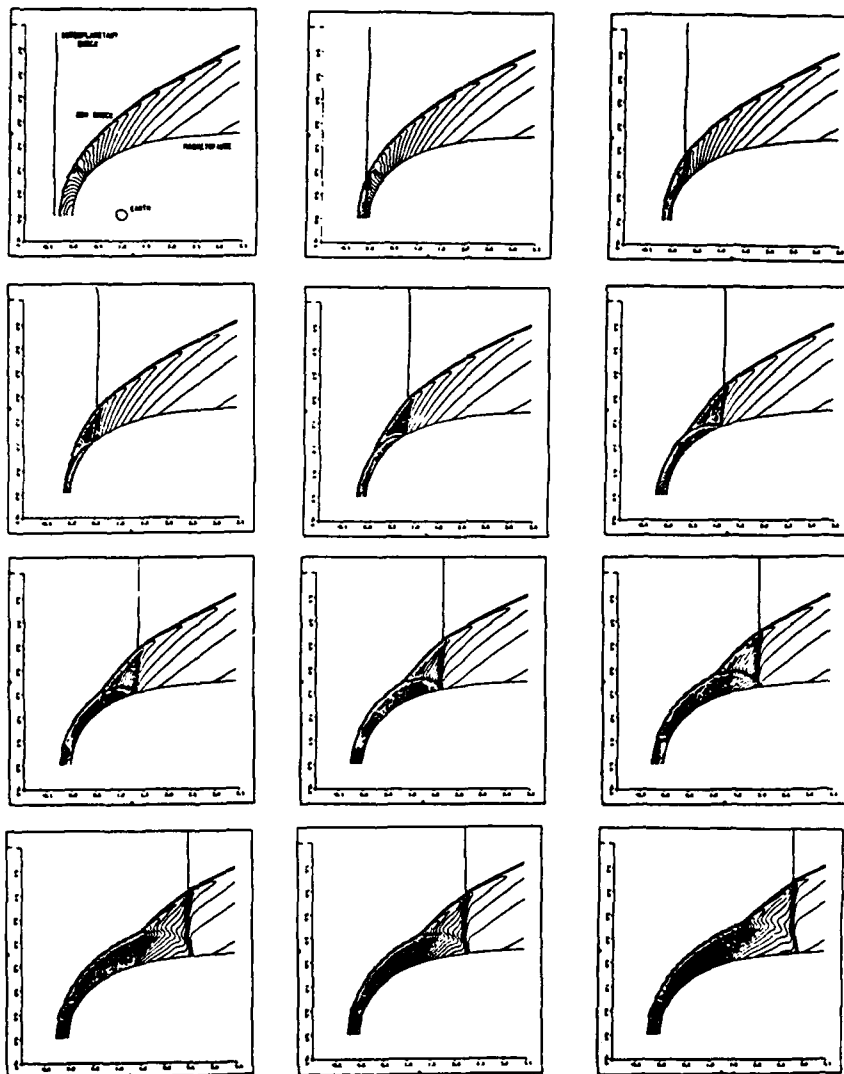


Figure 11. Illustration of Results from the Discontinuous Flow Transient Interaction Submodel: Plasma Pressure Contours Resulting from the Global Interaction of an Interplanetary Shock with an Established Terrestrial Bow Shock/Magnetopause Configuration

In order to expedite development of the discontinuous flow transient interaction model, in these initial calculations with the model we have held the location of the magnetopause fixed. This simplification, which can be relaxed simply by introducing time-dependent grid metrics, was adopted since the addition of time-dependent grid metrics in the computational model would have substantially complicated and extended the development effort and time for this model. Since this unsteady interaction model will always require substantially more computational resources than the other axisymmetric interaction models developed and consequently will not be employed for routine interaction calculations, we have chosen to defer the introduction of time-dependent metrics into the model to a later time. The major importance of the discontinuous flow transient interaction model to this effort are the computational flow results that it is able to provide. These flow results provide the basis for construction of a rational, computationally-simple, unsteady flow interaction model that can capture the essence of the discontinuous interaction process involving impingement of an interplanetary shock on an established terrestrial bow shock and magnetopause configuration but at a computational efficiency at least two orders of magnitude higher. Based on results from the current discontinuous flow transient interaction model, we now have the means for estimating the extent of and approximating the flow details within the transient flow region that separates the initial and final steady state bow shock and magnetopause configurations. Those initial and final steady state configurations and associated flow conditions can be directly determined by the core interaction model. Using this rational modeling concept, the entire complex unsteady shock-on-shock interaction process can be simulated by a relatively simple but accurate and computationally-efficient interaction model.

In summary, the significant accomplishments that have been achieved in this modeling effort include:

- Development of a core interaction model in user-oriented format for both quick response use and also for detailed scientific analysis

- Development, verification, and application of a series of extended interaction models including:
 - * Fully unsteady B field predictive capability in core model
 - * New 3-D flow interaction model for predicting steady plasma properties about arbitrary 3-D magnetopause geometries
 - * New aligned flow MHD interaction model for predicting steady full MHD solutions about arbitrary axisymmetric magnetopause geometries
 - * New flow interaction model for predicting continuous plasma transient phenomena
 - * New flow interaction model for predicting discontinuous plasma transient phenomena

The preliminary development of the terrestrial interaction model is now successfully complete. The interaction models developed, considered in total, allow the quantitative prediction of details of the plasma and field properties associated with a variety of interaction phenomena, both steady and unsteady, to a degree of accuracy and routineness that was previously unachievable.

The most important remaining work lies in the further development and enhancement of the modeling capability for accurately simulating strongly dynamic processes associated with the global solar wind-terrestrial environment system, in particular with regard to plasma properties. This work should involve development of both advanced computational models capable of accurate dynamic simulations as well as computationally-simplified, rational dynamic models which are based upon the advanced computational models but which allow the accurate approximate simulation of unsteady solar wind-terrestrial interaction phenomena at a greatly reduced computational cost.

5. PRESENTATIONS AND PUBLICATIONS

PRESENTATIONS

1. Stahara, S. S., R. R. Rachiele, and J. R. Spreiter. Development of a 3-D Gasdynamic Model for Solar Wind Interaction with Nonaxisymmetric Magnetospheres. Presented at Spring 1987 AGU Meeting, Baltimore, MD, May 18-21, 1987.
2. Stahara, S. S., G. M. Molvik and J. R. Spreiter. A Mass Loaded Gasdynamic Model for Solar Wind/Cometary and Planetary Interactions. Presented at Spring 1987 AGU Meeting, Baltimore, MD, May 18-21, 1987.
3. Stahara, S. S., R. R. Rachiele, J. R. Spreiter, and J. A. Slavin. A 3-D Computational Model for Solar Wind/Magnetosphere Interactions: Prediction of Polar Flattening of Jupiter and Saturn Magnetospheres. Presented at AIAA 19th Fluid Dynamics, Plasma Dynamics and Lasers Conference, Honolulu, HI, June 8-10, 1987.
4. Stahara, S. S., G. M. Molvik and J. R. Spreiter. A New Computational Model for the Prediction of Mass Loading Phenomena for Solar Wind Interactions With Cometary and Planetary Ionospheres. Presented at AIAA 19th Fluid Dynamics, Plasma Dynamics and Lasers Conference, Honolulu, HI, June 8-10, 1987.
5. Stahara, S. S. and J. R. Spreiter. Recent Developments in Computer Modeling of Solar Wind Interaction with the Magnetosphere. Presented at the AFGL, Hanscom AFB, MA, November 17, 1987.
6. Stahara, S. S. and J. R. Spreiter. Recent Developments in Computer Modeling of Solar Wind Interactions with Planetary Magneto/ionospheres. Presented at Goddard Space Flight Center, November 18, 1987.
7. Stahara, S. S. Recent Developments in Computational Modeling of Solar Wind Interactions with Planetary Magnetoionospheres. Presented at Institute of Geophysics and Planetary Physic, UCLA, Febuary 10, 1988.
8. Stahara, S. S., G. M. Molvik and J. R. Spreiter. A New Computational Model for Predicting Aligned MHD Solar Wind Flow Past Planetary Magnetoionospheres: Application to Earth and Venus. Presented at the Fall 1988 AGU Meeting, San Francisco, CA, December 4-8, 1988.

PUBLICATIONS

1. Stahara, S.S., R.R. Rachiele, J.R. Spreiter, and J.A. Slavin: A 3-D Computational Model for Solar Wind/Magnetosphere Interactions: Prediction of Polar Flattening of Jupiter and Saturn Magnetospheres: AIAA Paper No. 87-1411, June 1987.

2. Stahara, S.S., G.A. Molvik, and J.R. Spreiter: A New Computational Model for the Prediction of Mass Loading Phenomena for Solar Wind Interactions With Cometary and Planetary Ionospheres. AIAA Paper No. 87-1410, June 1987.
3. Stahara, S. S., R. R. Rachiele, J. R. Spreiter, and J. A. Slavin. A Three Dimensional Gasdynamic Model for Solar Wind Flow Past Nonaxisymmetric Magnetospheres: Application to Jupiter and Saturn. In Press, Jour. Geophys. Res.

REFERENCES

1. Stahara, S. S., D. Klenke, B. C. Trudinger, and J. R. Spreiter: Application of Advanced Computational Procedures for Modeling Solar-Wind Interactions with Venus - Theory and Computer Code. NASA CR 3267, May 1980.
2. Spreiter, J. R., and S. S. Stahara: A New Predictive Model for Determining Solar Wind - Terrestrial Planet Interactions. J. Geophys. Res., Vol. 85, No. A12, December 1, 1980, pp. 6769-6777.
3. Spreiter, J. R., and S. S. Stahara: Solar-Wind Flow Past Venus - Theory and Comparisons. J. Geophys. Res., Vol. 85, No. A13, December 1980, pp. 7715-7738.
4. Luhmann, J. G., R. J. Walker, C. T. Russell, N. U. Crooker, J. R. Spreiter, S. S. Stahara, and D. J. Williams: Mapping the Magnetosheath Field Between the Magnetopause and the Bow Shock: Implications for Magnetospheric Particle Leakage. J. of Geophys. Res., Vol. 89, No. A8, August 1984, pp. 6829-6834.
5. Luhmann, J. G., R. J. Walker, C. T. Russell, N. U. Crooker, J. R. Spreiter, and S. S. Stahara: Patterns of Potential Magnetic Field Merging Sites on the Dayside Magnetopause. J. Geophys. Res., Vol. 89, No. A3, March 1984, pp. 1739-1742.
6. Russell, C. T., J. G. Luhmann, J. R. Spreiter, and S. S. Stahara: The Magnetic Field of Mars: Implications from Gas Dynamic Modeling. J. Geophys. Res., Vol. 89, No. A5, May 1984, pp. 2997-3003.
7. Crooker, N. U., J. G. Luhmann, J. R. Spreiter, and Stahara, S. S.: Magnetopause Merging Site Asymmetries. J. Geophys. Res., Vol. 90, No. A1, January 1985, pp. 341-346.
8. Crooker, N. U., J. G. Luhmann, C. T. Russell, E. J. Smith, J. R. Spreiter, and S. S. Stahara: Magnetic Field Draping Against the Dayside Magnetopause. J. Geophys. Res., Vol. 90, No. A4, April 1985, pp. 3505-3510.
9. Slavin, J. A., E. J. Smith, J. R. Spreiter, and S. S. Stahara: Solar Wind Flow About the Outer Planets: Gasdynamic Modeling of the Jupiter and Saturn Bow Shock, J. Geophys. Res., Vol. 90, No. A7, July 1985, pp. 6275-6286.
10. Stahara, S. S., R. R. Rachiele, J. R. Spreiter, and J. A. Slavin. A 3-D Computational Model for Solar Wind/Magnetosphere Interactions: Prediction of Polar Flattening of Jupiter and Saturn Magnetospheres. Presented at AIAA 19th Fluid Dynamics, Plasma Dynamics and Lasers Conference, Honolulu, HI, June 8-10, 1987.
11. Spreiter, J. R., and A. W. Rizzi, Aligned Magnetohydrodynamic Solution for Solar Wind Flow Past the Earth's Magnetosphere. Acta Astronautica, Vol 1, 1974, pp. 15-35.

APPENDIX-COPIES OF PUBLICATIONS

TABLE OF CONTENTS

	PAGE
Stahara, S. S., R. R. Rachiele, and J. R. Spreiter. Development of a 3-D Gasdynamic Model for Solar Wind Interaction with Nonaxisymmetric Magnetospheres. Presented at Spring 1987 AGU Meeting, Baltimore, MD, May 18-21, 1987.	31
Stahara, S. S., G. M. Molvik and J. R. Spreiter. A Mass Loaded Gasdynamic Model for Solar Wind/Cometary and Planetary Interactions. Presented at Spring 1987 AGU Meeting, Baltimore, MD, May 18-21, 1987.	32
Stahara, S.S., R.R. Rachiele, J.R. Spreiter, and J.A. Slavin: A 3-D Computational Model for Solar Wind/Magnetosphere Interactions: Prediction of Polar Flattening of Jupiter and Saturn Magnetospheres: AIAA Paper No. 87-1411, June 1987.	33
Stahara, S.S., G.A. Molvik, and J.R. Spreiter: A New Computational Model for the Prediction of Mass Loading Phenomena for Solar Wind Interactions With Cometary and Planetary Ionospheres. AIAA Paper No. 87-1410, June 1987.	43
Stahara, S. S., G. M. Molvik and J. R. Spreiter. A New Computational Model for Predicting Aligned MHD Solar Wind Flow Past Planetary Magnetoionospheres: Application to Earth and Venus. Presented at the Fall 1988 AGU Meeting, San Francisco, CA, December 4-8, 1988.	54
Stahara, S. S., R. R. Rachiele, J. R. Spreiter, and J. A. Slavin. A Three Dimensional Gasdynamic Model for Solar Wind Flow Past Nonaxisymmetric Magnetospheres: Application to Jupiter and Saturn. In Press, J. Geophys. Res.	55

Development of a 3-D Gasdynamic Model for Solar Wind Interaction with Nonaxisymmetric Magnetospheres

S S Stahara and R R Rachiele (RMA Aerospace, Inc., Mountain View, CA 94043; 415-961-0560)
J R Spreiter (Div. of Applied Mechanics, Stanford University, Stanford, CA 94305; 415-723-2891)

The gasdynamic convected magnetic field model for predicting solar wind flow past a planetary magnetoionopause obstacle has been extended to three-dimensions to apply to obstacles of nonaxisymmetric shape. Development of the 3-D computational model is described, as well as results of an application of the new model to the magnetospheres of Jupiter and Saturn. These magnetospheres provide a strong test of the new 3-D model since the combined effects of rapid spin, large size, and substantial ring current phenomena are believed to cause the magnetospheres of these planets to be significantly broader near the planetary equatorial plane than near the noon-midnight polar meridian plane. With the aid of the new three-dimensional model, it is now possible to infer the degree of flattening of the magnetospheric cross sections from a knowledge of the locations of the low-latitude magnetopause and bow shock crossings. In this paper, the computational procedures of the new model are described, and calculated results are presented for a number of magnetospheres of elliptic cross sections with values ranging from 1 to 2 for the ratio a/b of major (equatorial) to minor (polar) axes. This range is sufficient to include values appropriate to both Jupiter and Saturn. Comparisons of the model results with the locations of observed crossings of the magnetopause and bow shock directly provide an estimate of the degree of equatorial broadening of the magnetospheric cross section for each of these planets. For Jupiter, the results indicate a broadening to $a/b \sim 1.75$, a value consistent with previous estimates determined from independent calculations of the three-dimensional magnetosphere shape formed by adding to the planetary dipole field the magnetic field of an equatorial current sheet selected so as to match the observed Jovian magnetic field near the equatorial plane. For Saturn, a similar comparison indicates a smaller broadening to $a/b \sim 1.25$. The determination is less certain than for Jupiter, however, because of the smaller amount and greater scatter of the available data.

A Mass Loaded Gasdynamic Model for Solar Wind/Cometary and Planetary Interactions

S S Stahara and G M Molvik (RMA Aerospace, Inc., Mountain View, CA 94043; 415-961-0560)
J R Spreiter (Div. of Applied Mechanics, Stanford University, Stanford, CA 94305; 415-723-2891)

The development of a new computational model for predicting in detail the mass loading phenomena known to occur when the solar wind interacts with cometary and certain planetary ionospheres is described. The computational model employs two separate but coupled flow solvers to determine the steady flow field: an asymptotic time-marching procedure for the subsolar to terminator region, and spatially-marching procedure for the post-terminator region. The procedures are based on current, fully-implicit algorithms and employ fitted discontinuity representations for both the bow shock and ionospheric obstacle surfaces. A detailed description of the computational model is provided, in particular, the high degree of accuracy the model is able to provide in regions near the obstacle surface is described as well as the high resolution of the convected magnetic field prediction near the magnetopause surface. Mass loading due to photoionization has been incorporated into the model, and results of initial applications of the model to cometary interactions and to the mass loaded Venus ionosheath are described. For the Venus application, the model has been used in an inverse sense to determine the mass loadings required to displace the Venusian bow shock at the terminator to the locations observed at solar EUV maximum and minimum.

A 3-D COMPUTATIONAL MODEL FOR
SOLAR WIND/MAGNETOSPHERE INTERACTIONS:
PREDICTION OF POLAR FLATTENING OF
JUPITER AND SATURN MAGNETOSPHERES

S. S. Stahara* and R. R. Rachiele**
RMA Aerospace, Inc., Mountain View, California

J. R. Spreiter†
Division of Applied Mechanics, Stanford University
Stanford, California

J. A. Slavin††
NASA Headquarters, Washington, D.C.

Abstract

The gasdynamic convected magnetic field model for predicting solar wind flow past a planetary magnetopause obstacle has been extended to apply to obstacles of nonaxisymmetric shape. The need for such an extension is small for applications to the Earth and other terrestrial planets; but is significant for Jupiter and Saturn where the combined effects of rapid spin, large size and substantial ring current phenomena are thought to cause the magnetosphere to be significantly broader near the planetary equatorial plane than in the noon-midnight polar meridian plane. Confirmation by direct observation cannot yet be made, however, because observational data are available only for conditions near the equatorial planes. Development of the computational procedures of the new three-dimensional model is described and results of an application to examine the suspected polar flattening of the Jupiter and Saturn magnetospheres are provided. A quantitative determination of the degree of polar flattening is obtained for each of these planets by employing the new model together with observations of the low latitude magnetopause and bow shock wave locations. For Jupiter, the results both confirm and better define previous qualitative estimates of the flattening determined from independent calculations of three-dimensional magnetosphere shapes formed by adding to the planetary dipole field the magnetic field of an equatorial current sheet selected so as to match the observed Jovian magnetic field near the equatorial plane. For Saturn, the predicted location of the equatorial bow shock agrees well with the observations near the nose of the bow shock, but the observed shock wave appears to flare out substantially more than the predicted shock wave at the terminator location. The number of these observations is small, however, and it is not possible at this time to determine whether this difference is due to some significant process peculiar to Saturn not included in the analysis, or a meaningless artifact resulting from temporal changes in conditions occurring at the time the observations were made.

Introduction

The gasdynamic convected magnetic field approximation to the magnetohydrodynamic model for supersonic solar wind flow past a planetary magnetosphere has provided a useful basis for understanding the solar wind planetary interaction process from its inception more than two decades ago¹ to the present day (see References 2-4 for recent reviews of the theory and applications). The original model calculations, although accurate, were tedious to perform with the methods available at the time. As a result, solutions were carried out for only a limited number of cases.

More recently, Spreiter and Stahara^{5,6} completely revised the solution procedures without changing the underlying physics in order to take advantage of the enormous advances in computer capability and computational methods that have occurred since the original model was conceived. The result is a well-documented model capable of routinely providing solutions for the detailed flow and magnetic field properties throughout the magnetosheath region between the bow wave and a rather arbitrarily specified shape for the planetary magnetopause or ionopause. The results provided by the model have now been widely used in the interpretation of spacecraft data, and for further extensions of the theory.

Throughout this theoretical development of the model, the shape of the magnetospheric obstacle has always been approximated as axisymmetric about a line parallel to the incident solar wind direction and passing through the planetary center. For application to the earth, this has been justified by numerous studies of extensive observational data in which it has been shown that any departure from axisymmetry is virtually immeasurable. More precisely, Fairfield⁷ and Holzer and Slavin⁸ have determined the eccentricity c of the magnetospheric cross section in the terminator plane to be less than 0.2. Here the eccentricity is defined as the positive root of $c = (1 - b^2/a^2)^{1/2}$ where a and b are the major and minor axes of an ellipse that best fits the observed magnetospheric cross section in the terminator plane. Observe that $c = 0.2$ corresponds to a value of 1.02 for a/b , i.e., the approximating elliptic cross section is very nearly circular. Most importantly, predicted results based upon an axisymmetric magnetopause shape have repeatedly been found to be in good agreement with observations of the location of the bow wave and of the plasma and magnetic field

*President, Associate Fellow AIAA
**Research Scientist
†Professor, Fellow AIAA
††Scientist

properties throughout the magnetosheath of the earth. The same result has also been found at the other terrestrial planets.¹⁰

Although only limited data, all obtained near the planetary equatorial plane, and associated theoretical analyses are currently available for Jupiter and Saturn, the agreement between the predictions and observations has been found to be clearly inferior to that for the terrestrial planets. In a comprehensive study of the positions of the Jupiter and Saturn bow shocks, Slavin et al.³ showed that the bow shock locations predicted by the axisymmetric model using the observed equatorial shape of the magnetopause are substantially farther from the magnetosphere nose than those actually observed. As shown in Figure 1, the resulting magnetosheath thickness in the subsolar region is 45% too great for Jupiter and 20% too great for Saturn. Slavin et al.³ attributed these differences to a substantial departure from axisymmetry in the magnetospheric shapes for these planets. In this view, the polar regions of the magnetopause are considerably flattened with respect to the equatorial regions by effects, presumably, of a large equatorial current system¹¹ brought about by the substantial centrifugal effects associated with the high spin rates and large size of these planets.

On the basis of the available information, Slavin et al.³ suggested the polar flattening hierarchy illustrated in Figure 2 for the magnetopause cross sections in the terminator plane. As shown, the cross section of the earth's magnetosphere is nearly circular with $0.98 < b/a < 1.00$ corresponding to an eccentricity $e \leq 0.2$, whereas that for the Jovian magnetosphere is flattened into approximately an ellipse with $b/a \sim 0.6$ corresponding to $e \sim 0.8$. The corresponding values for Saturn were not determined to an equal precision, but it was concluded that this planet presents an intermediate case with $0.6 < b/a < 1.00$, or $e < 0.8$.

The polar flattening hypothesis is consistent with most of the results shown in Figure 1 since the axisymmetric shape that results from rotating the observed equatorial magnetopause trace about the symmetry axis produces a shape that has significantly greater cross-section area than a flattened shape having the same equatorial magnetopause trace. As a result, the bow shock about an axisymmetric magnetopause will be everywhere farther from the magnetopause than it is for a polar flattened magnetopause having the same equatorial shape, just as observed for Jupiter and near the magnetopause nose for Saturn. The reason for the pronounced flaring of the Saturnian bow wave near the terminator plane as shown in Figure 1 is not known, but the amount of data on which this result is based is so small that it may, in fact, be an erroneous steady-state interpretation of data obtained over times of significant temporal variations.

To provide the appropriate theoretical solutions for application to such flattened magnetospheres, we have extended our previous analysis so that it can be applied to the interaction of the solar wind flow with a general three-dimensional magnetospheric obstacle. This

extension serves the dual purpose of providing (a) more accurate theoretical results required for comparative studies with observations of the solar wind interaction with substantially nonaxisymmetric magnetospheres, such as those of Jupiter and Saturn, and (b) an important element of a general interactive scheme in which the three-dimensional shape of the magnetopause and the surrounding flow and magnetic fields for any planet are calculated alternately in the process of converging toward an exact solution of the magnetohydrodynamic equations.

In this paper, the new computational model is described and results are presented for the shape of the bow wave and the flow properties in magnetosheaths of polar flattened magnetopauses representative of Jupiter and Saturn. Through a parametric study in which the amount of polar flattening is varied, a quantitative determination is obtained of the degree of flattening at both Jupiter and Saturn. The new three-dimensional results are shown to be in good agreement with the observations, and account for most of the differences between the observations and the axisymmetric model results.

Mathematical Model and Solution Procedure

The fundamental assumption underlying the present work, as in the previous analyses of axisymmetric flows reported in the references cited above, is that the average bulk properties of the solar wind flow around a planetary magnetosphere can be described adequately by solutions of the continuum equations of magnetogasdynamics of a perfect gas having infinite electrical conductivity and zero viscosity and thermal conductivity. The primary justification for this assumption is provided not by rigorous proof but by the outstanding general agreement of the calculated results with a large amount of direct observations in space.

Under this assumption, the equations used to describe the flow of the solar wind plasma past a planetary magnetosphere are those of single-fluid dissipationless magnetohydrodynamics for the conservation of mass, momentum, energy, and magnetic flux, augmented by the equation of state for a perfect gas and by entropy considerations. These equations have been given many times (see Reference 2 for our most recent account), and will not be repeated here.

For typical solar wind conditions, and particularly at the locations of the outer planets, both the oncoming sonic Mach number $M_{S\infty} = V_{\infty}/(\gamma P_{\infty}/\rho_{\infty})^{1/2}$ and Alfvén Mach number $M_{A\infty} = V_{\infty}/(B_{\infty}^2/(4\pi\rho_{\infty}))^{1/2}$ are high (of the order of 10). Under these conditions, an important simplification of the magnetohydrodynamic equations occurs because the magnetic terms may be disregarded as small in the momentum and energy conservation equations. With these terms omitted, the magnetogasdynamic equations separate into two sets: the ordinary gasdynamics equations for the flow of a perfect gas, and the Faraday magnetism equations. The equations for the fluid motion about an obstacle of given shape thereby reduce to those of gasdynamics, and can be solved without

further consideration of the magnetic field. The magnetic field can be determined subsequently by solving the remaining Faraday equations using the values for the velocity and density fields already calculated. The magnetic field determined in this fashion is usually interpreted, somewhat ambiguously, as being 'frozen-in' or 'moving with the fluid'. The resulting equations and the model they represent are commonly referred to as the gasdynamic convected field approximation. It should be noted, however, that the interpretation of the field as frozen-in or moving with the fluid is not dependent upon the separation of the fluid motion determination from the magnetic field determination, but is actually an exact consequence of the basic assumption that the flow can be represented by the magnetohydrodynamic equations for a perfect dissipationless electrically conducting gas.

In carrying out the decoupled gasdynamic calculation, the shape of the magnetopause is not known a priori, but must be found as part of the overall solution. In our previous analyses, the magnetopause shape has been determined by either an independent approximate theoretical analysis, a synthesis of actual observational results, or a combination thereof. This latter procedure has also been employed in the present analysis.

Computational methods based on the full magnetohydrodynamic equation set now exist, but are still in a preliminary state of development and lack adequate resolution for many purposes. Hence, Russell⁴ has recently stated, "Currently, the only way to achieve the spatial resolution needed for a useful comparison with data obtained on a pass through a planetary magnetosheath is to employ the gasdynamic convected field model".

One of the most important and unique features of both the current three-dimensional and previous axisymmetric models is the use of two separate, but coupled, computational procedures for determining the steady flow field. As illustrated in Figure 3, the model is composed of an obstacle nose region solver that determines the flow field from the subsolar region to or somewhat beyond the terminator location by using an unsteady procedure that marches the solution forward in time to obtain the asymptotic steady state solution. That solver is then linked together with a spatially-marching tail region solver that advances the flow field solution downstream to any arbitrary distance in which the flow remains supersonic.

The precise axial location at which the two solutions are joined is relatively arbitrary, with the single requirement being that at all points on the joining plane the axial component of the local sonic Mach number be supersonic. This is the basic requirement of the spatially-marching solver. In most of our previous applications, it was convenient to select for the joining location the plane through the planetary center oriented normal to the oncoming solar wind direction, i.e., the terminator plane. In some cases involving magnetopause obstacles that possess considerable flare at the terminator, it is necessary to locate the joining plane at some fraction of an obstacle nose radii downstream of the terminator in

order to satisfy the requirement of supersonic axial Mach number.

The reasons for expanding the substantial additional development effort to achieve such a coupled two-flow solver combination, rather than employ a single time-marching solver for the entire flow field as is done in all existing magnetohydrodynamic solutions procedures, are twofold. First, there is the huge gain in computational efficiency since the computationally expensive time-marching procedure required to treat the subsonic/transonic flow in the nose region is used only where needed, while the remainder of the solution is obtained using a highly efficient spatially marching procedure appropriate for supersonic flow. Secondly, the computational capability is attained to determine flow conditions as arbitrarily far downstream as needed. Such a capability cannot be provided by a time-marching procedure. Finally, we note that such a subdivision of both flow field and solution procedures is not uncommon in calculating supersonic/hypersonic flows and has been used extensively not only in all our previous work, but also for example, in the analysis of reentry flows including space shuttle applications.

Nose Region Solution Procedure

In the nose region, we have adapted the procedure of Rizk et al.² to solve the unsteady, three-dimensional dissipationless gasdynamic partial differential equations governing the conservation of mass, momentum, and energy. Upon introduction of the generalized independent variable transformation $\tau = t$, $\xi = \xi(x,y,z)$, $\eta = \eta(x,y,z)$, $\zeta = \zeta(x,y,z)$, these equations can be written in strong conservation law form as:

$$\hat{Q}_\tau + \hat{E}_\xi + \hat{F}_\eta + \hat{G}_\zeta = 0 \quad (1)$$

where

$$\hat{Q} = \frac{1}{J} \begin{bmatrix} \rho \\ \rho u \\ \rho v \\ \rho w \\ e \end{bmatrix} \quad \hat{E} = \begin{bmatrix} \rho u \\ \rho u^2 + \xi_x p \\ \rho u v + \xi_x p \\ \rho u w + \xi_x p \\ (e+p)u \end{bmatrix}$$

$$\hat{F} = \frac{1}{J} \begin{bmatrix} \rho v \\ \rho u v + \eta_x p \\ \rho v^2 + \eta_y p \\ \rho v w + \eta_z p \\ (e+p)v \end{bmatrix} \quad \hat{G} = \begin{bmatrix} \rho w \\ \rho u w + \zeta_x p \\ \rho v w + \zeta_y p \\ \rho w^2 + \zeta_z p \\ (e+p)w \end{bmatrix} \quad (2)$$

Here (u,v,w) are the Cartesian velocity components, ρ and p are density and pressure, e is the internal energy and is related to pressure by $p = (\gamma-1)[e - \rho(u^2 + v^2 + w^2)/2]$, where γ is the ratio of specific heats, (U,V,W) are the contravariant velocities without metric normalization and are given by

$$\begin{bmatrix} U \\ V \\ W \end{bmatrix} = \begin{bmatrix} u\xi_x + v\xi_y + w\xi_z \\ u\eta_x + v\eta_y + w\eta_z \\ \zeta_\tau + u\zeta_x + v\zeta_y + w\zeta_z \end{bmatrix} \quad (3)$$

where (ξ_x, ξ_y, ξ_z) , (η_x, η_y, η_z) , $(\zeta_x, \zeta_y, \zeta_z)$ are the transformation metrics and J is the Jacobian of the transformation. At each time step the transformation metrics are unknown and must be determined as part of the solution. In our implementation, they are evaluated numerically using second-order central differences. The time dependent metric terms are functions of the instantaneous shock speed, which is determined from the shock fitting procedure of Kutler et al.¹⁴

The numerical algorithm used to solve the above equations is based on the Beam and Warming¹⁵ procedure. The method is employed in delte form and is fully implicit, noniterative, second-order accurate in space, and spatially factored. When applied to equation (1), the algorithm can be written as:

$$\begin{aligned}
 & [I + \Delta t \delta_{\xi} \hat{A} - \epsilon_1 J^{-1} \nabla_{\xi} \Delta_{\xi} J] \cdot [I + \Delta t \delta_{\eta} \hat{B} - \epsilon_1 J^{-1} \nabla_{\eta} \Delta_{\eta} J] \cdot \\
 & [I + \Delta t \delta_{\zeta} \hat{C} - \epsilon_1 J^{-1} \nabla_{\zeta} \Delta_{\zeta} J] \Delta \hat{q} = -\Delta t [\delta_{\xi} \hat{E} + \delta_{\eta} \hat{F} + \delta_{\zeta} \hat{G}] \\
 & - \epsilon_e J^{-1} [(\nabla_{\xi} \Delta_{\xi})^2 + (\nabla_{\eta} \Delta_{\eta})^2 + (\nabla_{\zeta} \Delta_{\zeta})^2] J \hat{q} \quad (4)
 \end{aligned}$$

where $(\hat{A}, \hat{B}, \hat{C})$ are the Jacobian matrices $\hat{A} = \partial \hat{E} / \partial \hat{q}$, $\hat{B} = \partial \hat{F} / \partial \hat{q}$, $\hat{C} = \partial \hat{G} / \partial \hat{q}$, $\Delta \hat{q} = (q/J)^{n+1} - (q/J)^n$ where n represents the time level, $(\delta_{\xi}, \delta_{\eta}, \delta_{\zeta})$ represent second-order central difference operators, (ϵ_1, ϵ_e) are implicit second-order and explicit fourth-order smoothing parameters, (∇, Δ) represent first-order backward and forward difference operators, and t is the time step. A single time step integration of equation (4) consists of three separate inversion steps associated with each of the three spatial directions (ξ, η, ζ) . Each inversion step involves the solution of a 5×5 block tridiagonal system. Integration step size is established by using the maximum eigenvalue of the Jacobian matrices $(\hat{A}, \hat{B}, \hat{C})$.

The analysis is initiated by introducing a computational mesh to discretize the flow field. For the present three-dimensional model as well as in all our previous work, we employ a fitted discontinuity surface representation of both the bow shock and the magnetospheric obstacle. For application to three-dimensional planetary magnetospheres we have found it convenient to develop a mesh generator based upon a generalized spherical (r, θ, ϕ) coordinate system with the origin usually located at the planetary center, but occasionally shifted downstream from that location on a line through the planetary center and parallel to the oncoming solar wind.

The associated Cartesian (x, y, z) coordinate axes and a typical grid employed in our analysis are illustrated in Figure 4 where a perspective cut out view of one quadrant of the flow field is provided. In that figure the origin coincides with a location approximately half of an obstacle radius downstream of the planetary center and the x -axis, which coincides with the longitudinal axis of the magnetosphere, points directly into the oncoming solar wind. The y axis lies in the planetary equatorial plane, and the z axis points in the north polar direction. In Figure 4, the

obstacle to shock (r, θ) grids in the azimuthal planes containing the x - z ($\phi = 0^\circ$) and x - y ($\phi = 90^\circ$) axes are shown together with the mesh distribution on the magnetopause surface, and the outflow boundary grid located in the y - z plane at the final downstream x location.

The quadrant of the (r, θ, ϕ) mesh shown in Figure 4 contains $(19, 30, 9)$ points, with the 9 azimuthal planes spaced at equal 10° increments. In each azimuthal plane, the capability of generating a body normal mesh has been implemented in the grid generator. A clustering capability has also been implemented to enable independent grid point clustering in each of the three coordinate directions. For the magnetospheric obstacle shown in Figure 4, which represents a polar flattened Jupiter magnetopause with $a/b = 1.75$, the equal angular distribution of the azimuthal planes results in a natural clustering of the grid spacing on the body in the polar region in contrast to that in the equatorial region. This can be retained or easily modified if desired by employing the clustering option.

Boundary conditions necessary for specifying a properly posed mathematical problem are that the flow satisfy the unsteady Rankine-Hugoniot shock relations along the moving bow shock surface, be entirely supersonic at the downstream outflow boundary, be symmetric about the stagnation streamline at the nose, and be tangential to the obstacle at its surface. Initial flow field conditions are determined by use of an approximating surface for the bow shock wave, and by prescribing a modified Newtonian pressure distribution on the surface of the magnetopause. Since the maximum entropy streamline wets the obstacle, that fact plus the flow tangency condition on the magnetopause serve to determine the remainder of the flow properties on that surface. A linear variation for the flow properties between the bow shock and the magnetopause then provides the starting flow field which is then integrated in a time-asymptotic fashion until the steady state solution is obtained.

At the boundaries, modification of the differencing algorithm to account for the appropriate conditions described above is accomplished as follows. For the fitted discontinuity surface representing the bow shock, the flow variables immediately downstream of the shock are determined using the unsteady shock fitting procedure of Kutler et al.¹⁴ At the outflow boundary where the flow is entirely supersonic, the dependent variables are determined by extrapolation from the adjacent interior points. Along the stagnation streamline, which forms a singularity line due to our use of a spherical-like coordinate system¹⁵, symmetry conditions are enforced by employing a second-order accurate averaging procedure. Also incorporated in the numerical solver is the capability to enforce symmetry boundary conditions across any two arbitrary azimuthal planes. For the present application, all members of the family of three-dimensional obstacles being considered possess quadrilateral symmetry about two orthogonal azimuthal planes passing through the equatorial and polar meridians. Consequently, the flow calculations can be restricted to a single

quadrant as shown in Figure 4, thereby reducing by a factor of four the number of grid points at which the solution must be determined. The obstacle surface flow tangency condition is incorporated by setting the contravariant velocity component normal to the surface equal to zero, and then determining the other two contravariant velocity components and the density at the obstacle surface by extrapolation from interior points. The total energy is then evaluated by using the information together with the pressure computed from the normal momentum equation. The interior flow field bounded by these various boundaries is treated in shock-capturing fashion and therefore allows for the accurate determination of secondary shocks should any occur.

Tail Region Solution Procedure

In the tail region, we have employed the shock capturing technique of Kutler et al.¹⁶ to solve the steady, three-dimensional dissipationless gasdynamic equations. The conservation equations for mass and momentum written in weak conservation law form in cylindrical (x, R, ϕ) coordinates can be written as:

$$\bar{U}_x + \bar{F}_R + \bar{G}_\phi + \bar{H} = 0 \quad (5)$$

where the four-component vectors $(\bar{U}, \bar{F}, \bar{G}, \bar{H})$ are defined by

$$\bar{U} = \begin{bmatrix} \rho u \\ \rho u^2 \\ \rho uv \\ \rho uw \end{bmatrix} \quad \bar{F} = \begin{bmatrix} \rho v \\ \rho uv \\ \rho v^2 \\ \rho vw \end{bmatrix}$$

$$\bar{G} = \begin{bmatrix} \rho w \\ \rho uw \\ \rho vw \\ \rho w^2 \end{bmatrix} \quad \bar{H} = \begin{bmatrix} \rho v \\ \rho uv \\ \rho(v^2 - w^2) \\ 2\rho vw \end{bmatrix} \quad (6)$$

in which (u, v, w) denote velocity components in the (x, R, ϕ) coordinate directions. The governing set of equations is completed with the addition of energy conservation as given by the equation for the total enthalpy

$$H_t = h(\rho, p) + q^2/2 = \text{const} \quad (7)$$

Here q is the magnitude of the velocity vector and $h(\rho, p)$ represents the static enthalpy which for a perfect gas is given by $[\gamma/(\gamma-1)](p/\rho)$.

The governing equations are transformed to a computational space using the independent variable transformation $\xi = x$, $\eta = (R-R_b)/(R_S-R_b)$, $\zeta = \phi$, where (R_S, R_b) represent the cylindrical radial coordinate of the bow shock and body surface, respectively, and ϕ is the azimuthal angle. This yields the conservation equation

$$D_\xi + F_\eta + G_\zeta + \bar{H} = 0 \quad (8)$$

where

$$\bar{U} = \bar{U}$$

$$\bar{F} = \frac{(\bar{F} - [R_b + \eta(R_S - R_b)]_\xi \bar{U} - [R_b \zeta + \eta(R_S - R_b)_\zeta] \bar{G})}{R_S - R_b}$$

$$\bar{G} = \bar{G}$$

$$\bar{H} = \bar{H} + \frac{[(R_S - R_b)_\xi \bar{U} + (R_S - R_b)_\zeta \bar{G}]}{R_S - R_b} \quad (9)$$

The numerical algorithm chosen to solve equation (8) is MacCormack's explicit second-order accurate predictor-corrector method. As applied to equation (9), the algorithm can be written as:

$$\bar{U}_{i,j}^* = \bar{U}_{i,j}^n - \frac{\Delta \xi}{\Delta \eta} (\bar{F}_{i+1,j}^n - \bar{F}_{i,j}^n) - \frac{\Delta \xi}{\Delta \zeta} (\bar{G}_{i,j+1}^n - \bar{G}_{i,j}^n) - \Delta \xi \bar{H}_{i,j}^n$$

$$\bar{U}_{i,j}^{n+1} = \left(\frac{1}{2}\right) (\bar{U}_{i,j}^n + \bar{U}_{i,j}^* - \frac{\Delta \xi}{\Delta \eta} (\bar{F}_{i,j}^* - \bar{F}_{i-1,j}^*) - \frac{\Delta \xi}{\Delta \zeta} (\bar{G}_{i,j+1}^* - \bar{G}_{i,j-1}^*) - \Delta \xi \bar{H}_{i,j}^*) \quad (10)$$

where

$$\bar{U}_{i,j}^n = \bar{U}^n(\eta \Delta \xi, i \Delta \eta, j \Delta \zeta), \bar{F}_{i,j}^n = \bar{F}(\bar{U}_{i,j}^n, \eta \Delta \xi, i \Delta \eta, j \Delta \zeta)$$

$$\bar{F}_{i,j}^* = \bar{F}(\bar{U}_{i,j}^*, (\eta+1) \Delta \xi, i \Delta \eta, j \Delta \zeta), \text{ etc.}$$

Subsequent to each integration step of equation (10) with respect to the hyperbolic marching coordinate ξ , the physical flow variables (ρ, p, u, v, w) must be decoded from the components \bar{u}_i of \bar{U} . This necessitates the solution of five simultaneous nonlinear equations consisting of equation (7) together with the four elements $\bar{u}_i = (\rho u, \rho u^2, \rho uv, \rho uw)$. For a perfect gas, the procedure yields a quadratic equation that can be solved for the supersonic velocity component u . The remaining physical variables can then be determined directly.

At the bow shock, the fitted shock discontinuity approach of Thomas et al.¹⁷ is employed, while at the obstacle surface the surface tangency condition is enforced by applying the method of Abbett.¹⁸ Integration step size in the marching direction is redetermined at each ξ location so as to allow the maximum possible step size consistent with stability.

The numerical calculations for which results are reported here were performed on the NASA Ames Research Center CRAY XMP computer facility. Approximately 20 to 30 minutes of CPU time were

typically required for the calculations for a single case of the three-dimensional magnetosphere shapes considered in this study. Essentially all of this time is spent with the nose region solver. For the family of three-dimensional shapes studied, the tail region solver is extremely rapid and can carry the solution downstream 10 obstacle nose radii in typically less than 10 CPU seconds. As a final runtime comparison, we note that the typical CRAY XMP CPU time required for a single case by the combined nose and tail axisymmetric model to determine an analogous flow field is approximately 15 seconds.

Results and Applications to Jupiter and Saturn

Figure 5 shows the calculated results for the magnetopause and bow wave locations for the conditions suggested by Slavin et al.³ as representative for Jupiter. These are that the flow has a free-stream sonic Mach number $M_{S\infty}$ of 10 and ratio of specific heats γ of 2.0, and the magnetopause has an elliptic cross section with constant ratio of major to minor axes a/b of 1.75, corresponding to an eccentricity e of 0.821. The equatorial magnetopause profile is taken to approximate that deduced from observations at Jupiter. Calculation of a converged solution for these conditions has been carried out over the region extending from the nose of the bow wave to about 1 magnetopause nose radius downstream of the planetary center, or about $6R_J$ Jupiter radii. The results, in the form of traces of the magnetopause and the bow shock wave in (a) each of the ten azimuthal grid planes from the equatorial to the polar planes of symmetry and (b) the terminator plane, display that the flattening of the bow wave is much less than that of the magnetopause.

Details of this three-dimensional flow field are presented in Figure 6. In that figure, contour plots of the density ρ/ρ_∞ , pressure p/p_∞ , temperature T/T_∞ , flow speed v/v_∞ , and the sonic Mach number M_S in the polar and equatorial planes, with an isometric drawing of the magnetopause and bow shock wave in the equatorial and noon-midnight meridian planes are given.

Figure 7 presents a comparison of the Jovian magnetopause and bow shock shapes observed near the equatorial plane³ with the bow shock shapes calculated for the same equatorial magnetopause shape for four values for a/b , namely 1.00 (circular cross section), 1.50, 1.75, and 2.00, that bracket the value of $5/3$ suggested by the observations. The results show that the bow wave is farthest out for the axisymmetric magnetosphere and moves progressively nearer as the flattening of the magnetospheric cross section increases. This is as appropriate since the cross-section area of the magnetosphere is largest for the axisymmetric case, and diminishes progressively as the magnetopause is flattened from a/b of 1.00 to 2.00, thereby presenting less of an obstruction to the flow.

Comparison with the observations for Jupiter show that they are in excellent agreement with the calculated results for $a/b = 1.75$, the magnetospheric shape with elliptic cross-section closest

to that proposed for Jupiter by Slavin et al.³ This finding is also consistent with the result of Engle and Beard,¹ in which the three-dimensional shape of the Jovian magnetosphere was calculated for a planetary dipole field supplemented by an equatorial current sheet chosen to reproduce the observed Jovian magnetic field near the equatorial plane. All of this confirms the general expectation that, provided the solution is determined for a suitably flattened magnetopause, the gasdynamic-convected field model should provide an even better representation for the magnetosheath flow at Jupiter than at earth because of the high sonic and Alfvénic Mach numbers that prevail there.

Figure 8 shows the corresponding results for conditions suggested by Slavin et al.³ as representative of Saturn. These are that the flow has a free-stream sonic Mach number $M_{S\infty}$ of 12, a value of 2.0 for the ratio of specific heats γ , and is about a magnetopause having the indicated shape in the equatorial plane and an elliptic cross section with constant ratio of major to minor axes a/b somewhere between that for the earth and Jupiter. Calculated equatorial plane traces of the bow shock wave are presented for magnetopause shapes with $a/b = 1.00$ (circular cross section), 1.15, 1.25, 1.35, and 1.45 together with a best-fit curve to the observations at Saturn³.

The results for $a/b = 1.25$ match the observations well near the nose of the bow shock wave, but depart significantly before the planetary terminator plane is reached. The observed bow wave flares out much farther from the planet than not only the calculated results for $a/b = 1.25$, but the results for all the calculated cases, including those for an axisymmetric magnetopause. This observation is surprising in view of the generally satisfactory agreement between the results of the gasdynamic calculations and the observations for all the other planets, and the reason for it remains unknown.^{3,4} It may be indicative of some significant physical process not included in the analysis, or it might simply be an insignificant artifact resulting from the interpretation of a small number of observations and of temporal changes in conditions occurring at the time they were made.

Conclusions

The development of a computational model for determining the solution of the gasdynamic portion of the gasdynamic convected magnetic field model for solar wind flow past three-dimensional magnetopauses of nonaxisymmetric shape is described. Specific application of the model is made to Jupiter and Saturn where, as inferred from observations, significant polar flattening of the magnetopause cross sections exists. Results from the new three-dimensional model converge continuously to those calculated previously for axisymmetric magnetospheres that were determined using completely different computational procedures, thereby verifying the accuracy of both methods.

Because the cost of determining these three-dimensional solutions is a hundred times greater than for axisymmetric flows, and the differences between the results are small for small departures from axisymmetry, we suggest that the axisymmetric model be used whenever the magnetopause cross section is nearly circular, and that the new nonaxisymmetric model be employed only for those cases in which substantial departures from axisymmetry exist. Examples of the latter are Jupiter and Saturn, for which previous comparisons between the observations and results calculated for axisymmetric magnetospheres were shown to be in substantially poorer agreement with observations than for the terrestrial planets.

Similar comparison of results from the new model for a parametric study of three-dimensional nonaxisymmetric magnetospheres having elliptic cross sections of various eccentricities representative of Jupiter and Saturn provide a new estimate of the amount of polar flattening present in the magnetospheres of these planets. It is found that essentially perfect agreement with the observational data is obtained for Jupiter when a value of 1.75 is used for the ratio a/b of major to minor axes of the cross section. For Saturn, similarly good agreement with the observational data is found in the nose region when a value of 1.25 is used for a/b. Both of these values are in good agreement with previous estimates for a/b based on other considerations.

Near the terminator region of Saturn, however, scanty observational evidence indicates that the Saturnian bow wave may flare out considerably more than indicated by any of the model predictions, including that for the axisymmetric case. It remains unknown whether this difference is indicative of some significant process peculiar to Saturn not included in the analysis, or a meaningless artifact of the steady-state interpretation of the observations caused by temporal or other changes in conditions at the time the observations were made at that planet.

Acknowledgements

This research was jointly supported by NASA Contract NASW-4135, NASA Grant NAGW 278, and by Air Force Office of Scientific Research Contract F49620-86-C-0035. CRAY XMP computational time was provided by the Applied Computational Fluids Branch at NASA/Ames Research Center under a Memorandum of Understanding with NASA Headquarters.

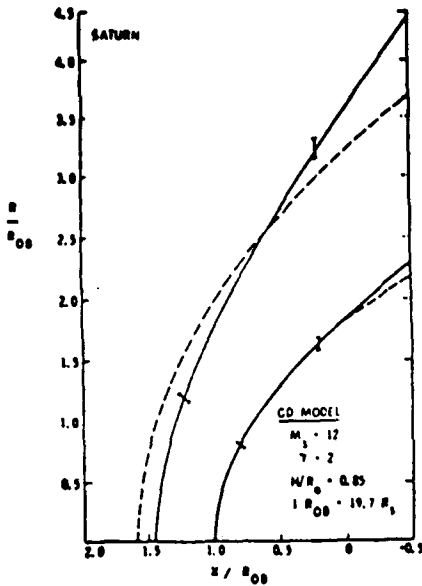
References

1. Spreiter, J.R., A.L. Summers, and A.Y. Alksne, Hydromagnetic flow around the magnetosphere, *Planet. Space Sci.*, Vol. 14, pp. 223-253, 1966.
2. Spreiter, J.R., and S.S. Stahara, Magneto-hydrodynamic and gasdynamic theories for planetary bow waves, in Collisionless Shocks in the Heliosphere, Review of Current

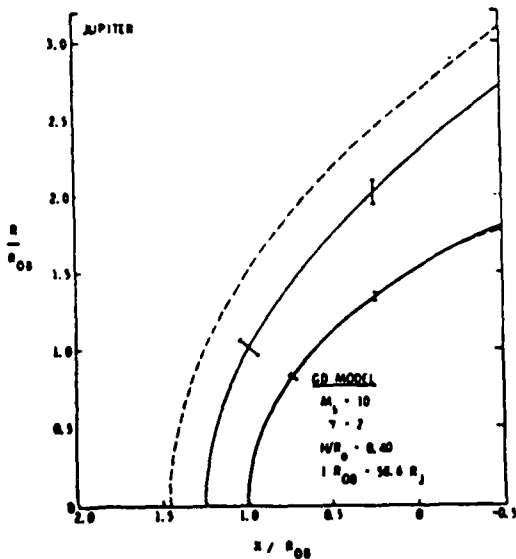
Research, edited by B.T. Tsurutani and R.G. Stone, pp. 85-107, AGU Geophysical Monograph 35, 1985.

3. Slavin, J.A., Smith E.J., Spreiter, J.R. and Stahara, S.S., Solar wind flow about the outer planets: gas dynamic modeling of the Jupiter and Saturn bow shocks, *J. Geophys. Res.*, Vol. 90, pp. 6275-6286, 1985.
4. Russell, C.T., Planetary bow shocks, in Collisionless Shocks in the Heliosphere, Review of Current Research, edited by B.T. Tsurutani and R.G. Stone, pp. 107-130, AGU Geophysical Monograph 35, 1985.
5. Spreiter, J.R., and S.S. Stahara, A new predictive model for determining solar wind-terrestrial planet interactions, *J. Geophys. Res.*, Vol. 85, pp. 6769-6777, 1980.
6. Spreiter, J.R., and S.S. Stahara, Solar wind flow past Venus: Theory and comparisons, *J. Geophys. Res.*, Vol. 85, pp. 7715-7738, 1980.
7. Stahara, S.S., D. Klenke, B.C. Trudinger, and J.R. Spreiter, Application of advanced computational procedures for modeling solar-wind interactions with Venus - Theory and computer code, NASA CR-3267, 1980.
8. Fairfield, D.H., Average and unusual locations of the earth's bow shock and magnetopause, *J. Geophys. Res.*, Vol. 86, pp. 6700-6716, 1971.
9. Slavin, J.A., and R.E. Holzer, Solar wind flow about terrestrial planets 1. Modeling bow shock position and shape, *J. Geophys. Res.*, Vol. 87, pp. 11401-11418, 1981.
10. Slavin, J.A., Holzer, R.E., Spreiter, J.R., Stahara, S.S. and Chaussee, D.S., Solar wind flow about the terrestrial planets 2. Comparison with gas dynamic theory and implications for solar-planetary interactions, *J. Geophys. Res.*, Vol. 88, pp. 19-35, 1983.
11. Engle, I.M., and D.B. Beard, Idealized Jovian magnetosphere shape and field, *J. Geophys. Res.*, Vol. 85, pp. 579-592, 1980.
12. Rizk, Y.M., J.N. Scott and R.K. Newman, Numerical simulation of viscous supersonic flows in the vicinity of embedded subsonic or axially separated regions, Vols. I and II, AFWAL-TR-83-3113, 1983.
13. Beam, R.M., and R.F. Warming, An implicit factored scheme for the compressible Navier-Stokes equations, AIAA Paper 77-645, 1977.
14. Kutler, P., J.A. Pedelty, and T.H. Pulliam, Supersonic flow over three-dimensional ablated nosetips using an implicit numerical procedure, AIAA Paper 80-63, 1980.
15. Pulliam, T. and J.L. Steger, On implicit time-difference simulations of three-dimensional flow, AIAA Paper 78-10, 1978.

16. Kutler, P., W.A. Reinhardt, and R.F. Warming, Multi-shocked three-dimensional supersonic flow fields with real gas effects, AIAA J., Vol. 11, pp. 657-664, 1973.
17. Thomas, P.D., M. Vinokur, R. Bastionon, and R.J. Conti, Numerical solution for the three-dimensional hypersonic flow field of a blunt body, AIAA J., Vol. 10, pp. 887-894, 1972.
18. Abbett, M.J., Boundary condition computational procedures for inviscid supersonic steady flow field calculations, Aerotherm Corp. Report 71-41, 1971.



b) Saturn bow shock comparison



a) Jupiter bow shock comparison

Fig. 1. Observations of the Jovian and Saturnian bow shock and magnetopause in the planetary equatorial plane compared with predictions (dashed lines) of the gasdynamic model with an assumed axisymmetric magnetopause

POLAR FLATTENING HIERARCHY

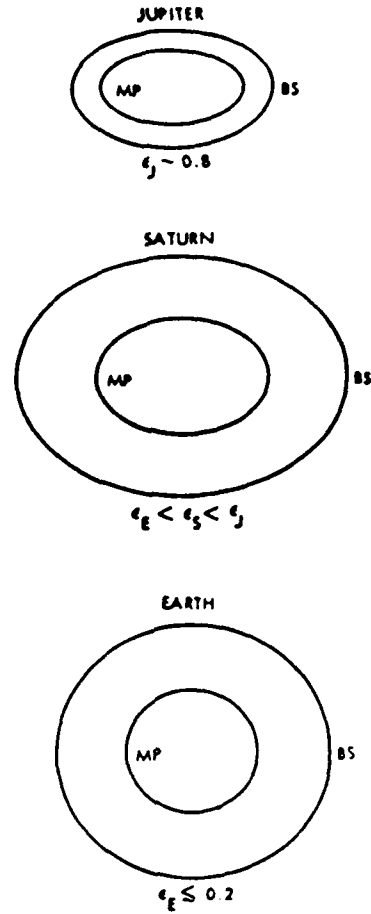


Fig. 2. A conceptual representation of magnetopause cross sectional shape based upon observations at the earth, theoretical magnetic field models at Jupiter, and interpretation of gasdynamic modeling results

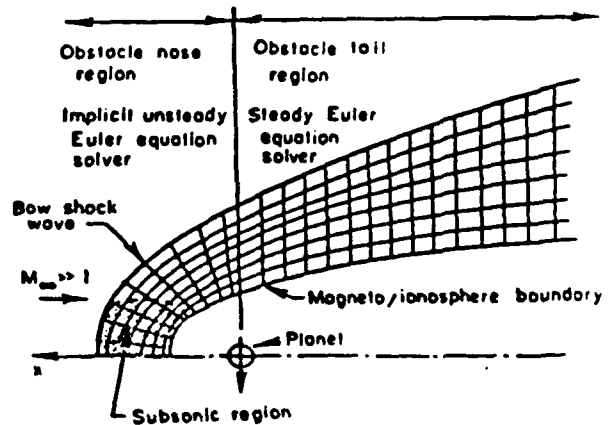


Fig. 3. Illustration of flow field subdivision and coupled flow solver combination incorporated in the 3-D solar wind/planetary interaction model

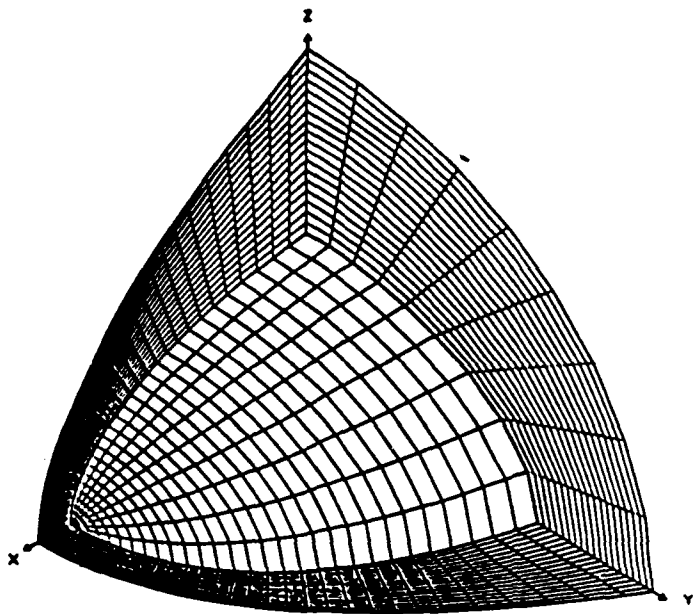


Fig. 4. Perspective cutout view of one quadrant of a typical computational grid employed in the 3-D model for the current study

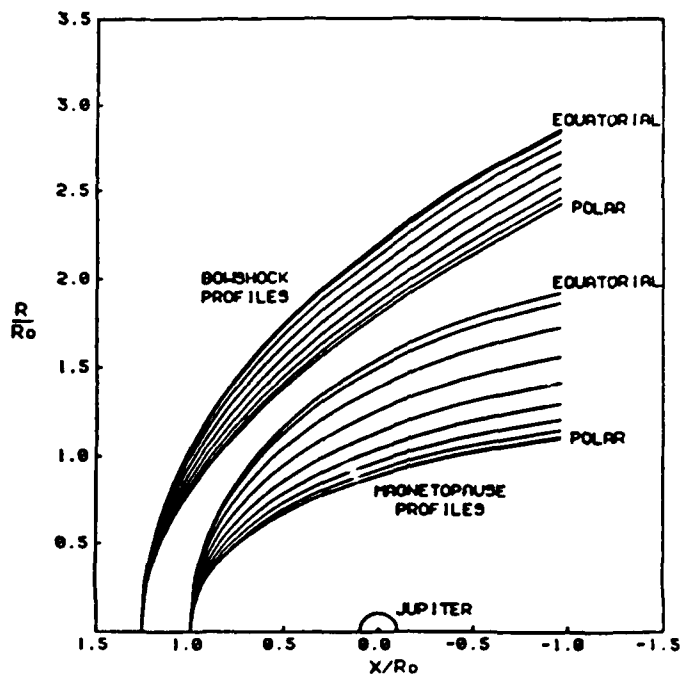


Fig. 5. Predicted bow shock and corresponding magnetopause locations in the 10 equally spaced azimuthal planes employed in the 3-D model for a polar flattened Jovian magnetopause having an elliptic cross section with $a/b = 1.75$ for $M_\infty = 10$ and $\gamma = 2.0$

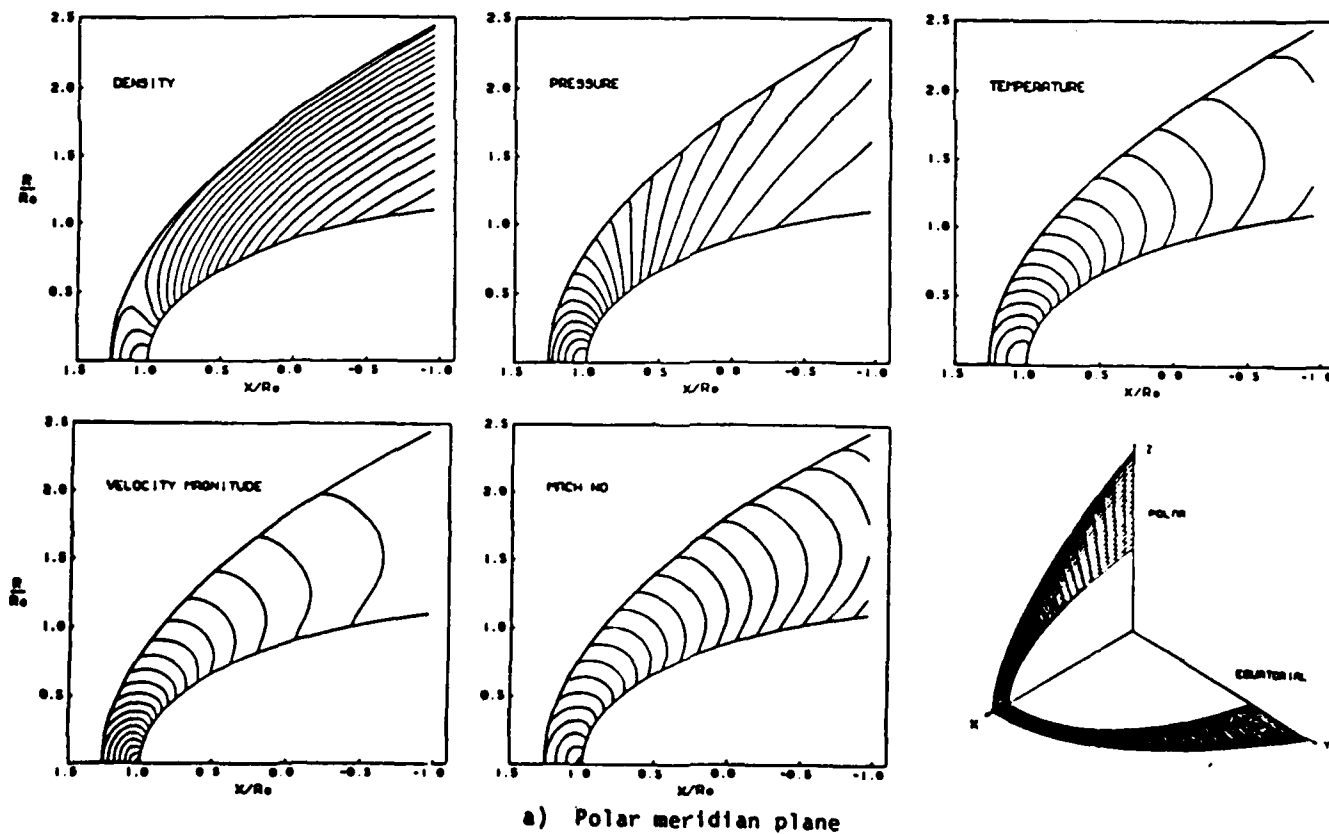
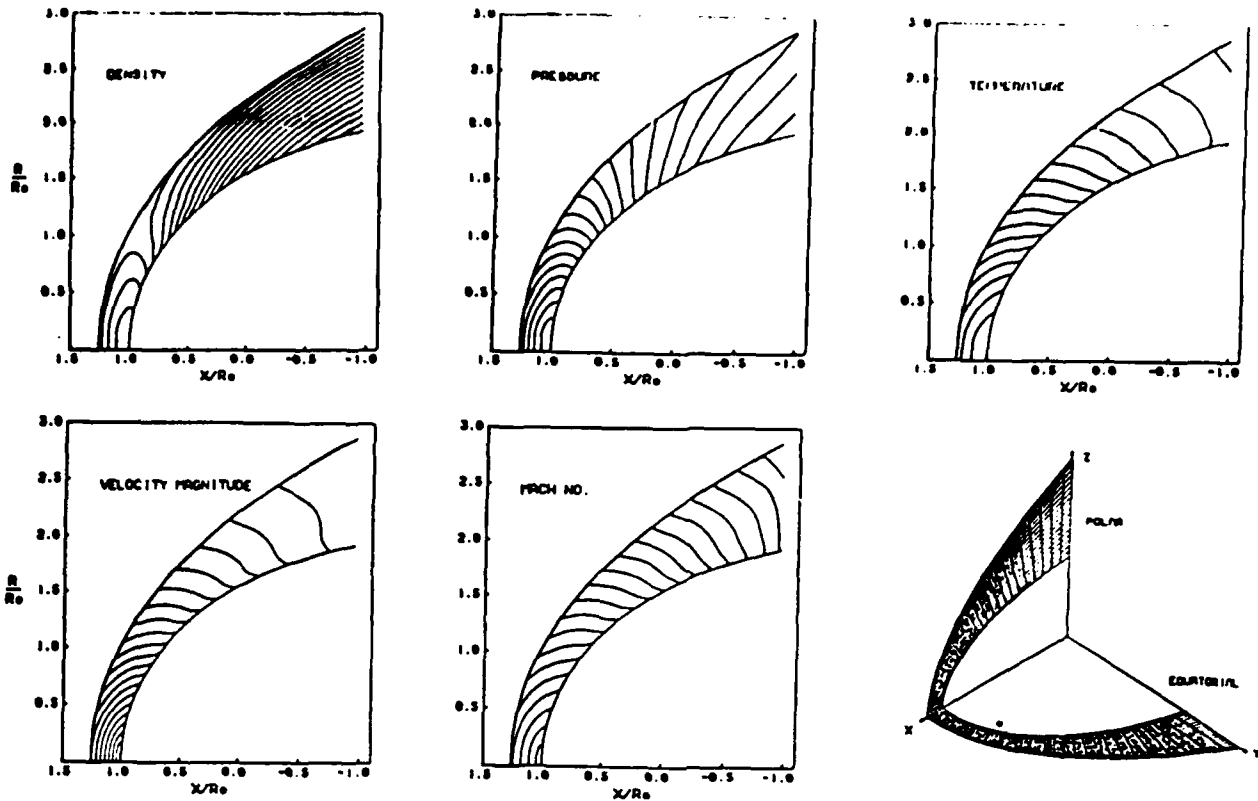


Fig. 6. Contours of density, pressure, temperature, velocity magnitude, and Mach number in the polar and equatorial meridian planes for the polar flattened Jovian magnetopause with $a/b = 1.75$ illustrated in Figure 5



b) Equatorial meridional plane
Fig. 6. (concluded)

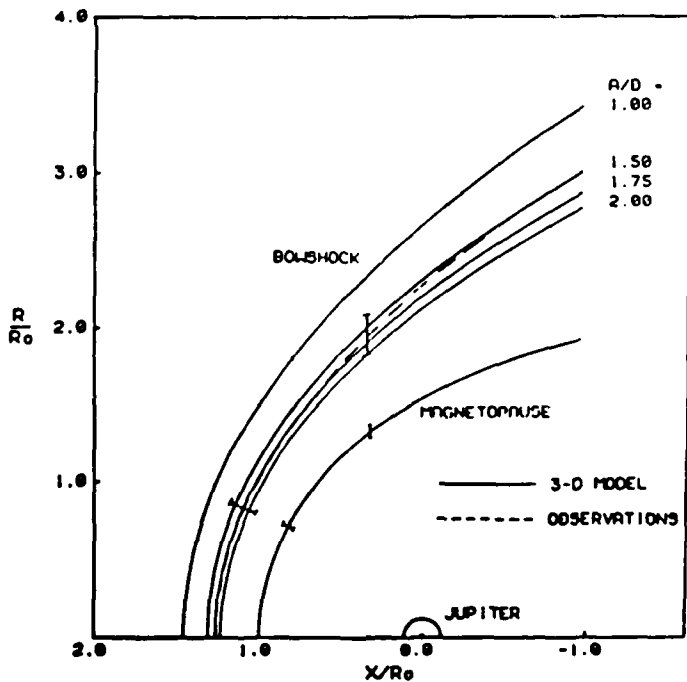


Fig. 7. Comparison of 3-D model predictions with observational data for the Jovian bow shock in the planetary equatorial plane for magnetopause shapes having elliptic cross sections with different ratios of major/minor axis a/b representing various amounts of polar flattening

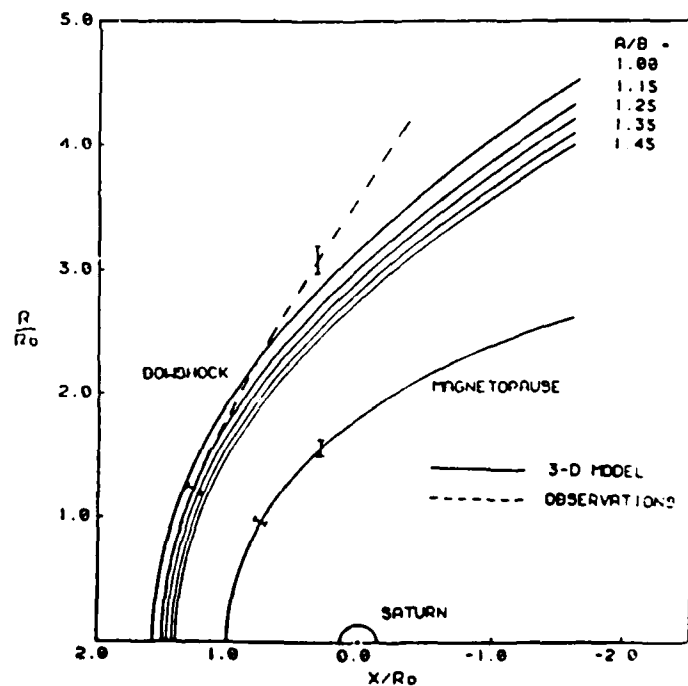


Fig. 8. Comparison of 3-D model predictions with observational data for the Saturnian bow shock in the planetary equatorial plane for magnetopause shapes having elliptic cross sections with different ratios of major/minor axis a/b representing various amounts of polar flattening

A NEW COMPUTATIONAL MODEL FOR THE PREDICTION OF MASS LOADING PHENOMENA FOR SOLAR WIND INTERACTIONS WITH COMETARY AND PLANETARY IONOSPHERES

Stephen S. Stahara*
RMA Aerospace, Inc., Mountain View, California

Gregory A. Molvik†
Sterling Federal Systems, Inc., Palo Alto, California

John R. Spreiter‡
Stanford University, Stanford, California

Abstract

The gasdynamic convected magnetic field model for predicting solar wind flows past a planetary magnetoionopause obstacle has been extended to apply to cometary or planetary obstacles for which significant ionization of atmospheric neutrals occurs in the surrounding solar wind flow. Because of the low density of the solar wind plasma, the presence of a neutral particle has no effect on the solar wind flow until the moment it becomes ionized, whereupon it makes itself evident as a mass, momentum, and energy addition to the flow. To account for the consequences, our existing gasdynamic convected magnetic field model was extended to include the effects of such additions to the flow. The need for such an extension is of paramount importance for applications to comets and can be of major significance for application to planets, such as Venus and possibly Mars that have sufficiently weak intrinsic magnetic fields that the effective planetary magnetoionopause would lie below the top of the sensible atmosphere.

A description of the computational procedures developed for the new mass loaded model is provided and results from a series of applications to both cometary and planetary bodies which involve a large degree of mass loading are presented. In order to verify the model, these results have purposely been obtained with a high degree of convergence and spatial resolution. The results indicate that as the mass loading is increased, the oncoming flow upstream of the bow wave becomes increasingly compressed, with the bow shock wave weakening and moving progressively farther upstream and away from the obstacle. The results are in accord with general physical considerations regarding source flow addition to supersonic flows and also with previous calculations of lesser resolution and accuracy. Significant corrections are provided for related results published recently by others.

Introduction

The gasdynamic convected magnetic field approximation to the magnetohydrodynamic model for supersonic solar wind flow past a planetary magnetoionosphere has provided a useful basis for understanding the solar wind planetary interaction process. From its inception more than two decades ago¹ to the present day (see e.g. Refs. 2,3 for recent reviews of the theory and applications), the

model has provided an increasingly useful tool for analyzing a number of phenomena arising from the interaction of the solar wind with planetary obstacles throughout the solar system.

The original model calculations, although accurate, were tedious to perform with the methods available at the time. As a result, solutions were carried out for only a limited number of cases. More recently, Spreiter and Stahara^{4,5} completely revised the solution procedures without changing the underlying physics in order to take advantage of the enormous advances in computer capability and computational methods that have occurred since the original model was conceived. The result is a well-documented model⁶ capable of routinely providing solutions for the location of the bow wave and the detailed flow and magnetic field properties throughout the magnetoionosphere region between the bow wave and a rather arbitrarily specified shape for the planetary magnetoionopause or ionopause.

The results provided by the model have proven useful in the interpretation of spacecraft data for all planets from Mercury to Jupiter. The ability of the numerical model to match the observed positions of the bow waves and magnetic fields of the Earth, Mars, and Mercury has been remarkably good. However, notable discrepancies were evident in the initial comparisons with observations for Venus, Jupiter, and Saturn. The discrepancies for the latter two giant planets have been attributed⁷ to a substantial 3-D effect associated with the flattening of the planetary magnetopause cross sections in the polar regions, presumably as a result of the high spin rate and large size of these planets; whereas the obstacle cross section was always assumed to be circular in the computational model. To enable the appropriate comparison with the gasdynamic convected field model to be made, Stahara et al.⁸ extended the basic computational model to apply to an arbitrary 3-D magnetospheric obstacle, and have demonstrated that the results from the 3-D model are in good accord with the observations for Jupiter and Saturn.

For Venus, observations indicate that the planet has no significant magnetic field and that a virtually axisymmetric obstacle shape results from solar wind flow past the planetary ionosphere, much as conceived in the original theoretical model^{4,5,9}. Numerous comparisons of the calculated results with those actually observed at Venus^{7,10,11,12} indicate, however, that the observed bow

* President, Associate Fellow AIAA

† Research Scientist, Member AIAA

‡ Professor, Fellow AIAA

wave tends on the average to flare out somewhat more on the flanks than predicted by the model. This has been generally interpreted to be the result of effects of solar wind pickup of newly ionized atmospheric particles not included in the model (see Breus¹³ for a recent review). Breus¹³ and Belotserkovskii et al.¹⁴ have recently published results of a calculation to illustrate the magnitude of these effects, but their results differ substantially from those provided by our model for the same conditions. While their results match the observations reasonably well, we believe their computed results are lacking in accuracy and greatly overestimate the effects of ion pickup.

Similar, but much more extensive, ion pickup processes become of dominant importance for comets, and, as emphasized by Breus et al.¹⁵, much is to be learned by studies of their similarities and differences. Study of the nature of comets extends from antiquity to the present day (see Ref. 16 for a comprehensive account), and has provided many insights into the properties of both comets and the interplanetary environment. Indeed, the first suggestion for the continual existence of a high speed outflow of gas from the sun, the solar wind, was made by Biermann^{17,18} on the basis of his studies of comet tails. Among the first systematic studies of solar wind flow past a comet in the modern context is that of Ref. 19 in which the solar wind flow was represented by the conservation equations of gasdynamics with additional source terms included to represent effects of mass, momentum, and energy addition in the flow. These are essentially the same equations employed in the model developed here, although the expressions for the source terms are quite different. However, the present numerical solutions are of significantly higher accuracy, due largely to advances in both numerical methods and computational capability made during the intervening twenty years.

Schmidt and Wegmann²⁰ subsequently rephrased the analysis in terms of the equations of magnetohydrodynamics, much as has been done for the planetary applications¹ and presented an interesting but limited set of low resolution results. Because the computational cost of determining solutions of the magnetohydrodynamic equations is considerably greater than it is for the gasdynamic equations, and because the latter have a long history of providing results of useful accuracy for related applications, we have based our model on the gasdynamic equations but have employed superior methods for their solution. In this way, our model provides high resolution results with almost minimal computing costs using a modern supercomputer. Although it is highly unlikely that the flow about an actual comet is either steady or possesses any simple symmetry, the present initial cometary application is based on the assumption that the flow is steady and axisymmetric under the hopeful assumption that such results will be generally informative about the basic nature of cometary flow fields. The benefits are at least a hundredfold reduction in the amount of computing required for a solution, and the avoidance of a requirement to specify with realism the unsteady and nonspherical symmetry properties of the outflow of neu-

tral gas from the cometary nucleus, which are in general unknown.

In this paper, the new computational model is described and results are presented for the shape of the bow wave and the associated properties for solar wind flow past both planetary and cometary bodies exuding neutral particles which subsequently become ionized. A quantitative determination of the effects of such ion addition to the solar wind is provided by presenting the results of a parametric study in which the amount of ion addition is varied. The new results provide considerable improvement over previous qualitative and semi-quantitative determinations of the properties of solar wind flow past a comet. For Venus they also show that a much greater addition of new ions than assumed by Breus et al.¹³ and Belotserkovskii et al.¹⁴ is required to achieve good quantitative agreement with observations.

Mathematical Model and Solution Procedure

The fundamental assumption underlying the present work, as in the previous analyses in the references cited above, is that the average bulk properties of the solar wind flow around a planetary magnetosphere can be described adequately by solutions of the continuum equations of magnetogasdynamics for a perfect dissipationless plasma having infinite electrical conductivity and zero viscosity and thermal conductivity. The primary justification for this assumption is provided not by rigorous proof but by the outstanding general agreement of the results predicted on this basis compared with a large number of direct observations in space. These governing equations, which have been given previously (see Ref. 12 for our most recent account), will not be repeated here. For application to flows with significant pickup of newly created ions, the conservation equations used to describe the solar wind flow must be augmented to include terms to represent the effective mass, momentum, and energy additions to the flow.

For typical solar wind conditions, both the oncoming sonic Mach number $M_{S\infty} = v_{\infty}/\sqrt{\gamma p/\rho}$ and Alfvén Mach number $M_{A\infty} = v_{\infty}/\sqrt{B_{\infty}^2/(4\pi\rho_{\infty})}$ are substantially greater than unity. Under these conditions, an important simplification of the magnetohydrodynamic equations may be introduced because of the relative smallness of the magnetic terms in the momentum and energy conservation equations. With these terms omitted, the magnetogasdynamic equations separate into two sets: the gasdynamics equations for the flow of a perfect gas with mass, momentum, and energy addition, and the Faraday magnetism equations. The equations for the fluid motion about an obstacle of given shape thereby reduce to those of gasdynamics, and can be solved without further consideration of the magnetic field. The magnetic field can then be determined subsequently by solving the remaining Faraday equations using the values for the velocity and density fields already calculated. The magnetic field determined in this fashion is usually interpreted, somewhat ambiguously, as being 'frozen-in' or 'moving with the fluid'. The resulting equations and the model they represent are referred to as the gasdynamic-convected

field approximation. It should be noted, however, that the interpretation of the field as frozen-in or moving with the fluid is not dependent upon the separation of the fluid motion determination from the magnetic field determination, but is an exact consequence of the basic assumption that the flow can be represented by the magnetohydrodynamic equations for a perfect dissipationless electrically conducting gas.

In carrying out the decoupled gasdynamic calculation, the shape of the magnetoionopause is not known a priori, but must be found as part of the overall solution. In our previous analyses, the magnetoionopause shape has been determined by either an independent approximate theoretical analysis, a synthesis of actual observational results, or a combination thereof. This latter procedure has also been employed in the present analysis.

Computational models based on the full magnetohydrodynamic equation set now exist, but are still in a preliminary state of development and lack adequate resolution for many purposes. Hence, Russell³ has recently stated, "Currently, the only way to achieve the spatial resolution needed for a useful comparison with data obtained on a pass through a planetary magnetosheath is to employ the gasdynamic-convected field model".

To be more precise, the conservation equations for unsteady axisymmetric gasdynamic flow with mass, momentum, and energy addition may be written as follows:

$$\frac{\partial Q}{\partial t} + \frac{\partial E}{\partial z} + \frac{\partial F}{\partial R} = S + H \quad (1)$$

in which

$$Q = \begin{pmatrix} \rho \\ \rho u \\ \rho v \\ e \end{pmatrix}, \quad E = \begin{pmatrix} \rho u \\ \rho u^2 + p \\ \rho uv \\ (e + p)u \end{pmatrix}$$

$$F = \begin{pmatrix} \rho v \\ \rho uv \\ \rho v^2 + p \\ (e + p)v \end{pmatrix}, \quad H = \frac{1}{R} \begin{pmatrix} \rho v \\ \rho uv \\ \rho v^2 \\ (e + p)v \end{pmatrix} \quad (2)$$

$$S = \begin{pmatrix} S_{\text{mass}} \\ S_{\text{x-momentum}} \\ S_{\text{R-momentum}} \\ S_{\text{energy}} \end{pmatrix}$$

where Q is the conserved quantity, E , F , and H are the corresponding fluxes, and S represents the source terms as indicated. The other quantities have their usual meanings, i.e., ρ is the density, u and v are the velocity components parallel to the cylindrical s and R axes, p is the pressure, and e is the total energy, which is related to the other quantities by $p = (\gamma - 1)(e - \rho(u^2 + v^2)/2)$ where γ is the ratio of specific heats.

The remaining Faraday equations for the magnetic field

\vec{B} are:

$$\frac{\partial \vec{B}}{\partial t} = \text{curl}(\vec{V} \times \vec{B}), \quad \text{div} \vec{B} = 0 \quad (3)$$

where \vec{V} and \vec{B} are the velocity and magnetic field vectors respectively.

In our realization of the solution, the discretized gasdynamic equations are solved on a segmented inner/outer curvilinear grid system in order to accurately account for mass loading effects upstream of the bow shock. As illustrated in Figure 1, the inner grid segment extends from the obstacle surface to the fitted bow shock, while the outer segment starts at the bow shock and extends to a location sufficiently far upstream where the mass, momentum, and energy additions due to the source terms are no longer significant. As is evident from the grid displayed in Figure 1, we employ a fitted discontinuity procedure to represent both the bow shock and the obstacle surface. Although this is far more difficult to implement than simply allowing the solution algorithm to capture these discontinuities, employing a fitted discontinuity representation allows the exact satisfaction of the shock jump and obstacle surface boundary conditions at surfaces that are precisely defined, in contrast to the smeared representation that inevitably results from even the best capturing methods.

One of the most important features of both the present and all of our previous models is the use of two separate, but coupled, computational procedures for determining the steady flow field. As illustrated in Figures 1 and 2, the model is composed of a nose region solver that determines the flow field from the subsolar region to or somewhat beyond the terminator location by using an unsteady procedure that marches the solution forward in time to obtain the asymptotic steady state solution. That solver is then joined with a spatial-marching tail region solver that advances the flow field solution downstream to any arbitrary distance in which the flow remains supersonic.

The precise axial location at which the two solutions are joined is relatively arbitrary, the single constraint being that at all points on the joining plane the axial component of the local sonic Mach number be supersonic. This is the basic requirement of the spatial-marching solver in order that it be able to march the solution downstream. In most of our previous applications, it has been convenient to select for the joining location the plane through the planetary center oriented normal to the oncoming solar wind direction, i.e., the terminator plane. In some cases involving obstacles that possess considerable flare at the terminator, it is necessary to relocate the joining plane at some fraction of an obstacle nose radii downstream of the terminator in order to satisfy the requirement of supersonic axial Mach number.

The primary reasons for expending the substantial additional development effort to realize such a coupled two flow solver combination, rather than employ a sin-

gle time-marching solver for the entire flow field as is done in all existing magnetohydrodynamic solutions procedures, are twofold. First, there is the substantial gain in computational efficiency since the computationally expensive time-marching procedure required to treat the subsonic/transonic flow in the nose region is used only where needed, while the remainder of the solution is obtained using a highly efficient spatially marching procedure appropriate for supersonic flow. Secondly, the computational capability is attained to determine flow conditions as far downstream as desired. Such a capability cannot be provided by a time-marching procedure. Finally, we note that such a subdivision of both flow field and solution procedures is not uncommon in calculating supersonic/hypersonic flows and has been used extensively not only in all our previous work, but also for example, in the analysis of reentry flows including space shuttle applications.

Nose Region Solution Procedure

In the nose region, we have employed the procedure of Beam and Warming²⁰ to solve equations (1) and (2) with specified mass, momentum, and energy addition. First, the governing equations are transformed from the (x, R, t) coordinates to the generalized set of coordinates, (ξ, η, τ) . This new set of equations can be written as:

$$\frac{\partial \hat{Q}}{\partial \tau} + \frac{\partial \hat{E}}{\partial \xi} + \frac{\partial \hat{F}}{\partial \eta} = \hat{S} + \hat{H} \quad (4)$$

The vectors \hat{Q} , \hat{E} , and \hat{F} represent the transformed dependent variables, and their flux vectors as:

$$\hat{Q} = \frac{1}{J} Q, \quad \hat{E} = \frac{1}{J} (\xi_x E + \xi_R F), \quad \hat{F} = \frac{1}{J} (\eta_x E + \eta_R F) \quad (5)$$

The transformed source terms are simply written as:

$$\hat{H} = \frac{1}{J} H, \quad \hat{S} = \frac{1}{J} S \quad (6)$$

In the above equations, $(\xi_x, \xi_R, \eta_x, \eta_R)$ are the transformation metrics and J is the Jacobian of the transformation. Even though the grid points are free to move in time, the unsteady metric terms corresponding to this grid movement have been neglected for the interior nodal points since only a steady state solution is desired. This is easily justified since the grid speeds vanish as the steady state solution evolves.

The numerical algorithm used to solve the above equations is based on the Beam and Warming²¹ procedure with the boundary conditions of Chakravarthy²². The method is a fully implicit, noniterative, scheme that is second-order accurate scheme in space. It can be written in delta form $(\Delta \hat{Q} = \hat{Q}^{n+1} - \hat{Q}^n)$ as:

$$\left[I + \Delta t \delta_\xi \hat{A} + \Delta t \delta_\eta \hat{B} \right]^n \Delta \hat{Q} = -\Delta t (\delta_\xi \hat{E} + \delta_\eta \hat{F} - \hat{H} - \hat{S})^n + D^s(\hat{Q}) \quad (7)$$

Here, \hat{A} , and \hat{B} are the standard fluid dynamic Jacobians, $\hat{A} = \partial \hat{E} / \partial \hat{Q}$ and $\hat{B} = \partial \hat{F} / \partial \hat{Q}$ and I is the identity

matrix. The superscript n implies evaluation at the n th time level. Second-order, central-differences have been used for all discretized derivatives and a fourth order artificial dissipation term, D , has been added for stability. The integration step size, Δt , is generally specified in the beginning of the calculation and held constant for the entire computation.

As noted above, the computations are carried out on a mesh that conforms to the fixed assumed shape of the obstacle and adapts itself at each time step of the solution to conform to the time-varying shape of the bow wave. The associated cylindrical (x, R) coordinate axes and a typical grid employed in our analysis are illustrated in Figure 2. The origin coincides with the center of the planet or the cometary nucleus, the x -axis, which coincides with the longitudinal axis of symmetry of the magnetosphere, points directly into the oncoming solar wind, and the R axis extends from the origin perpendicular to the x axis. The obstacle to shock grid lines and their continuations extend in the radial r direction from the origin. The azimuthal grid lines extend from the x axis to the R axis at the terminator plane in such a way that one of the grid lines conforms to the obstacle surface and another conforms to the bow wave. Various numbers of grid lines may be used for the calculations, but the situation portrayed in Figure 2 in which a finer mesh is employed between the obstacle and the bow wave than in the region beyond the bow wave may be taken as representative. In this example, there are 35 azimuthal grid lines and 23 radial grid lines for the nose region. Values for all flow quantities are calculated at every point of intersection of these grid lines.

The boundary conditions applied to the set of governing equations are outlined in Figure 3. At the outermost boundary, the flow is uniform and parallel to the x -direction with free-stream values for the density, velocity, and Mach number corresponding to those of the undisturbed solar wind. At the innermost boundary, the flow is tangential to the obstacle surface. In addition, the solution must satisfy the unsteady Rankine-Hugoniot shock relations at the moving bow shock surface, be entirely supersonic at the downstream outflow boundary of the nose region, and be symmetric about the stagnation streamline upstream from the nose. Initial flow field conditions are determined by use of an approximating surface for the bow shock wave, and by prescribing a modified Newtonian pressure distribution on the surface of the magnetopause. Since the maximum entropy streamline wets the obstacle, that fact plus the flow tangency condition on the magnetopause serve to determine the remainder of the flow properties on that surface. A linear variation for the flow properties between the bow shock and the magnetopause then provides the starting flow field which is then integrated in a time-asymptotic fashion until the steady state solution is obtained.

At the boundaries, modification of the differencing algorithm to account for the particular conditions described above is accomplished as follows. First, an eigenvalue analysis reveals the number of boundary conditions need-

ing to be specified at each boundary. The number of boundary conditions at each boundary must be equal to the number of characteristic waves entering the computational domain through that boundary. For the supersonic outflow condition, since all eigenvalues are associated with waves exiting the computational domain at that boundary, no additional boundary conditions need be specified and the governing equations are discretized using a one sided difference into the computational domain from this boundary. These equations are then made implicit by a simple linearization process.

Boundary conditions other than those associated with supersonic flow are not as straightforward. A characteristic equation is specified for each outward traveling wave and boundary conditions are specified until the number of equations matches the number of dependent variables. These characteristic equations are a direct result of the eigenvalue analysis and a further discussion of their origin can be found in reference 22. For the surface tangency boundary condition, three characteristic equations and one boundary condition are used since only one eigenvalue is associated with an inward traveling wave. The boundary condition used in this case is the specification a zero surface-normal velocity.

For the bow shock boundary condition, two additional quantities are added to the set of dependent variables. They are x_r and y_r , the shock propagation velocities speeds in the x and y direction respectively. An eigenvalue analysis reveals that only one wave propagates from the interior flow field to the bow shock resulting in only one valid characteristic equation. Five boundary conditions must then be specified. They consist of four Rankine-Hugoniot relations across the bow shock and one grid point restriction equation. The Rankine-Hugoniot relations are well known and the grid point restriction equation restricts the shock grid points to lie only on rays emanating from the obstacle center.

Tail Region Solution Procedure

If the velocity of the flow in the streamwise coordinate direction is greater than the speed of sound, a method can be employed that solves for the flowfield directly without a costly time iteration. The method is based on that of Shiff and Steger²³ and marches along the streamwise coordinate rather than time to obtain a solution. Since the flow in the tail region fulfills this criteria, such a method is used. The governing equations used here are identical to those of equations 4, with the exclusion of any time derivatives.

$$\frac{\partial \hat{E}}{\partial \xi} + \frac{\partial \hat{F}}{\partial \eta} = \hat{S} + \hat{H} \quad (8)$$

If a first order approximation to the streamwise derivative is made and a spatial linearization of all quantities evaluated at the new spatial location is done, the numerical scheme can be written in delta form ($\Delta \hat{Q} = \hat{Q}_{i+1} - \hat{Q}_i$) as:

$$[\hat{A}_i + \Delta \xi \delta_q \hat{B}'_i] \Delta \hat{Q} = -\Delta \xi (\hat{E}'_i - \hat{E}_i + \delta_q \hat{F}'_i - \hat{H}'_i - \hat{S}) + \hat{A}_i [D^4(Q)] \quad (9)$$

The subscript i denotes the axial plane, and the primed quantities signify that the metric quantities have been frozen in the linearization. Again the δ -operator implies central differencing and a fourth order artificial dissipation has been used. This tail region solver has been built in such a way to be as consistent as possible with the nose region solver. Even boundary conditions are similar with the exception of spatial rather than temporal linearization.

Applications to Comets

To complete the specification of the mathematical problem to represent solar wind flow past a comet, it is necessary to supply expressions for the mass, momentum, and energy source terms. For the applications reported here, we have employed the model suggested by Schmidt and Wegmann²⁰ and others in which

$$S = \begin{pmatrix} S_{\text{mass}} \\ S_{\text{x-momentum}} \\ S_{\text{R-momentum}} \\ S_{\text{energy}} \end{pmatrix} = \begin{pmatrix} S_m \\ S_m W_x \\ S_m W_R \\ \frac{S_m W^2}{2} \end{pmatrix} \quad (10)$$

where

$$S_m = \frac{G \sigma m_c}{4\pi W r^2} \exp\left(-\frac{\sigma r}{W}\right) \quad (11)$$

and where G is the total number of neutral particles emitted from the comet per second, σ is the photoionization rate, W is the radial expansion velocity of the neutral particles, r is the three-dimensional radial distance from the origin, and m_c is the neutral particle mass. The physical considerations underlying the above formulation for the source terms are that the ions are formed at a constant rate σ by photoionization of the originally neutral cometary particles which have been evaporated from the nucleus. These neutral molecules are all considered to have the same mass m_c and to move radially away from the comet with a constant speed W . The electrons are treated as a cool component whose effects on the properties of the flow are negligible.

With regard to the computational considerations that these source terms have on the numerical method, we note that with G , σ , M_C , and W considered to be constants, a typical conservation equation for, say, the continuity of mass then becomes of the form

$$\text{L.H.S. continuity equation} = \tilde{S}_m \cdot f(r) \quad (12)$$

where $\tilde{S}_m = \text{Constant}$ and $f(r) = O(1)$. We note that representative values for the normalized constant \tilde{S}_m for cometary interactions range from as small as 0.1 to as large as 1000 and even greater. The larger values result in an extremely stiff set of partial differential equations and

poses a severe and challenging test of any computational procedure.

We have applied the above computational model to a parametric series of mass loadings for the above cometary source model with good success. Figure 4 displays results for the density contours for a complete nose and tail flow field for one such calculation employing cometary source parameters representative of those suggested by Schmidt and Wegmann²⁰. That result corresponds to a cometary mass loading with $G = 6 \times 10^{28}$ particles per second, a photoionization rate σ of 10^{-6} per second, a radial expansion velocity of 1 km/sec, a cometary particle mass of $23.3m_p$, where m_p represents the proton mass, a solar wind density $\rho_{\infty} = 5m_p/cm^3$ and velocity $v_{\infty} = 350$ km/sec, sonic Mach number $M_{S_{\infty}} = 6.0$, and ratio of specific heats $\gamma = 5/3$. The assumed cometary tangential discontinuity surface was approximated as a hemisphere/cylinder. For perspective on this choice for G , recent observations provide a value of about 4×10^{28} particles/sec for Giacobinin-Zinner, a middle-size comet²⁴ and about 1×10^{30} particles/sec for Halley, a large comet. The results for density contour lines upstream of the bow, indicating that considerable compression of the flow occurs upstream of the bow wave. Overall, however, the results are quite similar to previously published results for planetary flows with no ion pickup.

Figure 5 shows corresponding results for the nose region for four different values for G ranging from 1.4×10^{28} to a substantially larger value of 1.12×10^{29} . Also shown on those figures are the corresponding values of the normalized mass source constant \tilde{S}_m which range from 1.2 to 9.2. The plot for the smallest G indicates only one density contour line upstream of the bow wave, and a comparison reveals that the results in their entirety differ only slightly from those without ion pickup about a similar obstacle. The plots for larger G show increased compression upstream of the bow wave. They also show that the entire bow wave moves away from the cometary obstacle, greatly enlarging the region between the obstacle and the bow wave. More specifically, the nose of the bow wave is shown to move from about $1.3 R_0$ upstream of the obstacle nose for small G to more than $2.0 R_0$ for the largest G , where R_0 is the cometary obstacle nose radius. These trends will continue as still larger values for mass loading are considered, or similarly if smaller obstacle sizes are assumed. The latter possibility highlights a significant remaining need for a model for the flow interior to the obstacle boundary to locate as part of the solution the cometary tangential discontinuity surface that separates the flow of cometary material from the external flow of the solar wind and picked-up ions.

The contour lines downstream of the bow wave also change dramatically in appearance from that characteristic of planetary flows with no ion pickup at the smallest G for which results are presented to being nearly concentric semi-circles (or hemispheres) about the obstacle nose at the largest G . These results also show an increasingly thick dark band of contour lines immediately adjacent

to the obstacle indicating an enormous enhancement of the density in that region. For the highest mass loading determined thus far in this study, corresponding to $\tilde{S}_m = 9.2$, our results indicate densities greater than 40 times that in the incident solar wind at the largest value for G . It is evident there exists a strong tendency for the newly ionized particles to be swept back toward the obstacle surface where they form a dense boundary layer.

Application to Venus

Application of the model to simulate the solar wind interaction with Venus requires the appropriate source model. For this, we follow the suggestion of Nagy et al.²⁵, Breus²³, and Belotserkovskii et al.¹⁴ and assume that (a) the only important source of new ions is the photoionization of the hot oxygen corona, (b) any initial motion of the newly-created ions is small enough that there is no significant addition of momentum or energy to the flow, and (c) that the ion source term can be represented by an expression of the form

$$S_m = Const \cdot \exp \frac{-(r - R_0)}{H_{O+}} \quad (13)$$

in which R_0 is the distance from the origin at the planetary center to the nose of the ionopause obstacle, and $Const$ is proportional to the product of the number density n_{O+} of the neutral hot oxygen particles at the ionopause nose and their mass m_{O+} , divided by the characteristic time τ for photoionization. Although the mass loading beyond the bow wave may be small, depending on the values selected for H_{O+} and $Const$ in Equation (13), in the results reported here, we have not terminated the mass addition at the location of the bow wave as was done in Refs. 13 and 14, but allowed its influence to continue all the way to the outer boundary of the grid. In this way, our solution, including in particular the location and local strength of the bow wave, is influenced by essentially all of the mass addition beyond the ionopause and not just that downstream of the bow wave.

Figure 6 presents a comparison of model results for constant density contours in the Venusian ionosheath with and without mass loading determined as described above. The calculations were carried out for flow conditions corresponding to those of orbit 582 of the Pioneer Venus Orbiter as suggested in previous studies by Mihalov et al.¹⁰, Breus²³, and Belotserkovskii et al.¹⁴. They are that the oncoming flow has a free stream Mach number of 5.7 and a value of 5/3 for the ratio of specific heats γ , and the Venusian ionospheric obstacle has a shape defined by a value of 0.03 for the ratio h_0/R_0 of the scale height in the outer ionosphere to the obstacle nose distance from the planetary center in accordance with the procedures^{4,6,9} for gasdynamic modeling of the flow past Venus, and that $Const$ and H_{O+}/R_0 in equation (16) are equal to 4.49 and 0.062 respectively, corresponding to a value for n_{O+} of 3×10^6 particles/cm³, $H_{O+} = 400$ km and $R_0 = 6450$ km.

Figure 6 shows a small but notable difference in the density contours between the results with and without

hot oxygen mass loading as predicted by the model. The location of the bow wave, however, is virtually the same for the two cases. We note that the single contour line upstream of the bow wave indicates some compression of the oncoming solar wind to occur in the mass loaded case. The significantly sharp bending and compaction of the density contour lines near the ionopause indicates the presence of a thin boundary layer of enhanced density adjacent to the ionopause.

Figure 7 provides a comparison of the results from the current model and that of Refs. 13 and 14 for the non-mass loaded and mass loaded cases for Venus, and shows that the results differ substantiantially for the same conditions. Breus¹³ and Belotserkovski et al.¹⁴ find the mass loading to have a significant effect on the location of the bow wave, moving it to a position slightly beyond that reported by Mihalov et al.¹⁰, whereas our results indicate almost no effect. Their results also indicate the bow wave for the nonloaded case to be slightly further from the ionopause than indicated by our calculations, with that provided in the more recent publication of Belotserkovski et al.¹⁴, presumably corrected from those reported by Breus¹³, being in better agreement with our results. The shock location for the mass loaded case as reported in both Refs. 13 and 14 is the same. Although that result is in better agreement with the observations of Mihalov et al.¹⁰, we have carefully reviewed our analysis and believe that the results predicted by the present model are correct for the suggested mass source model and mass loading parameters suggested for this example.

To determine what amount of mass loading would be required with our model for the predicted terminator location of the bow wave to match that observed, we have carried out a parametric parameter study involving an enhancement of the mass source constant ($Const$) and the hot oxygen scale height (H_{o+}) as given in the source model in Equation (16). Figure 8 shows the results for 8 different combinations of the two parameters. In the plot on the left, the four results shown for the bow shock correspond to the same value for $Const$ as used for Figure 7, namely 4.49 corresponding to a number density of 3×10^4 for the neutrals at the ionopause nose, but a range of values from 400km to 3200km for the scale height H_{o+} of the hot oxygen. The results for the largest of these values places the bow wave in a position that agrees almost perfectly with the observations of Mihalov et al. (Ref. 10), but the value of 3200km seems unreasonably high for the scale height of the hot oxygen.

The results in the plot in the right half of Figure 8 show the corresponding results for four other combinations of the two mass loading parameters ($Const$, H_{o+}). They show that the bow wave moves significantly outward from the planet as either parameter is increased. Compared with these four bow wave locations, the data of Mihalov et al.¹⁰ for Pioneer Venus Orbiter for orbit 582 falls between the two outermost locations corresponding to $n_{o+} = 3 \times 10^5$, and $H_{o+} = 800$ and 1600km. It appears that²⁰ values for n_{o+} of this order may be appropriate for Venus, but that values much larger than about 400km for

the scale height H_{o+} of the hot oxygen are probably not appropriate. A substantial part of the outward displacement of the bow wave from that indicated for flows without mass loading thus appears to be accounted for, but some additional considerations are necessary to achieve a good quantitative agreement with this particular data set. Whether the main source of these differences arises from shortcomings in the model itself or in the interpretation of data required as input to the model remains uncertain, and is currently under study.

All of the numerical calculations for which results are reported here were performed on the NASA Ames Research Center CRAY XMP computer facility. Approximately 10 minutes of CPU time were typically required for the calculations for a single case of the more difficult cometary examples considered in this study, and approximately 2 minutes for the typical Venusian mass loaded cases. Nearly all of this time is spent with the nose region solver, as the tail region solver is extremely rapid and can carry the solution downstream 10 obstacle nose radii in typically less than 30 CPU seconds.

Conclusions

The development and initial verification of a computational model for determining the solution of the gasdynamic portion of the gasdynamic convected magnetic field model for solar wind flow past axisymmetric obstacles surrounded by an extended atmosphere of neutral particles undergoing ionization so as to add mass, momentum, and energy to the flow is described. Results from the new model converge continuously to those calculated previously for magnetoionospheres without ion pickup using completely different computational procedures, thereby verifying the accuracy of both methods.

Specific applications are made to cometary interactions and to Venus using ion loading rates provided by existing analyses of direct observations. For comets, the high mass loading causes the bow wave to be weakened due to the slowing of the upstream solar wind and to move to substantially greater distances from the nucleus. For Venus, the ion addition is comparatively much smaller, and the resulting effects more modest, although still significant for quantitative comparisons between theory and observations. In both applications, large density enhancements are indicated by the model immediately adjacent to the obstacle surface, with values for the density as great as 40 times that in the incident solar wind in some of the cometary examples. Even larger enhancements are anticipated when the model is applied to larger comets, such as Halley, with more massive ion additions than those we have considered thus far.

Acknowledgements

This research was jointly supported by NASA Headquarters under Contract NASW-4135 and Grant NAGW 278, and by Air Force Office of Scientific Research Contract F49620-86-C-0035. Cray XMP computational time was provided by the Applied Computational Fluids

References

1. Spreiter, J. R., A. L. Summers, and A. Y. Alksne, *Hydromagnetic flow around the magnetosphere*, Planet. Space Sci., 14, 223-253, 1966.
2. Spreiter, J. R., and S. S. Stahara, *Magnetohydrodynamic and gasdynamic theories for planetary bow waves*, in *Collisionless Shocks in the Heliosphere*, Review of Current Research. edited by B. T. Tsurutani and R. G. Stone, pp.85-107, AGU Geophysical Monograph 35, 1985.
3. Russell, C. T., *Planetary bow shocks*, in *Collisionless Shocks in the Heliosphere*, Review of Current Research. edited by B. T. Tsurutani and R. G. Stone, pp.107-130, AGU Geophysical Monograph 35, 1985.
4. Spreiter, J. R., and S. S. Stahara, *A new predictive model for determining solar wind-terrestrial planet interactions*, J. Geophys. Res., 85, 6769-6777, 1980.
5. Spreiter, J. R., and S. S. Stahara, *Solar wind flow past Venus: Theory and comparisons*, J. Geophys. Res., 85, 7715-7738, 1980.
6. Stahara, S. S., D. Klenke, B. C. Trudinger, and J. R. Spreiter *Application of advanced computational procedures for modeling solar-wind interactions with Venus - Theory and computer code*, NASA Contr. Rep., CR 3267, 1980.
7. Slavin, J. A., Smith E. J., Spreiter, J. R., and; Stahara, S. S. *Solar wind flow about the outer planets: gas dynamic modeling of the Jupiter and Saturn bow shocks*, J. Geophys. Res., 90, 6275-6286, 1985.
8. Stahara, S. S., Rachiele, R. R., and Spreiter, J. R., *A 3-D Computational Model for Solar Wind/ Magnetosphere Interactions: Prediction of Polar Flattening of Jupiter and Saturn Magnetospheres*, AIAA Paper 87-1411. July 1987
9. Spreiter, J. R., A. L. Summers, and A. W. Rizzi, *Solar Wind Flow Past Non-magnetic Planets - Venus and Mars*, Plan. and Space Sci., 18 1281-1299,1970.
10. Mihalov, J. D., J. R. Spreiter, and S. S. Stahara, *Comparison of gas dynamic model with steady solar wind flow around Venus*, J. Geophys. Res., 87, 10363-10371, 1982.
11. Slavin, J. A., and R. E. Holzer, J. R. Spreiter, S. S.; Stahara, and D. S. Chaussee *Solar wind flow about the terrestrial planets 2. Comparison with gas dynamic theory and implications for solar-planetary interactions*, J. Geophys. Res., 88, 19-35, 1983.
12. Luhmann, J. G., C. T. Russell, J. R. Spreiter, and; S. S. Stahara *Evidence for mass-loading of the Venus magnetosheath*, Adv. Space Res., 5, 307-311, 1985.
13. Breus, T. K., *Mass-loading at Venus: Theoretical Expectations*, Adv. Space Res., 6, 167-177,1986.
14. Belotserkovskii, O. M., T. K. Breus, A. M. Krymskii, V. Ya Mitnitskii, A. F. Nagy, and T. I. Gombosi *The effect of the hot oxygen corona on the interaction of the solar wind Venus*, Geophys. Res. Letters. 14 , 503-506, 1987.
15. Breus, T. K., A. M. Krymskii, and J. G. Luhmann, *Solar wind mass-loading at comet Halley: A lesson from Venus?*, Geophys. Res. Letters. 14, 499-502, 1987.
16. Brandt, J. C., and R. D. Chapman, *Introduction to Comets*. Cambridge University Press, Cambridge, U. K., 1981.
17. Biermann, L., *Kometenschweife und solare Korpuskularstrahlung*, Z. Astrophys., 29, 274-286, 1951.
18. Biermann, L., *Physical processes in comet tails and their relation to solar activity*, Extrait des Mem. Soc. Roy. Sci. Liege Collection in -4 °. 13, 291-302, 1953.
19. Biermann, L., B. Brosowski, and H. U. Schmidt, *The interaction of the solar wind with a comet*, Solar Physics. 1, 254-284, 1967.
20. Schmidt, H. U., and R. Wegmann, *Plasma flow and magnetic fields in comets*, Proc. International Meeting on the Giotto Mission. Noordwijkerhout, Netherlands. (also ESA SP-169), 1981.
21. Beam, R. M., and R. F. Warming, *An implicit factored scheme for the compressible Navier-Stokes equations*, AIAA Paper 77-645. Albuquerque, New Mexico, 1977.
22. Chakravarthy, S.R., *Euler equations-implicit schemes and implicit boundary conditions*, AIAA Paper 82-0228. Jan. 1982.
23. Schiff, L. B. and J. L. Steger, *Numerical simulation of steady supersonic flows*, NASA TP 1749. May 1981.
24. Mendis, D. A., E. J. Smith, B. T. Tsurutani, J.; A. Slavin, D. E. Jones, and G. L. Siscoe *Comet-solar wind interaction: dynamic length scales and models*, Geophys. Res. Letters. 13, 327-333, 1986.
25. Nagy, A. F., T. E. Cravens, J. H. Yee, and A. I.; P. Stewart *Hot oxygen atoms in the upper atmosphere of Venus*, Geophys. Res. Letters. 8, 629- 633, 1981.
26. Luhman, J. L., *Private Communication*. May 1987

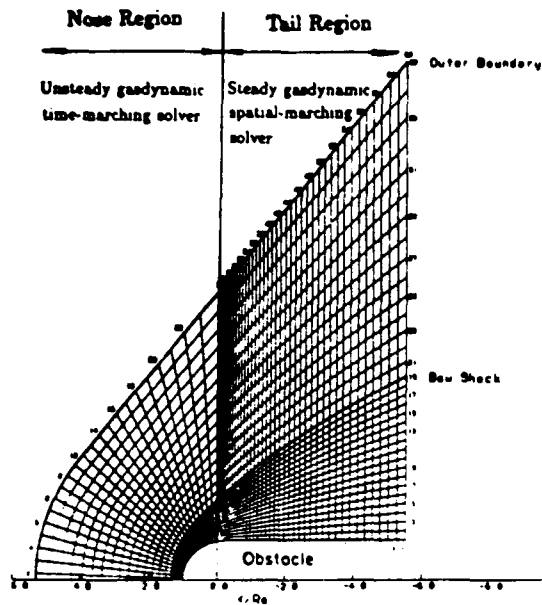


Figure 1. Illustration of flow field subdivision, extended grid, and coupled flow solver combination employed in the mass loaded solar wind planetary/cometary interaction model.

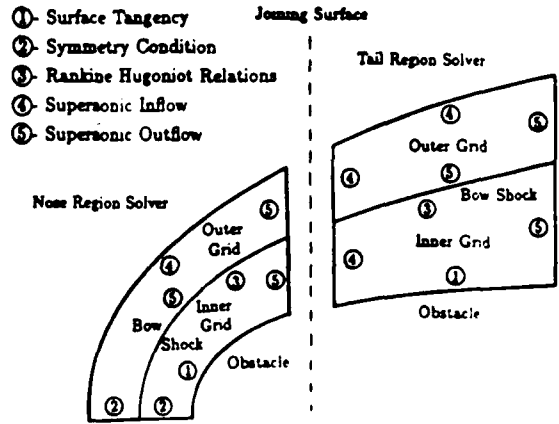


Figure 2. Illustration of boundaries and coupling of computational domains in the mass loaded solar wind planetary/cometary interaction model.

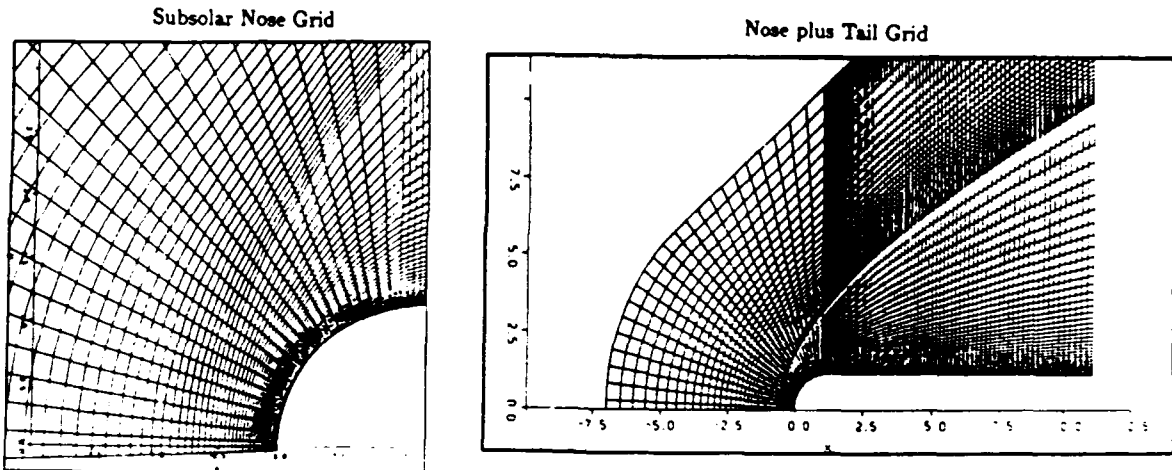


Figure 3. Illustration of a typical computational grid employed in the mass loaded solar wind planetary/cometary interaction model.

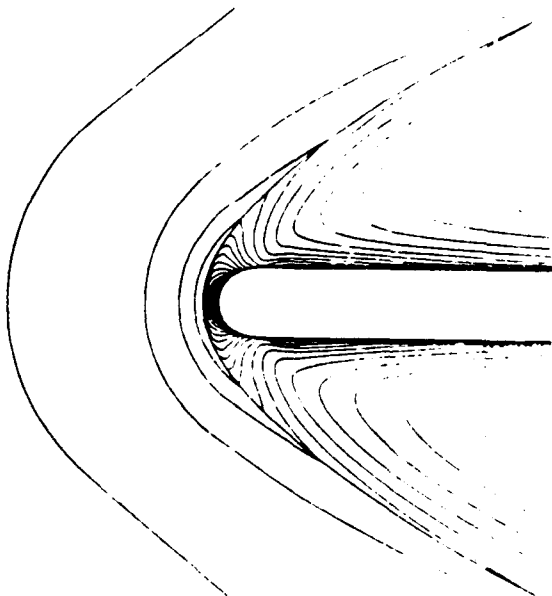


Figure 4. Density contours for a simulated cometary flow with extended mass loading of $G = 6 \times 10^{28}$ particles/sec emitted by the comet, $M_{S\infty} = 6.0$, $\gamma = 5/3$.

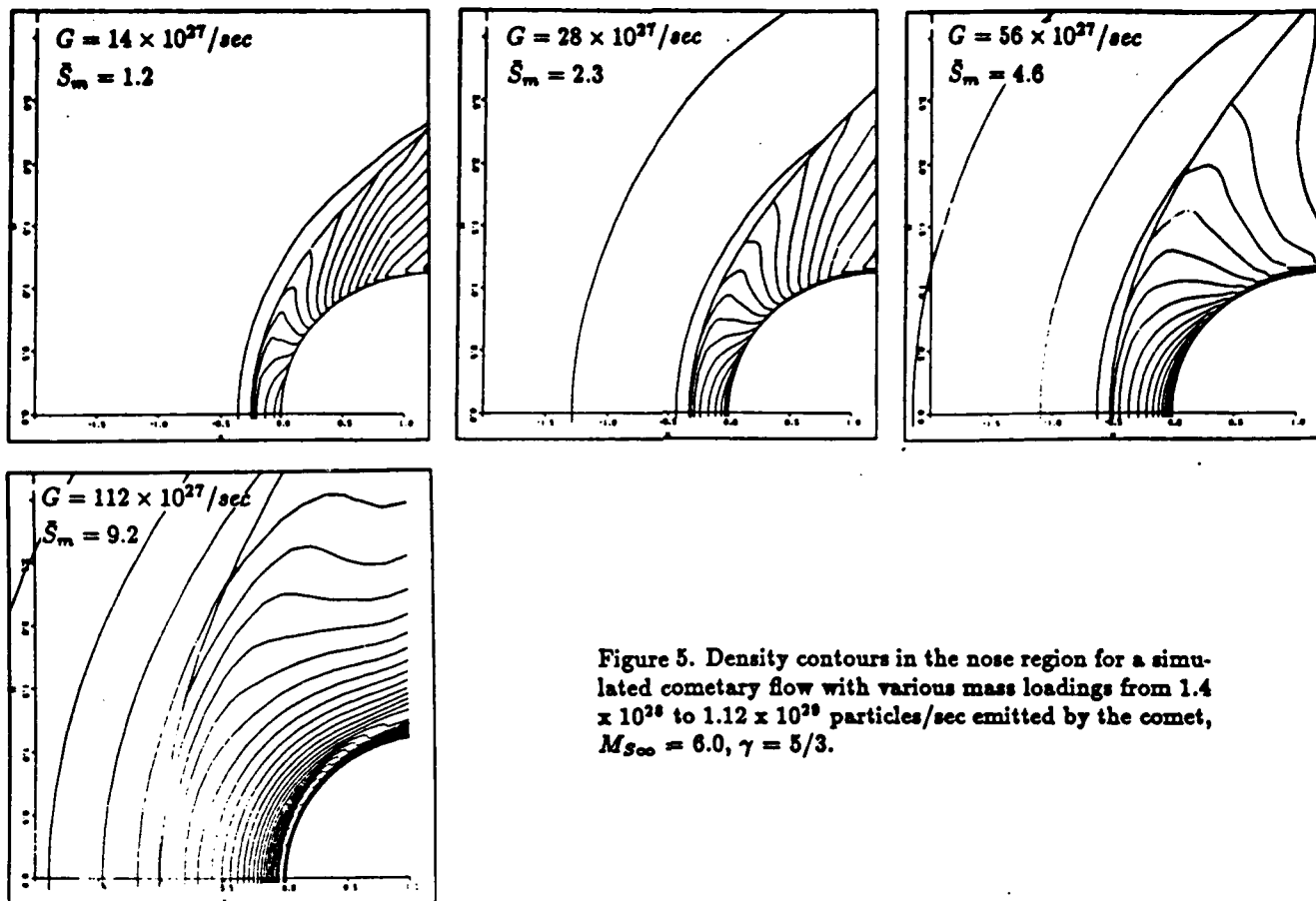


Figure 5. Density contours in the nose region for a simulated cometary flow with various mass loadings from 1.4×10^{28} to 1.12×10^{29} particles/sec emitted by the comet, $M_{S\infty} = 6.0$, $\gamma = 5/3$.

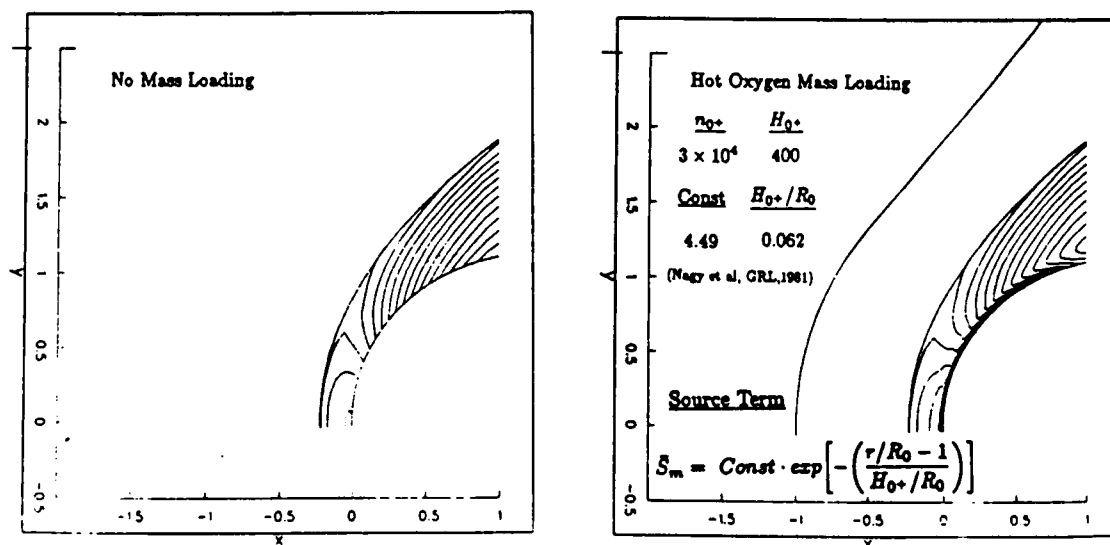


Figure 6. Calculated density contours in the Venusian ionosheath with and without mass loading due to photoionization of hot oxygen, $M_{S\infty} = 5.7$, $\gamma = 5/3$.

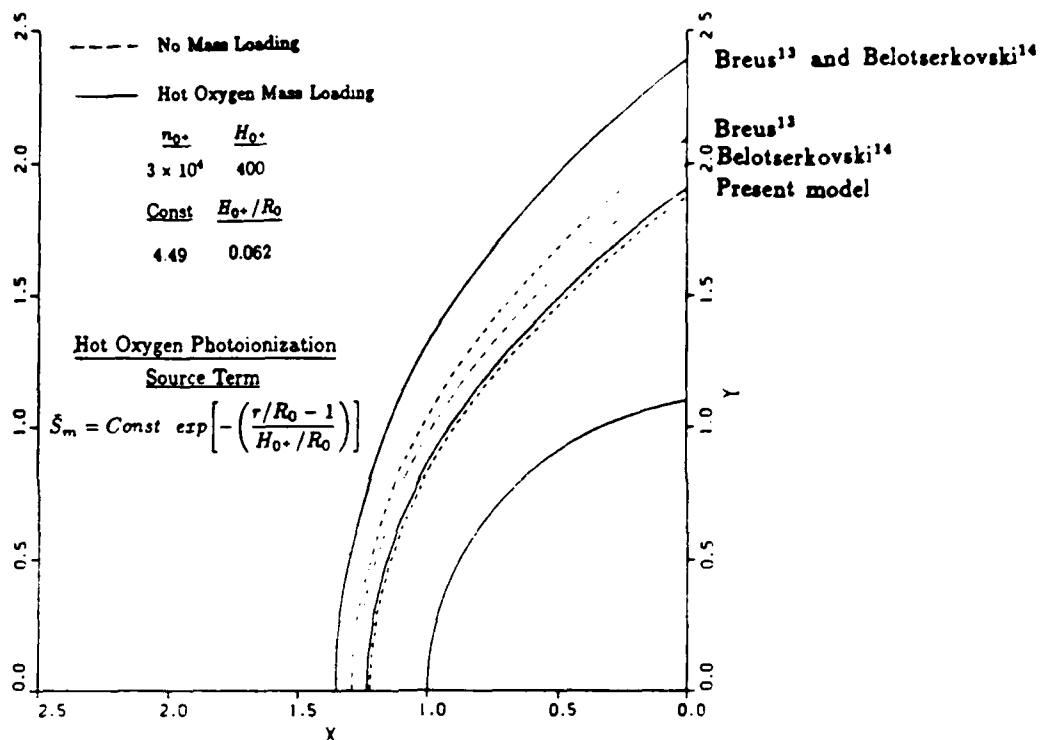


Figure 7. Comparison of present model results for the location of the Venusian bow shock wave with those of Breus¹³ and Belotserkovski¹⁴ with and without mass loading due to photoionization of hot oxygen, $M_{S\infty} = 5.7$, $\gamma = 5/3$.

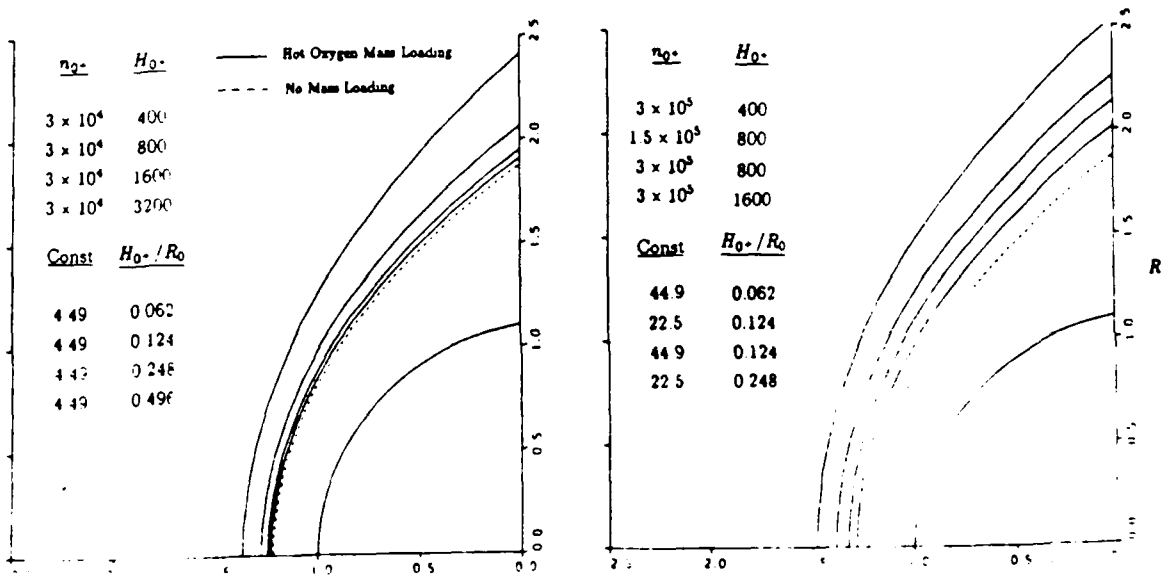


Figure 8. Predicted locations of the Venusian bow shock as a function of the mass source model constants for photoionization of hot oxygen, $M_{S\infty} = 5.7$, $\gamma = 5/3$.

A New Computational Model for Predicting Aligned MHD
Solar Wind Flow Past Planetary Magnetoionospheres:
Application to Earth and Venus

S S Stahara and G M Molvik (RMA Aerospace,
Inc., Mountain View, CA 94043; 415-961-0560)
J R Spreiter (Div. of Applied Mechanics,
Stanford University, Stanford, CA 94305; 415-723-
2891)

The development of a new computational model for predicting the global interaction of the solar wind with planetary magnetoionospheres at the full MHD accuracy level for situations when the IMF is aligned with the oncoming flow direction is described. The procedures developed are appropriate for supersonic, super-Alfvénic solar wind flows past general axisymmetric magnetoionosphere obstacle shapes. The computational model developed employs two separate but coupled flow field solvers to determine the steady flow field: (1) an asymptotic time-marching procedure for the subsolar to terminator region, and (2) a spatially-marching procedure for the post-terminator region. Both computational procedures are based on current, fully-implicit numerical algorithms, and both employ fitted discontinuity representations for the bow shock and magnetoionospheric obstacle surfaces. An outline of the numerical model and some of the computational details involved in its development are provided. Results of initial applications of the model to Earth and Venus are described. For the application to Earth, the results are compared to those previously determined by Spreiter and Rizzi (Acta Astr., 1974) using a completely different computational method. The current method predicts the identical variation of the bow shock shape as a function of Alfvén Mach number in the oncoming solar wind that was previously obtained, i.e. as the oncoming Alfvén Mach number decreases, the bow shock simultaneously moves inward toward the magnetopause in the nose region and flares outward away from the magnetopause along its flanks. For the application to Venus, the model results provide an important indication of the sensitivity of the Venusian bow shock to MHD effects, in particular the dependence of the bow shock location at the terminator on the Alfvén Mach number of the oncoming flow.

A THREE-DIMENSIONAL GASDYNAMIC MODEL
FOR SOLAR WIND FLOW PAST
NONAXISYMMETRIC MAGNETOSPHERES:
APPLICATION TO JUPITER AND SATURN

S. S. Stahara and R. R. Rachiele
RMA Aerospace, Inc., Mountain View, California

J. R. Spreiter
Division of Applied Mechanics, Stanford University
Stanford, California

J. A. Slavin
Goddard Space Flight Center
Greenbelt, Maryland

Abstract

The gasdynamic convected magnetic field model for predicting solar wind flow past a planetary magnetoionopause obstacle has been extended to three-dimensions to apply to obstacles of nonaxisymmetric shape. The need for such an extension is of first-order importance for Jupiter and Saturn because the effects of rapid spin, large size, and substantial ring current phenomena are believed to cause the magnetospheres of these

planets to be significantly broader near the planetary equatorial plane than near the noon-midnight polar meridian plane. Direct observational determination of such asymmetries for Jupiter and Saturn has not been possible, however, because only a limited amount of data are available from four spacecraft at Jupiter and three at Saturn, all of which followed flyby trajectories at fairly low latitudes. With the aid of the new three-dimensional model, it is now possible to infer the degree of flattening of the magnetospheric cross sections from a knowledge of the locations of the low-latitude magnetopause and bow shock crossings. In this paper, the computational procedures of the new model are described, and calculated results are presented for a number of magnetospheres of elliptic cross sections with values ranging from 1 to 2 for the ratio a/b of major (equatorial) to minor (polar) axes. This range is sufficient to include values appropriate to both Jupiter and Saturn. Comparisons of the model results with the locations of observed crossings of the magnetopause and bow shock directly provide an estimate of the degree of equatorial broadening of the magnetospheric cross section for each of these planets. For Jupiter, the results indicate a broadening to $a/b \sim 1.75$, a value consistent with previous estimates determined from independent calculations of the three-dimensional magnetosphere shape formed by adding to the planetary dipole field the magnetic field of an equatorial current sheet selected so as to match the observed Jovian magnetic field near the equatorial plane. For Saturn, a similar comparison indicates a smaller broadening to $a/b \sim 1.25$. The determination is less certain than for Jupiter, however, because of the smaller amount and greater scatter of the available data.

Introduction

The gasdynamic convected magnetic field approximation to the magnetohydrodynamic model for supersonic solar wind flow past a planetary magnetosphere has provided a useful basis for understanding the solar wind planetary interaction process from its inception more than two decades ago (Spreiter et al., 1966) to the present day (see e.g., Spreiter and Stahara, 1985; Slavin et al., 1985; and Russell, 1985, for recent reviews of the theory and applications). The original model calculations, although accurate, were tedious to perform with the methods available at the time. As a result, solutions were carried out for only a limited number of cases.

More recently Spreiter and Stahara (1980a,b) completely revised the solution procedures without changing the underlying physics in order to take advantage of the enormous advances in computer capability and computational methods that have occurred since the original model was conceived. They produced a well-documented model (Stahara et al., 1980) capable of routinely providing solutions for the detailed flow and magnetic field properties throughout the magnetosheath region between the bow shock and a rather arbitrarily specified smooth shape for the planetary magnetopause or ionopause. The results provided by the model are now widely used in the interpretation of spacecraft data, and in further extensions of the theory.

Throughout the theoretical development of the model, the shape of the magnetospheric obstacle has always been approximated as axisymmetric

about a line parallel to the incident aberrated solar wind direction and passing through the planetary center. For the earth, this has been justified by numerous studies of extensive observational data that have shown that any departure from axisymmetry is virtually immeasurable. More precisely, Fairfield (1971) and Holzer and Slavin (1978) have determined that the eccentricity e of the magnetospheric cross section in the terminator plane is less than 0.2. In this, the eccentricity is defined in the usual way as the positive root of $e = (1 - b^2/a^2)^{1/2}$ where a and b are the major and minor axes of an ellipse that best fits the observed magnetospheric cross section in the terminator plane. Since $e < 0.2$ correspond to values for a/b between 1 and 1.02 as can be readily determined using the equivalent relation $a/b = (1 - e^2)^{-1/2}$, the approximating elliptic cross section for the earth's magnetosphere differs only slightly from being circular. Furthermore, predicted results based upon an axisymmetric magnetopause shape have consistently been found to be in good agreement with observations of both the bow shock location and also of the plasma and magnetic field properties throughout the magnetosheath of the earth. Similar results have been found for the other terrestrial planets (Slavin et al., 1983), but notable differences appear in the corresponding comparisons for Jupiter and Saturn (Slavin et al., 1985).

All direct measurements of conditions in the magnetospheres and surrounding solar wind interaction regions at Jupiter and Saturn are those provided by flyby missions of Pioneer and Voyager spacecraft. Their trajectories as well as the average observed locations of the bow shock and magnetopause boundaries are shown in Figure 1 (see Slavin et al., (1985) and references therein). The spatial coverage provided by

the four spacecraft trajectories through the Jovian system and the three through the Saturnian system appears to be reasonably good, as viewed in the rotated cylindrical coordinate system of Figure 1. However, all of the trajectories were at fairly low latitudes, and no data whatsoever were obtained at high latitudes.

In spite of the scatter in the average boundary and bow shock locations, much of which can be accounted for by the effects of differing solar wind stagnation pressure $p_{st} \sim \rho_{\infty} U_{\infty}^2$, an orderly pattern of boundary and shock crossings at Jupiter can readily be recognized in Figure 1 even before application of corrections for variations in p_{st} . For Saturn, the situation is not so clear because the data display more scatter than can be accounted for by a simple scaling of the magnetosphere and bow shock according to known variations in p_{st} . It has been suggested, furthermore, that the distant locations of the magnetopause and bow shock observed by Voyager 2 may be the result of Saturn possibly being in the distant magnetic tail of Jupiter at the time of the encounter (see e.g., Scarf et al., 1977; Grzedzielski et al., 1981; Behannon et al., 1983; and Desch, 1983 for further discussion of this interesting possibility). Most of the expected effects of such an occurrence should be compensated for, however, by the stagnation pressure scaling procedure of Slavin et al. (1985) that has been applied to the observational data summarized in Figure 2, and subsequently herein.

In a comprehensive study of the positions of the magnetopause and bow shock of Jupiter and Saturn, Slavin et al. (1985) determined the least-square conic curve representations recast into nondimensional form in

Figure 2. The results for Jupiter show that the calculated bow shock based upon an assumed axisymmetric magnetopause shape that matches the observed equatorial magnetopause is everywhere displaced substantially farther from the magnetopause than the observations. The results for Saturn display a similar result near the nose of the bow shock. However, both the original least-square conic curve of Slavin et al. (1985), and an analogous new curve that includes effects of outbound Voyager 1 data excluded in the original determination may be seen to flare out even beyond the calculated axisymmetric shock near or downstream of the terminator plane. Temporarily setting aside this flaring at Saturn, which will be discussed separately, the differences between the calculated axisymmetric and the least-square observational shock locations in the nose region of each of these planets are substantial. More specifically, the calculated thickness of the magnetosheath in the subsolar region is 80 percent too great for Jupiter and 30 percent too great for Saturn.

Slavin et al. (1985), attributed these differences to a significant departure from axisymmetry in the magnetospheric shapes for these planets. In this view, the equatorial regions of the magnetopause are broadened with respect to the polar regions by effects of a large equatorial ring current system (Engle and Beard, 1980) brought about, presumably, by centrifugal effects associated with the large angular velocity ω and low mean density ρ_p of these planets.

The equatorial broadening hypothesis is consistent with most of the results shown in Figure 2 since the axisymmetric shape that results from

rotating the observed equatorial magnetopause trace about the symmetry axis produces a shape that has a significantly larger cross-section area than a flattened shape having the same equatorial magnetopause trace. As a result, the bow shock about an axisymmetric magnetopause will be everywhere farther from the magnetopause than it is for a flattened magnetopause having the same equatorial shape, just as shown for Jupiter and near the magnetopause nose for Saturn.

To appreciate the enhanced effects of centrifugal forces in the Jupiter and Saturn magnetospheres compared with those for the earth, note that the synchronous orbital distance r_s beyond which the centrifugal force $r\omega^2$ per unit mass corotating with the planet in the equatorial plane exceeds the gravitational force $GM/r^2 = 4\pi G\rho_p R_p^3/3r^2$, where $G = 6.668 \times 10^{-8}$ dynes $\text{cm}^2 \text{g}^{-2}$ is the gravitational constant, and R_p is the planetary radius, is at a normalized planetary distance $r_s/R_p = [4\pi G_p/(3\omega^2)]^{1/3} \sim 6.6$ for the earth, but only about 2.2 and 1.8 for Jupiter and Saturn. However, a more appropriate indicator of centrifugal flattening of the magnetosphere is the ratio of r_s to a representative dimension of the magnetospheric obstacle, rather than the planetary radius. If this dimension is taken to be the planetocentric distance R_0 to the magnetopause nose, where $R_0 = (10R_e, 58.6R_J, 19.7R_S)$ for the earth, Jupiter and Saturn, the resulting values for r_s/R_0 are 0.66 for the earth, and only 0.04 and 0.09 for Jupiter and Saturn. This clearly shows that centrifugal force on corotating matter dominates over gravitational force throughout a much larger fraction of the Jupiter and Saturn magnetospheres than it does for the earth.

On the basis of the available observations, Slavin et al. (1985) proposed an equatorial broadening hierarchy similar to that illustrated in Figure 3 for the magnetopause cross sections in the terminator plane. As discussed above, the cross section of the earth's magnetosphere is essentially circular with an eccentricity $\epsilon \leq 0.2$, which corresponds to a ratio of major to minor axes of $1.00 \leq a/b \leq 1.02$. In contrast, they concluded that Jupiter's magnetosphere is broadened into an ellipse with $\epsilon \sim 0.8$, or $a/b \sim 5/3$. The corresponding values for Saturn were not determined with an equal precision, but it was concluded that planet presents an intermediate case with $0 \leq \epsilon \leq 0.8$, or $1 \leq a/b \leq 5/3$. Our results are most consistent with the Pioneer and Voyager observations when values for a/b are set to 1.25 for Saturn and 1.75 for Jupiter, and the cross sections for those planets are drawn accordingly in Figure 3. In each case, the shock position is that calculated at the terminator plane using representative values of 2 for the ratio of specific heats γ , and 8, 10 and 12 for the Mach number of the solar wind approaching earth, Jupiter and Saturn.

To provide the appropriate theoretical solutions for application to equatorially broadened magnetospheres, we have extended our previous axisymmetric analysis so that it can be applied to the interaction of the solar wind flow with a general three-dimensional magnetoionospheric obstacle. This extension serves the dual purpose of providing (a) more accurate theoretical capability required for comparative studies with observations of the solar wind interaction with substantially nonaxisymmetric planetary magnetospheres, and (b) an important element of a general interactive scheme in which the three-dimensional shape of the

magnetoionopause and the surrounding flow and magnetic fields for any planet are calculated alternately in the process of converging toward an exact solution of the magnetohydrodynamic equations.

The new computational model is described in this paper, and results are presented for the calculated shape of the bow shock and the flow properties in the magnetosheaths of equatorially broadened magnetospheres having elliptic cross sections representative of those suggested for Jupiter and Saturn. By comparison of these results with the observed locations of the low-latitude magnetopause and bow shock crossings, a quantitative determination is obtained for the degree of equatorial broadening of the magnetospheres of Jupiter and Saturn. The new three-dimensional results for these broadened magnetospheres are shown to be in satisfactory agreement with the observations near these planets, and to account for most of the differences between the observations and the axisymmetric model results indicated previously by Slavin et al. (1985).

Mathematical Model and Solution Procedure

The fundamental assumption underlying the present work, as in our previous analyses of axisymmetric flows reported in the references cited above, is that the bulk properties of the solar wind plasma flow around a planetary magnetoionosphere can be described adequately for many purposes by solutions of the continuum equations of magnetohydrodynamics of a perfect gas having infinite electrical conductivity and zero viscosity and thermal conductivity. The primary justification for this assumption

is provided not by rigorous proof, but by the outstanding general agreement of the calculated results with a large amount of direct observations in space.

Under this assumption, the equations used to describe the flow of the solar wind plasma past a planetary magnetosphere are those of single-fluid dissipationless magnetohydrodynamics for the conservation of mass, momentum, energy, and magnetic flux, augmented by the equation of state for a perfect gas and by entropy considerations. These equations have been given many times (see Spreiter and Stahara, 1985, for our most recent account), and will not be repeated here.

In addition to the differential equations and auxiliary relations referred to above, boundary and initial conditions must be specified for the properties of the solar wind upstream of the bow shock wave, and for the size and other relevant properties of the planet for which a solution is sought. For a planet with a strong dipolar component to the magnetic field, like the earth, Jupiter, and Saturn, the pertinent parameters are the strength and orientation of the planetary field.

In common with most studies of the present type, we assume that the flow is steady and that the dipole field is stationary in time. As will be commented upon further in the discussion of the results, the large dimensions of the magnetospheres of Jupiter and Saturn cause these assumptions to be much more restrictive than they are in applications to the earth and other terrestrial planets.

For typical solar wind conditions, particularly at the locations of the outer planets, both the oncoming sonic Mach number $M_{S\infty} = V_{\infty}/(\gamma p_{\infty}/\rho_{\infty})^{1/2}$ and the Alfvén Mach number $M_{A\infty} = V_{\infty}/(B_{\infty}^2/(4\pi\rho_{\infty}))^{1/2}$ are high (of the order of 10). Under these conditions, an important simplification of the magnetohydrodynamic equations occurs because the magnetic terms may be disregarded as small in the momentum and energy conservation equations. With these terms omitted, the magnetohydrodynamic equations separate into two sets. One is the ordinary gasdynamic equations for the flow of a perfect inviscid gas. The other set is the Faraday magnetism equations for a perfectly conducting medium.

The equations for the fluid motion about an obstacle of given shape thus reduce to those of gasdynamics, and can be solved without further consideration of the magnetic field. The magnetic field can be determined subsequently by solving the remaining Faraday equations using the values for the velocity and density fields calculated using the gasdynamic equations. Because the magnetic field determined in this fashion is usually interpreted, although somewhat ambiguously, as being "frozen-in" or "moving with the fluid", the resulting equations and the model they represent are commonly referred to as the gasdynamic convected field approximation. It should be noted, however, that the interpretation of the field as frozen-in or moving with the fluid is not dependent upon the separation of the determination of the fluid motion from that of the magnetic field, but is actually an exact consequence of the basic assumption that the flow can be represented by the magnetohydrodynamic equations for a dissipationless electrically conducting perfect gas.

In carrying out the decoupled gasdynamic calculation, the shape of the magnetoionopause is not known a priori, but must be found as part of the overall solution. In our previous analyses, the magnetoionopause shape has been determined by either an independent approximate theoretical analysis, a synthesis of actual observational results, or a combination thereof. The latter procedure has also been employed in the present analysis.

Numerical solutions of the full magnetohydrodynamic equation set without resort to the gasdynamic convected field approximation now exist, but they are still in a fairly early state of development, require large computational resources, and lack adequate resolution for many purposes. In summarizing the situation recently, Russell (1985) stated, "Currently, the only way to achieve the spatial resolution needed for a useful comparison with data obtained on a pass through a planetary magnetosheath is to employ the gasdynamic convected field model".

One of the most important features of both the current three-dimensional and previous axisymmetric models is the use of two separate, but coupled, computational procedures for determining the steady flow field. As illustrated in Figure 4, the first of these is a nose region solver that determines the transonic flow field from the subsolar region to or somewhat beyond the terminator location by using an unsteady procedure that marches the solution forward in time from a somewhat arbitrarily imposed initial state to the asymptotic steady state solution. That solver is then linked together with a spatially-marching tail region

solver that advances the supersonic flow field solution downstream to any arbitrary distance in which the flow remains supersonic.

The choice of axial location at which the two solutions are joined is relatively arbitrary, the most important requirement being that imposed by the spatially-marching solver that the axial component of the local sonic Mach number be greater than unity everywhere at the joining plane. In most of our previous applications, it was convenient to join the two solutions at the plane through the planetary center oriented normal to the oncoming solar wind direction, which we term the terminator plane. For some cases involving magnetoionopause obstacles with enhanced flaring at the terminator, it has been found necessary to join the solutions at a plane some fraction of an obstacle nose radii downstream of the terminator in order to satisfy the requirement of supersonic axial velocity component.

For clarification, it should be noted that our definition of the terminator plane differs slightly from the standard definition based on visual considerations as the plane through the planetary center oriented normal to the sun-planet line. The orientations of the two planes differ by the small angle between the upstream direction and the sun-planet line, and is due primarily to the aberration effects of the orbital motion of the planet through the much higher speed and nearly radial outflow of the solar wind from the Sun. For earth, this angle is usually about 5° , but substantially smaller values would be anticipated for Jupiter and Saturn. The reason is that (a) the average radial velocity of the solar wind is nearly independent of distance from the

Sun throughout this part of the Solar System, and (b) the orbital velocity of a planet varies inversely as the square root of its distance from the Sun. Since this distance is approximately 5.2 and 9.5 times greater for Jupiter and Saturn than for the earth, the corresponding difference between the orientations of the alternately defined terminator planes is only about 2.2° for Jupiter and 1.6° for Saturn.

The reason for expending the substantial additional effort to develop such a coupled two-flow solver combination, rather than employing a single time-marching solver for the entire flow field as is done in all existing magnetohydrodynamic solutions procedures, are twofold. First, there is a huge gain in computational efficiency because the computationally expensive time-marching procedure required to treat the subsonic/transonic flow in the nose region is used only where needed, while the remainder of the solution is obtained using a highly efficient spatially marching procedure appropriate for supersonic flow. Secondly, a computational capability is attained to determine flow conditions as arbitrarily far downstream alongside a specified magnetotail surface as needed. Such an extended capability cannot be provided by a time-marching procedure alone. Finally, we note that such a subdivision of the solution procedures is quite common in calculating supersonic/hypersonic flows past blunt nosed bodies. It has been used throughout not only all our previous work, but also, for example, in the analysis of flow past a reentry body such as the space shuttle.

Nose Region Solution Procedure

In the nose region, we have adapted the procedure of Rizk et al. (1983) to solve the unsteady, three-dimensional dissipationless gasdynamic partial differential equations governing the conservation of mass, momentum, and energy. Upon introduction of the generalized independent variable transformation $\tau = t$, $\xi = \xi(x,y,z)$, $\eta = \eta(x,y,z)$, $\zeta = \zeta(x,y,z)$, these equations can be written in strong conservation law form as:

$$\hat{Q}_\tau + \hat{E}_\xi + \hat{F}_\eta + \hat{G}_\zeta = 0 \quad (1)$$

where

$$\hat{Q} = \frac{1}{J} \begin{bmatrix} \rho \\ \rho U \\ \rho V \\ \rho W \\ e \end{bmatrix}$$

$$\hat{E} = \begin{bmatrix} \rho U \\ \rho U^2 + \xi_x p \\ \rho V U + \xi_y p \\ \rho W U + \xi_z p \\ (e+p)U \end{bmatrix}$$

$$\hat{F} = \frac{1}{J} \begin{bmatrix} \rho V \\ \rho U V + \eta_x p \\ \rho V^2 + \eta_y p \\ \rho W V + \eta_z p \\ (e+p)V \end{bmatrix}$$

$$\hat{G} = \begin{bmatrix} \rho W \\ \rho U W + \zeta_x p \\ \rho V W + \zeta_y p \\ \rho W^2 + \zeta_z p \\ (e+p)W \end{bmatrix}$$

(2)

Here (u,v,w) are the Cartesian velocity components, ρ and p are density and pressure, e is the internal energy which is related to pressure by $p = (\gamma-1)[e - (u^2 + v^2 + w^2)/2]$, where γ is the ratio of specific heats. (U,V,W) are the contravariant velocities without metric normalization given by

$$\begin{aligned}
 U &= u \xi_x + v \xi_y + w \xi_z \\
 V &= u \eta_x + v \eta_y + w \eta_z \\
 W &= \zeta_t + u \zeta_x + v \zeta_y + w \zeta_z
 \end{aligned}
 \tag{3}$$

in which (ξ_x, ξ_y, ξ_z) , (η_x, η_y, η_z) , $(\zeta_x, \zeta_y, \zeta_z)$ are the transformation metrics, and J is the Jacobian of the transformation. At each time step the transformation metrics are unknown and must be determined as part of the solution. In our implementation, they are evaluated numerically using second-order central differences. The time dependent metric terms are functions of the instantaneous shock speed, which is determined from the shock fitting procedure of Kutler et al. (1980).

The numerical algorithm used to solve the above equations is based on the Beam and Warming (1976) procedure. The method is employed in delta form and is fully implicit, noniterative, second-order accurate in space, and spatially factored. When applied to equation (1), the algorithm can be written as:

$$\begin{aligned}
& [I + \Delta t \delta_{\xi} \hat{A} - \epsilon_i J^{-1} \nabla_{\xi} \Delta_{\xi} J] \cdot [I + \Delta t \delta_{\eta} \hat{B} - \epsilon_j J^{-1} \nabla_{\eta} \Delta_{\eta} J] \cdot \\
& [I + \Delta t \delta_{\zeta} \hat{C} - \epsilon_k J^{-1} \nabla_{\zeta} \Delta_{\zeta} J] \Delta \hat{q} = -\Delta t [\delta_{\xi} \hat{E} + \delta_{\eta} \hat{F} + \delta_{\zeta} \hat{G}] \\
& - \epsilon_e J^{-1} [(\nabla_{\xi} \Delta_{\xi})^2 + (\nabla_{\eta} \Delta_{\eta})^2 + (\nabla_{\zeta} \Delta_{\zeta})^2] J \hat{q}
\end{aligned}
\tag{4}$$

where $(\hat{A}, \hat{B}, \hat{C})$ are the Jacobian matrices $\hat{A} = \partial \hat{E} / \partial \hat{q}$, $\hat{B} = \partial \hat{F} / \partial \hat{q}$, $\hat{C} = \partial \hat{G} / \partial \hat{q}$, $\Delta \hat{q} = (q/J)^{n+1} - (q/J)^n$ where n represents the time level, $(\delta_{\xi}, \delta_{\eta}, \delta_{\zeta})$ represent second-order central difference operators, (ϵ_i, ϵ_e) are implicit second-order and explicit fourth-order smoothing parameters, (∇, Δ) represent first-order backward and forward difference operators, and t is the time step. A single time step integration of equation (4) consists of three separate inversion steps associated with each of the three spatial directions (ξ, η, ζ) . Each inversion step involves the solution of a 5x5 block tridiagonal system. Integration step size is established by using the maximum eigenvalue of the Jacobian matrices $(\hat{A}, \hat{B}, \hat{C})$.

The analysis is initiated by introducing a computational mesh to discretize the flow field. For the present three-dimensional model as well as in all our previous work, we employ a fitted discontinuity surface representation of both the bow shock and the magnetospheric obstacle. For application to three-dimensional planetary magnetospheres we have found it convenient to develop a mesh generator based upon a generalized spherical (r, θ, ϕ) coordinate system with the origin usually located at the planetary center, but occasionally shifted downstream from that location on a line through the planetary center and

parallel to the oncoming solar wind. Although the basic method imposes no such requirement for the calculations presented here, it has been assumed that the magnetopause shape and associated flow field possess bilateral or quadrilateral symmetry about the equatorial plane and the polar meridian plane.

The associated Cartesian (x,y,z) coordinate axes and a typical grid employed in our analysis are illustrated in Figure 5 where a perspective cut out view of one quadrant of the flow field is provided. In that figure the origin coincides with a location approximately half of an obstacle radius downstream of the planetary center and the x-axis, which coincides with the longitudinal axis of the magnetosphere, points directly into the oncoming solar wind. The y axis lies in the planetary magnetic equatorial plane, and the z axis points in the north polar direction. In Figure 5, the obstacle to shock (r, θ) grids in the azimuthal planes containing the x-z ($\phi = 0^\circ$) and x-y ($\phi = 90^\circ$) axes are shown together with the mesh distribution on the magnetopause surface, and the outflow boundary grid located in the y-z plane at the final downstream x location.

The quadrant of the (r, θ , ϕ) mesh shown in Figure 5 contains (19,30,9) points, with the 9 azimuthal planes spaced at equal 10° increments. In each azimuthal plane, the capability of generating a body normal mesh has been implemented in the grid generator. A clustering capability has also been implemented to enable independent grid point clustering in each of the three coordinate directions. For the magnetospheric obstacle shown in Figure 5, which represents an equatorial broadened

Jupiter magnetopause with $a/b = 1.75$, the equal angular distribution of the azimuthal planes results in a natural clustering of the grid spacing on the body in the polar region in contrast to that in the equatorial region. This can be retained or easily modified if desired by employing the clustering option.

Boundary conditions necessary for specifying a properly posed mathematical problem are that the flow satisfy the unsteady Rankine-Hugoniot shock relations along the moving bow shock surface, be entirely supersonic at the downstream outflow boundary, possess bilateral or quadrilateral symmetry about the stagnation streamline at the nose, and be tangential to the obstacle at its surface. Initial flow field conditions are determined by use of an approximating surface for the bow shock wave, and by prescribing a modified Newtonian pressure distribution on the surface of the magnetopause. Since the maximum entropy streamline wets the obstacle, that fact plus the flow tangency condition on the magnetopause serve to determine the remainder of the flow properties on that surface. A linear variation for the flow properties between the bow shock and the magnetopause then provides the starting flow field which is then integrated in a time-asymptotic fashion until the steady state solution is obtained.

At the boundaries, modification of the differencing algorithm to account for the appropriate conditions described above is accomplished as follows. For the fitted discontinuity surface representing the bow shock, the flow variables immediately downstream of the shock are determined using the unsteady shock fitting procedure of Kutler et al.

(1980). At the outflow boundary where the flow is entirely supersonic, the dependent variables are determined by extrapolation from the adjacent interior points. Along the stagnation streamline, which forms a singularity line due to our use of a spherical-like coordinate system (Pulliam and Steger, 1978), symmetry conditions are enforced by employing a second-order-accurate averaging procedure. Also incorporated in the numerical solver is the capability to enforce symmetry boundary conditions across any two arbitrary azimuthal planes. For the present application, all members of the family of three-dimensional obstacles being considered possess quadrilateral symmetry about two orthogonal azimuthal planes passing through the equator and the polar meridians. Consequently, the flow calculations can be restricted to a single quadrant as shown in Figure 5, thereby reducing by a factor of four the number of grid points at which the solution must be determined. The obstacle surface flow tangency condition is incorporated by setting the contravariant velocity component normal to the surface equal to zero, and then determining the other two contravariant velocity components and the density at the obstacle surface by extrapolation from interior points. The total energy is then evaluated by using that information together with the pressure computed from the normal momentum equation. The interior flow field bounded by these various boundaries is treated in shock-capturing fashion and therefore allows for the accurate determination of secondary shocks, should any occur.

Tail Region Solution Procedure

In the tail region, we have employed the shock capturing technique of Kutler et al. (1973) to solve the steady, three-dimensional dissipationless gasdynamic equations. The conservation equations for mass and momentum written in weak conservation law form in cylindrical (x, R, ϕ) coordinates can be written as:

$$\tilde{U}_x + \tilde{F}_R + \tilde{G}_\phi + \tilde{H} = 0 \quad (5)$$

where the four-component vectors $(\tilde{U}, \tilde{F}, \tilde{G}, \tilde{H})$ are defined by

$$\begin{aligned} \tilde{U} &= \begin{bmatrix} \rho u \\ p + \rho u^2 \\ \rho uv \\ \rho uw \end{bmatrix} & \tilde{F} &= \begin{bmatrix} \rho v \\ \rho uv \\ p + \rho v^2 \\ \rho vw \end{bmatrix} \\ \tilde{G} &= \begin{bmatrix} \rho w \\ \rho uw \\ \rho vw \\ p + \rho w^2 \end{bmatrix} & \tilde{H} &= \begin{bmatrix} \rho v \\ \rho uv \\ \rho(v^2 - w^2) \\ 2\rho vw \end{bmatrix} \end{aligned} \quad (6)$$

in which (u, v, w) denote velocity components in the (x, R, ϕ) coordinate directions. The governing set of equations is completed with the addition of energy conservation as given by the equation for the total enthalpy

$$H_t = h(p,p) + q^2/2 = \text{const} \quad (7)$$

Here q is the magnitude of the velocity vector and $h(p,p)$ represents the static enthalpy which for a perfect gas is given by $[\gamma/(\gamma-1)](p/\rho)$.

The governing equations are transformed to a computational space using the independent variable transformation $\xi = x$, $\eta = (R-R_b)/(R_s-R_b)$, $\zeta = \phi$, where (R_s, R_b) represent the cylindrical radial coordinate of the bow shock and body surface, respectively, and ϕ is the azimuthal angle. This yields the conservation equation

$$\bar{U}_\xi + \bar{F}_\eta + \bar{G}_\zeta + \bar{H} = 0 \quad (8)$$

where

$$\bar{U} = \tilde{U}$$

$$\bar{F} = \frac{\{\tilde{F} - [R_b + \eta(R_s - R_b)]_\xi \tilde{U} - [R_b \zeta + \eta(R_s - R_b)]_\zeta \tilde{G}\}}{R_s - R_b}$$

$$\bar{G} = \tilde{G}$$

$$\bar{H} = \tilde{H} + \frac{[(R_s - R_b)_\xi \tilde{U} + (R_s - R_b)_\zeta \tilde{G}]}{R_s - R_b} \quad (9)$$

The numerical algorithm chosen to solve equation (8) is MacCormack's explicit second-order accurate predictor-corrector method. As applied to equation (9), the algorithm can be written as:

$$O_{i,j}^* = O_{i,j}^n - \frac{\Delta\xi}{\Delta\eta} (\bar{F}_{i+1,j}^n - \bar{F}_{i,j}^n) - \frac{\Delta\xi}{\Delta\zeta} (\bar{G}_{i,j+1}^n - \bar{G}_{i,j}^n) - \Delta\xi \bar{H}_{i,j}^n$$

$$\begin{aligned} \bar{U}_{i,j}^{n+1} = & \left(\frac{1}{2}\right) \{ \bar{U}_{i,j}^n + \bar{U}_{i,j}^* - \frac{\Delta\xi}{\Delta\eta} (\bar{F}_{i,j}^* - \bar{F}_{i-1,j}^*) - \frac{\Delta\xi}{\Delta\zeta} (\bar{G}_{i,j}^* \\ & - \bar{G}_{i,j-1}^*) - \Delta\xi \bar{H}_{i,j}^* \} \end{aligned} \quad (10)$$

where

$$\begin{aligned} \bar{U}_{i,j}^n &= \bar{U}(n\Delta\xi, i\Delta\eta, j\Delta\zeta) \\ \bar{F}_{i,j}^n &= \bar{F}(\bar{U}_{i,j}^n, n\Delta\xi, i\Delta\eta, j\Delta\zeta) \\ \bar{F}_{i,j}^* &= \bar{F}(\bar{U}_{i,j}^*, (n+1)\Delta\xi, i\Delta\eta, j\Delta\zeta), \text{ etc.} \end{aligned} \quad (11)$$

Subsequent to each integration step of equation (10) with respect to the hyperbolic marching coordinate ξ , the physical flow variables (p.p.u.v.w) must be decoded from the components u_i of U . This necessi-

tates the solution of five simultaneous nonlinear equations consisting of equation (7) together with the four elements $u_j = (p, p+\rho u^2, \rho uv, \rho uw)$. For a perfect gas, the procedure yields a quadratic equation that can be solved for the supersonic velocity component u . The remaining physical variables can then be determined directly.

At the bow shock, the fitted shock discontinuity approach of Thomas et al. (1972) is employed, while at the obstacle surface the surface tangency condition is enforced by applying the method of Abbett (1971). Integration step size in the marching direction is redetermined at each location so as to allow the maximum possible step size consistent with stability.

The numerical calculations for which results are reported here were performed on the NASA Ames Research Center CRAY XMP computer facility. Approximately 20 to 30 minutes of CPU time were typically required for the calculations for a single case of the three-dimensional magnetosphere shapes considered in this study. Essentially all of this time is spent with the nose region solver. For the family of three-dimensional shapes studied, the tail region solver is extremely rapid and can carry the solution downstream 10 obstacle nose radii in typically less than 10 CPU seconds. As a final run time comparison, we note that the typical CRAY XMP CPU time required for a single case by the combined nose and tail axisymmetric model to determine an analogous flow field is approximately 15 seconds.

Results and Applications to Jupiter and Saturn

Figure 6 shows the calculated results for the magnetopause and bow wave locations for conditions representative of those suggested by Slavin et al. (1985) as appropriate for Jupiter. These conditions are that the flow has a free-stream sonic Mach number $M_{S\infty}$ of 10 and ratio of specific heats γ of 2.0, and the magnetopause has an elliptic cross section with constant ratio of major to minor axes a/b of 1.75, corresponding to an eccentricity ϵ of .821. The equatorial magnetopause profile is taken to approximate that deduced from observations at Jupiter. Calculation of a converged solution for these conditions has been carried out over the region extending from the nose of the bow shock to about 1 magnetopause nose distance or about 60 Jupiter radii, downstream of the planetary center. The results, in the form of traces of the magnetopause and the bow shock in (a) each of the ten equally-spaced azimuthal grid planes from the equatorial plane to the noon-midnight polar plane of symmetry and (b) the terminator plane, display that the flattening of the bow shock is much less than that of the magnetopause.

Properties of this three-dimensional flow field are presented in Figure 7. In that figure, contour plots of the density ρ/ρ_∞ , pressure p/p_∞ , temperature T/T_∞ , flow speed V/V_∞ , and the sonic Mach number M_S in the noon-midnight polar meridian and equatorial planes are presented together with an isometric drawing of the magnetopause and bow shock in the equatorial and noon-midnight meridian planes. These contours

clearly indicate the smoothness and highly-converged nature of the three-dimensional solution for these magnetopause shapes.

Figure 8 shows calculated results similar to those of Figure 6 for $M_{S\infty} = 12$, $\gamma = 2.0$, and $a/b = 1.25$, corresponding to $\epsilon = 0.6$, selected as representative of conditions at Saturn. The equatorial magnetopause profile is that deduced by Slavin et al. (1985) from the Pioneer and Voyager observations at Saturn. As in Figure 6, the results show that the flattening of the trace of the bow shock in the terminator plane is much less than that of the magnetopause. It is also much less flattened than the bow wave for Jupiter, as would be expected in view of the substantially less flattened shape of the Saturn magnetopause.

Figure 9 presents a comparison of the least-squares fitted conic curves of Slavin et al. (1985) representing the Jovian magnetopause and bow shock crossings observed near the equatorial plane with the model-predicted bow shock shapes calculated for the same equatorial magnetopause shape and for four values for a/b , namely 1.00 (circular cross section), 1.50, 1.75 and 2.00, that bracket the value of $5/3$ suggested by Slavin et al. (1985). The results show that the bow shock is farthest out for the axisymmetric magnetosphere and moves progressively nearer as the flattening of the magnetospheric cross section increases. This is appropriate because the cross-section area of the magnetosphere is largest for the axisymmetric case, and diminishes progressively as the magnetopause is flattened from a/b of 1.00 to 2.00, thereby presenting less of an obstruction to the flow.

Comparison with the observations for Jupiter show that they are in close accord with the calculated results for $a/b = 1.75$, the magnetospheric shape of our set of examples with elliptic cross-section closest to that proposed for Jupiter by Slavin et al. (1985). This finding is also consistent with the result of Engle and Beard (1980) in which the three-dimensional shape of the Jovian magnetosphere was calculated for a planetary dipole field supplemented by an equatorial current sheet chosen to reproduce the observed Jovian magnetic field near the equatorial plane. All of this confirms the general expectation that, provided the solution is determined for a suitably flattened magnetopause, the gasdynamic convected field model should provide an even better representation for the magnetosheath plasma and field properties at Jupiter than at earth because of the high sonic and Alfvénic Mach numbers that prevail there.

On the other hand, the assumption that the flow is steady and that the dipole field is stationary is less appropriate for Jupiter and Saturn than for the earth or other terrestrial planets because of the immense size of their magnetospheres and bow shocks. Whereas the geocentric distance to the nose of the earth's bow shock is about 8.2×10^4 km, the corresponding distances for Jupiter and Saturn are 5.3×10^6 km and 1.75×10^6 km. Note that both of the latter are greater than the 1.4×10^6 km diameter of the sun.

Less than 4 minutes is thus required for the solar wind with a velocity of 400 km/s to flow a distance equal to that from the nose of the bow shock to the terminator plane for the earth. For the forward part of

the magnetopause and the surrounding flow field to reach a quasi-steady state, it may be expected that a period of the order of, say, twice this time, or 8 minutes, is required. For Jupiter and Saturn, the corresponding solar wind travel times are about 220 and 75 minutes, so that the times required to reach a quasi-steady state may be expected to be of the order of 7.3 and 2.5 hours, respectively. These are exceptionally long periods for conditions in the solar wind, particularly the magnetic field, to remain essentially steady.

A second source of unsteady conditions in the Jupiter magnetosphere is associated with the coning of the magnetic dipole axis as a result of planetary spin and the angular offset of this axis from the spin axis. These effects can be disregarded rather safely for the earth, even though there is an angle of 11.5° between these two axes, because the solar wind flowing at 400 km/s will travel 1.7×10^7 km 2700 earth radii in 12 hours, a distance equal to about 200 times the distance from the bow shock nose to the terminator plane. Furthermore, it has been long established, see Spreiter and Briggs (1962) or Spreiter and Stahara (1985) and numerous studies of the observed positions of magnetopause crossings, that the shape of the earth's magnetopause is remarkably insensitive to the $\pm 11.5^\circ$ daily, or even the combined $\pm 35^\circ$ yearly-daily, variation of the tilt of the dipole relative to the direction of the incident wind. The effects would also appear to be negligible for Saturn because its dipole axis is aligned within 1° of the spin axis and there is thus no significant coning of the dipole axis.

The matter is not so simply dismissed for Jupiter, however. The dipole magnetic field for this planet, which rotates once about every 10 hours, is inclined 11° to the spin axis. Since a 400 km/s solar wind flows about 7.2×10^6 km in 5 hours, it follows that the solar wind advances only about 1.3 times the distance from the bow shock nose to the terminator plane during the time the magnetic axis makes half a revolution around the spin axis. This clearly would have to be taken into account in the calculation of the magnetic field within the magnetosphere and its tail, and perhaps the shape of the magnetopause downstream of, say, the terminator plane. On the basis of the insensitivity of the magnetopause shape cited above for the earth, we believe, however, that the results provided by the steady-state model, particularly those upstream of the terminator plane, are not adversely affected to any significant degree for many applications.

Figure 10 shows the corresponding results for conditions suggested by Slavin et al. (1985) as representative of Saturn. These are that the flow has a free-stream sonic Mach number M_{S_∞} of 12, a value of 2.0 for the ratio of specific heats γ , and is about a magnetopause having the indicated shape in the equatorial plane and an elliptic cross section with constant ratio of major to minor axes a/b somewhere between that for the earth and Jupiter. Calculated equatorial plane traces of the bow shock are presented for magnetopause shapes with $a/b = 1.00$ (circular cross section), 1.15, 1.25, 1.35 and 1.45 together with the least-square curve fitted to the observations at Saturn by Slavin et al. (1985), and also the new least-square conic curve included on Figure 2.

The results calculated for $a/b = 1.25$ provide a good match to the least-square fitted conic curves near the nose of the bow shock. However, the latter flares out much farther from the planet than not only the calculated results for $a/b = 1.25$, but the results for all the calculated cases, including the axisymmetric magnetopause. This result is surprising in view of the generally satisfactory agreement between the results of the gasdynamic calculations and the observations for all the other planets, and has been commented on by Russell (1985) and Slavin et al. (1985).

Prompted by suggestions of Dr. R. P. Lepping of NASA Goddard Space Flight Center, we have re-examined the procedures used by Slavin et al. (1985), to determine their least-square conic curves for the bow shock and magnetopause for Saturn and arrived at the new least-square conic curve included in Figures 2 and 10. This curve is fitted to the stagnation-pressure-corrected observations using the same techniques as employed by Slavin et al. (1985), but including the data from Voyager 1. Those observations were not included in the original determination because the shock crossings occurred approximately two magnetopause nose distances downstream of the terminator plane, and did not meet the general modeling criteria set up and used previously by Slavin and Holzer (1981) and Slavin et al. (1983) in analyses of observations of the terrestrial planets. To ensure comparability of the models for the magnetopause and bow shock shapes for Jupiter and Saturn with similar ones for Venus, earth and Mars, the Voyager 1 crossings were therefore not used in determining the least-square conic curves of Slavin et al. (1985). Since comparisons of observations of the terrestrial and Jovian

planets is not an objective for this study, such a reason is not so compelling here. Moreover, the location of the Voyager 1 outbound crossing shown in Figure 1 suggests that its inclusion might significantly reduce the large flare of the least-square curve to the Saturn shock and improve the agreement with both the calculated results and also the shock shapes observed at the other planets. The results presented in Figure 10 show that this expectation is realized to only a limited degree, however, since even the new least-square conic curve flares out beyond the calculated curves by the terminator plane.

Both the original and the new least-square curves are conic sections described in terms of nondimensional cylindrical coordinates X/R_0 , R/R_0 by equations of the form $X = X_0 + r \cos \theta$ and $R = r \sin \theta$, where $r = L / (1 + \epsilon \cos \theta)$, $R_0 = 19.7 \times (2.1 \times 10^{-10} / 3.2 \times 10^{-10})^{1/6} = 18.36$, and θ is the angle measured from the x axis with $\theta = 0$ at the magnetosphere nose. The original curve determined without use of the outbound Voyager 1 observations is defined by $L = 55.4$, $X_0 = 6$, and $\epsilon = 1.71$. The corresponding values for the new curve are $L = 51.8$, $X_0 = 5$, and $\epsilon = 1.39$; and those for the magnetopause are $L = 30.8$, $X_0 = 5$, $\epsilon = 1.09$, and $R_0 = 19.7$. In neither case was any attempt made to eliminate Voyager 2 data on the basis of it being atypical because of Saturn possibly being in the magnetic tail of Jupiter, although it is evident from Figure 1 that elimination of those data would lead to a least-square fitted conic curve that would not only be in improved agreement with our calculated results but with general experience for all the other planets for which such studies have been made. It should be noted that the procedure employed in determining these least-square curves is increasingly

suspect with increasing distance from the nose because no consideration is given in their determination to matching the asymptotic directions of the bow shock. This would not pose a problem if adequate data were available for downstream shock crossings, but that is not the situation for Saturn.

Although the stagnation pressure correction introduced through R_0 accounts for a significant part of the inward location of the Voyager 1 outbound shock location, the overall result is a significant reduction in the amount of flaring at the flanks of the bowshock. Even so, downstream of the terminator plane, the revised least-square conic curve extends outside the location of the calculated shock for an axisymmetric magnetosphere having the same shape as the least-square conic curve representing the low-latitude magnetopause of Saturn. It would appear from these comparisons that magnetospheric flattening for Saturn may be about one-third that for Jupiter, but the differences in the shock locations near the terminator plane require further examination.

Concluding Remarks

The development of a three-dimensional computational model for determining the solution of the gasdynamic portion of the gasdynamic convected magnetic field model for solar wind flow past a magnetopause of nonaxisymmetric shape is described. Specific application of the model is made to Jupiter and Saturn where, as inferred from observations, significant equatorial broadening of the magnetopause cross sections exists. Results from the new three-dimensional model

converge continuously to those calculated previously for axisymmetric magnetoionospheres that were determined using completely different computational procedures, thereby verifying the accuracy of both methods.

Because the cost of determining these three-dimensional solutions is two orders of magnitude greater than for axisymmetric flows, and the differences between the results are small for small departures from axisymmetry, we suggest that the axisymmetric model be used whenever the magnetoionopause cross section is nearly circular, and that the new non-axisymmetric model be employed only for those cases in which substantial departures from axisymmetry exist. Examples of the latter are Jupiter and Saturn, for which previous comparisons between the observations and results calculated for axisymmetric magnetospheres were shown to be in substantially poorer agreement with observations than for the terrestrial planets.

Comparisons of results from the new model for a family of three-dimensional nonaxisymmetric magnetospheres having elliptic cross sections of various eccentricities with the observed magnetopause and bow shock crossings at Jupiter and Saturn, all of which occurred at low latitudes, provide a new means to estimate the amount of equatorial broadening of the magnetospheres of these planets. It is found that essentially perfect agreement with the observations is obtained for Jupiter when a value of 1.75 is used for the ratio a/b of major to minor axes of the cross section. For Saturn, similarly good agreement with the observations is found in the nose region when a value of 1.25 is

used for a/b . Both of these values are in essential agreement with previous estimates of $5/3$ and $4/3$ for a/b based on other considerations.

Near and downstream of the terminator of Saturn, however, the least-square fitted conic curve (Slavin et al., 1985) used to represent the shape of the bow shock flares out considerably more than indicated by any of the model predictions, including that for an axisymmetric magnetopause. In an attempt to gain a better understanding of the reason for this behavior, we have reexamined the fitting procedure applied to the Saturn data and produced a new least-square conic curve that includes the observations of Voyager 1 spacecraft not utilized in the original determination. Those observations were not used in the original determination because the bow shock crossings were too far downstream of the planet to meet criteria set previously in studies of the terrestrial planets. The new curve matches the calculated shape of the bow shock for $a/b = 1.25$ for a greater distance from the nose of the bow shock than the original curve, but also flares out more than the calculated results at and downstream of the terminator. An inescapable conclusion of these comparisons of calculated and observed shock shapes is that the currently available observational data for bow shock crossings at Saturn are too few in number and too scattered to provide a well-defined representation of the shape of the bow shock in the terminator region.

Acknowledgements

This research was jointly supported by NASA Contracts NASW-4135, NASW-4335, NASA Grant NAGW 278, and by Air Force Office of Scientific Research Contract F49620-86-C-0035. CRAY XMP computational time was provided by the Applied Computational Fluids Branch at NASA/Ames Research Center under a Memorandum of Understanding with NASA Headquarters. The authors thank Dr. Ron Lepping of Goddard Space flight Center for helpful comments on the interpretation of shock crossing observations by Voyager and Pioneer spacecraft at Jupiter and Saturn.

References

Abbett, M. J., Boundary condition computational procedures for inviscid supersonic steady flow field calculations, Aerotherm Corp. Report 71-41, 1971.

Beam, R. M. and R. F. Warming, An implicit factored scheme for the compressible Navier-Stokes equations, AIAA Paper 77-645, 1977.

Behannon, K. W., R. P. Lepping and N. F. Ness, Structure and dynamics of Saturn's outer magnetosphere and boundary regions, J. Geophys. Res., 88, 8791-8800, 1983.

Desch, M. D., Radio emission signature of Saturn's immersions in Jupiter's tail. J. Geophys. Res., 88, 6904-6910, 1983.

Engle, I. M. and D. B. Beard, Idealized Jovian magnetosphere shape and field, J. Geophys. Res., Vol. 85, pp. 579-592, 1980.

Fairfield, D. H., Average and unusual locations of the earth's bow shock and magnetopause, J. Geophys. Res., Vol. 86, pp. 6700-6716, 1971.

Grzedzielski, S., W. Macek and P. Oberc, Expected immersion of Saturn's magnetosphere in the Jovian magnetic tail. Nature, 292, 615-616, 1981.

Kutler, P., W. A. Reinhardt and R. F. Warming, Multi-shocked three-dimensional supersonic flow fields with real gas effects, AIAA J., Vol. 11, pp. 657-664, 1973.

Kutler, P., J. A. Pedelty and T. H. Pulliam, Supersonic flow over three-dimensional ablated nosetips using an implicit numerical procedure, AIAA Paper 80-63, 1980.

Pulliam, T. and J. L. Steger, On implicit time-difference simulations of three-dimensional flow, AIAA Paper 78-10, 1978.

Rizk, Y. M., J. N. Scott and R. K. Newman, Numerical simulation of viscous supersonic flows in the vicinity of embedded subsonic or axially separated regions, Vols. I and II, AFWAL-TR-83-3113, 1983.

Russell, C. T., Planetary bow shocks, in Collisionless Shocks in the Heliosphere. Review of Current Research, edited by B. T. Tsurutani and R. G. Stone, pp. 107-130, AGU Geophysical Monograph 35, 1985.

Scarf, F. L., L. A. Frank and R. P. Lepping, Magnetosphere boundary observations along the IMP-7 orbit: Part 1, boundary locations and wave level variations. J. Geophys. Res., 82, 5171-5180, 1977.

Slavin, J. A. and R. E. Holzer, Solar wind flow about terrestrial planets 1. Modeling bow shock position and shape, J. Geophys. Res., Vol. 87, pp. 11401-11418, 1981.

Slavin, J. A., R. E. Holzer, J. R. Spreiter, S. S. Stahara and D. S. Chaussee, Solar wind flow about the terrestrial planets 2. Comparison with gas dynamic theory and implications for solar-planetary interactions. J. Geophys. Res., Vol. 88, pp. 19-35, 1983.

Slavin, J. A., E. J. Smith, J. R. Spreiter and S. S. Stahara, Solar wind flow about the outer planets: gas dynamic modeling of the Jupiter and Saturn bow shocks, J. Geophys. Res., Vol. 90, pp. 6275-6286, 1985.

Spreiter J. R. and B. R. Briggs, Theoretical determination of the form of the boundary of the corpuscular stream produced by interaction with the magnetic dipole field of the earth. J. Geophys. Res., 67, 37-51, 1962.

Spreiter, J. R., A. L. Summers and A. Y. Alksne, Hydromagnetic flow around the magnetosphere, Planet. Space Sci., Vol. 14, pp. 223-253, 1966.

Spreiter, J. R. and S. S. Stahara, A new predictive model for determining solar wind-terrestrial planet interactions, J. Geophys. Res., Vol. 85, pp. 6769-6777, 1980.

Spreiter, J. R. and S. S. Stahara, Solar wind flow past Venus: Theory and comparisons, J. Geophys. Res., Vol. 85, pp. 7715-7738, 1980.

Spreiter, J. R. and S. S. Stahara, Magnetohydrodynamic and gasdynamic theories for planetary bow waves, in Collisionless Shocks in the Heliosphere, Review of Current Research, edited by B. T. Tsurutani and R. G. Stone, pp. 85-107, AGU Geophysical Monograph 35, 1985.

Stahara, S. S., D. Klenke, B. C. Trudinger and J. R. Spreiter, Application of advanced computational procedures for modeling solar-wind interactions with Venus-Theory and computer code, NASA CR-3267, 1980.

Thomas, P. D., M. Vinokur, R. Bastionon and R. J. Conti, Numerical solution for the three-dimensional hypersonic flow field of a blunt body, AIAA J., Vol. 10, pp. 887-894, 1972.

FIGURE TITLES

Figure 1. Locations of the Jupiter and Saturn bow shock and magnetopause crossings observed by Pioneer 10, 11 and Voyager 1, 2 spacecraft (Slavin et al., 1985).

Figure 2. Least-square fitted conic curves representing the observations of the Jovian and Saturnian bow shock and magnetopause in the planetary equatorial plane together with predictions (dashed lines) of the gasdynamic bow shock model for an axisymmetric magnetopause matching the fitted magnetopause curve near the equatorial plane.

Figure 3. A conceptual representation of magnetopause cross sectional shapes based upon observations, theoretical magnetic field models, and gasdynamic modeling results.

Figure 4. Illustration of flow field subdivision and coupled flow solver combination incorporated in the three-dimensional gasdynamic solar wind planetary interaction model.

Figure 5. Perspective cutout view of one quadrant of a typical computational grid employed in the three-dimensional model.

Figure 6. Predicted bow shock and corresponding magnetopause locations in the terminator plane and in the 10 equally-spaced azimuthal planes employed in the three-dimensional model for an equatorially broadened

Jovian magnetopause having an elliptic cross section with $a/b = 1.75$ for $M_{S\infty} = 10$ and $\gamma = 2.0$.

Figure 7. Contours of density, pressure, temperature, velocity magnitude normalized by free stream values, and Mach number in the equatorial and polar meridian planes for the Jovian magnetopause with $a/b = 1.75$, $M_{S\infty} = 10$ and $\gamma = 2.0$.

(a) Noon-midnight polar meridian plane

(b) Equatorial plane

Figure 8. Predicted bow shock and corresponding magnetopause locations in the terminator plane and in the 10 equally-spaced azimuthal planes employed in the three-dimensional model for an equatorially broadened Saturnian magnetopause having an elliptic cross section with $a/b = 1.25$ for $M_{S\infty} = 12$ and $\gamma = 2.0$.

Figure 9. Comparison of a least-square fitted conic curve representing the observational data for the Jovian bow shock in the planetary equatorial plane with three-dimensional bow shock predictions for magnetopause shapes having elliptic cross sections with different ratios a/b of major to minor axes representing various amounts of equatorial broadening for $M_{S\infty} = 10$ and $\gamma = 2.0$.

Figure 10. Comparison of a least-square fitted conic curve representing the observational data for the Saturnian bow shock in the planetary equatorial plane with three-dimensional bow shock predictions for magnetopause shapes having elliptic cross sections with different ratios a/b of major to minor axes representing various amounts of equatorial broadening for $M_{S\infty} = 12$ and $\gamma = 2.0$.

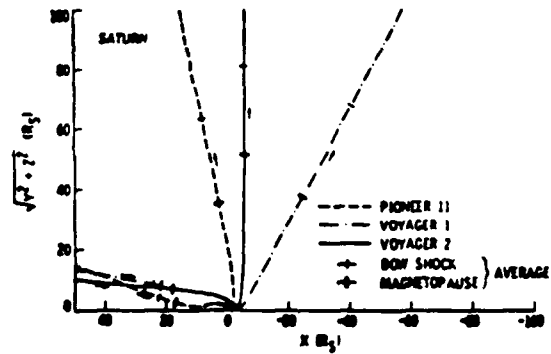
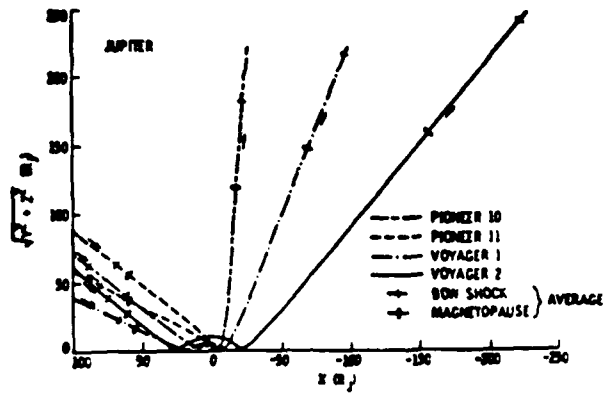


Figure 1. Locations of the Jupiter and Saturn bow shock and magnetopause crossings observed by Pioneer 10, 11 and Voyager 1, 2 spacecraft (Slavin et al., 1985).

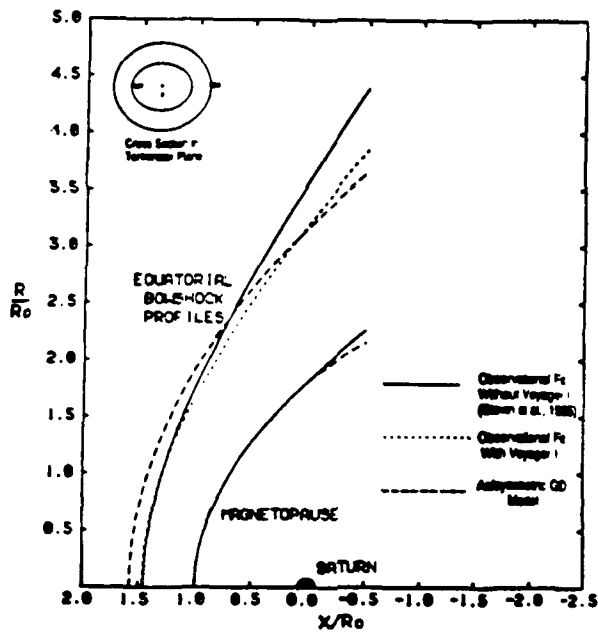
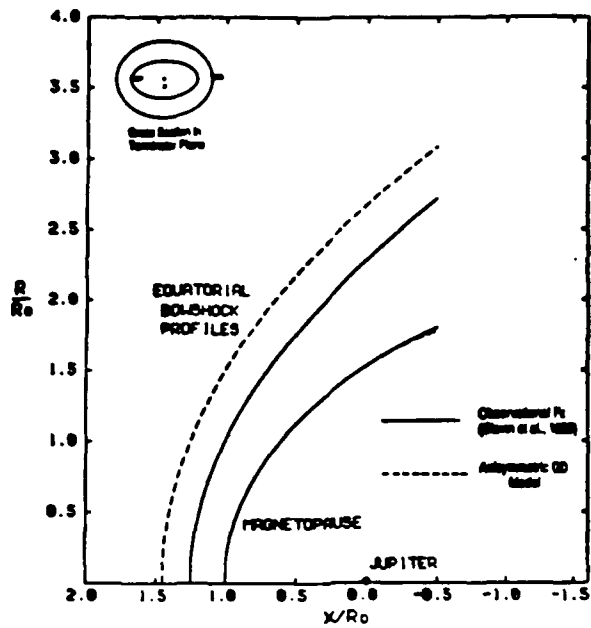


Figure 2. Least-square fitted conic curves representing the observations of the Jovian and Saturnian bow shock and magnetopause in the planetary equatorial plane together with predictions (dashed lines) of the gasdynamic bow shock model for an axisymmetric magnetopause matching the fitted magnetopause curve near the equatorial plane.

Polar Flattening Hierarchy

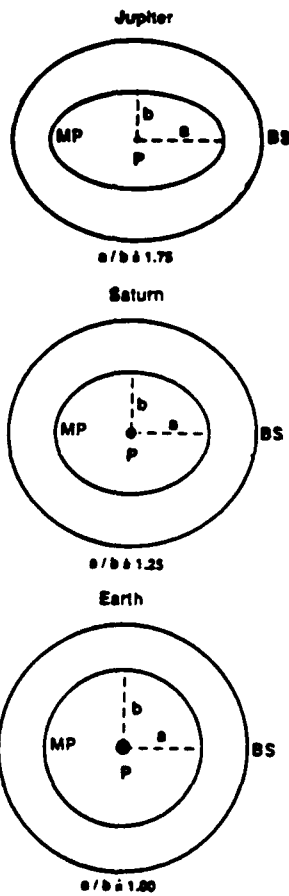


Figure 3. A conceptual representation of magnetopause cross sectional shapes based upon observations, theoretical magnetic field models, and gasdynamic modeling results.

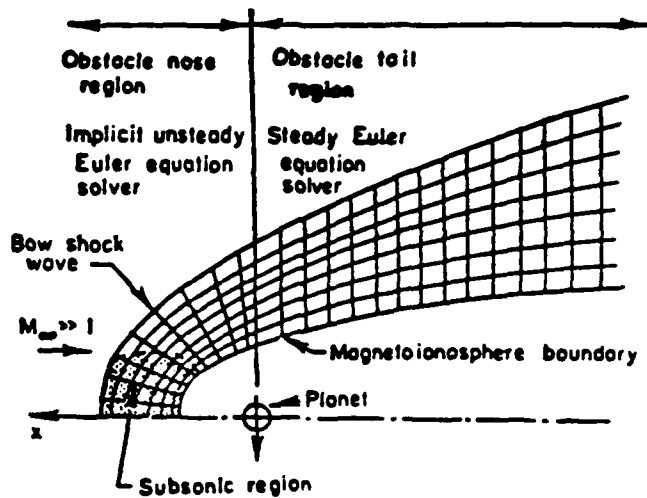


Figure 4. Illustration of flow field subdivision and coupled flow solver combination incorporated in the three-dimensional gasdynamic solar wind planetary interaction model.

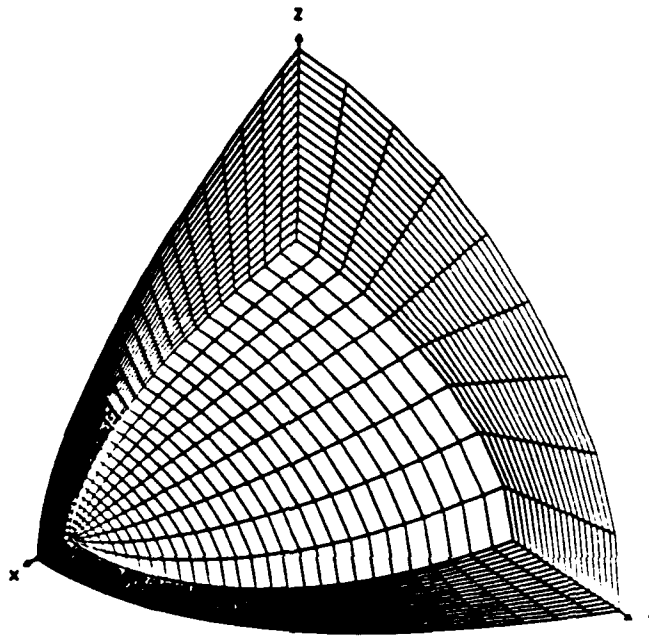


Figure 5. Perspective cutout view of one quadrant of a typical computational grid employed in the three-dimensional model.

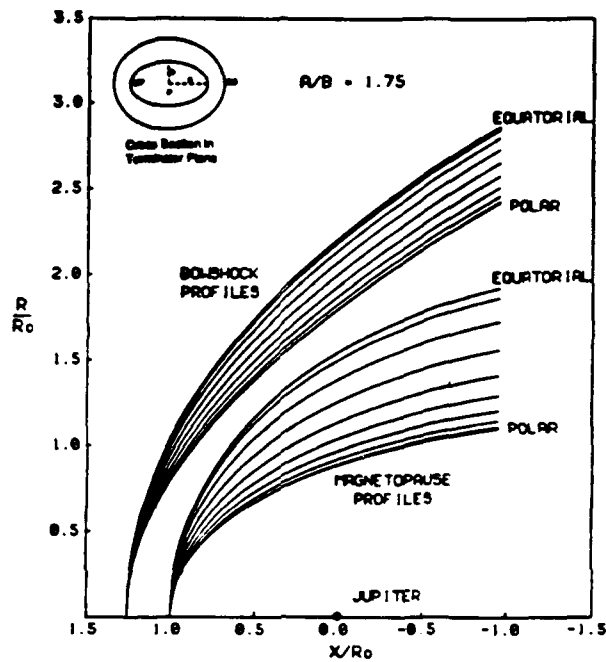
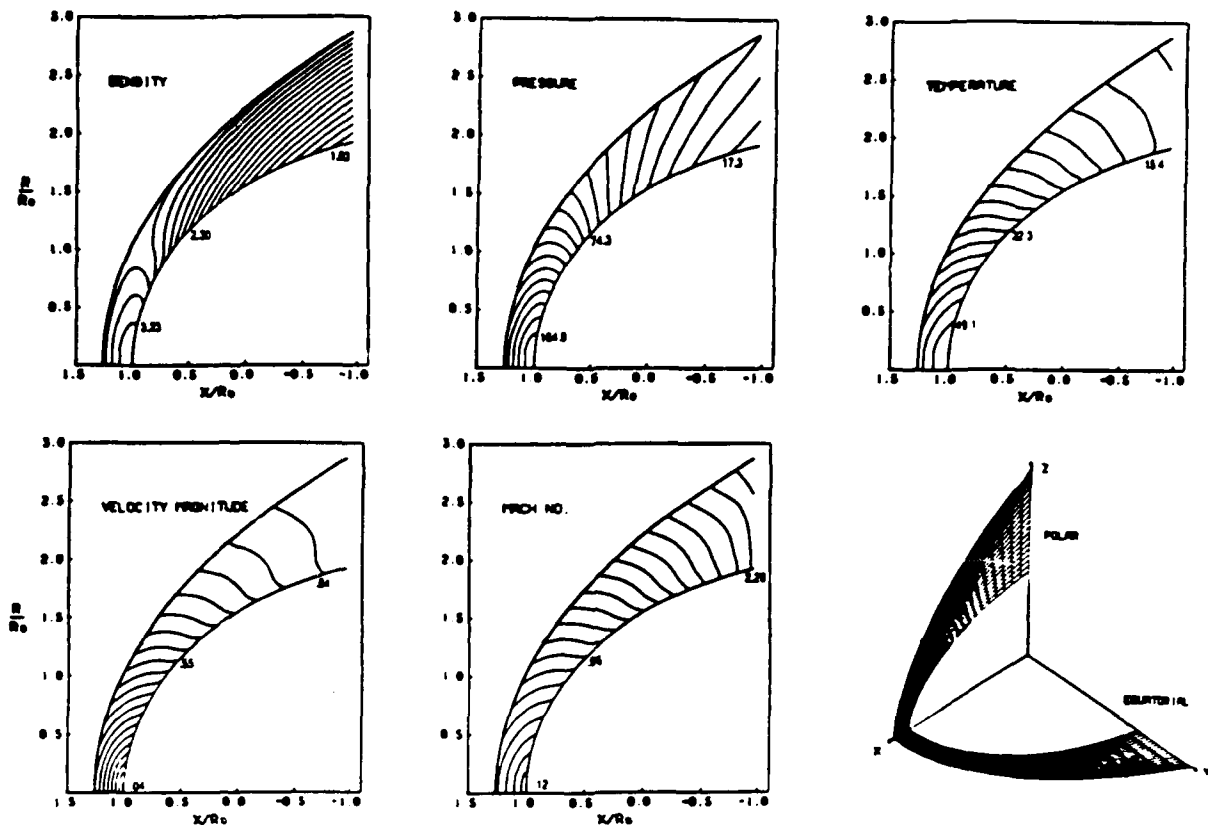
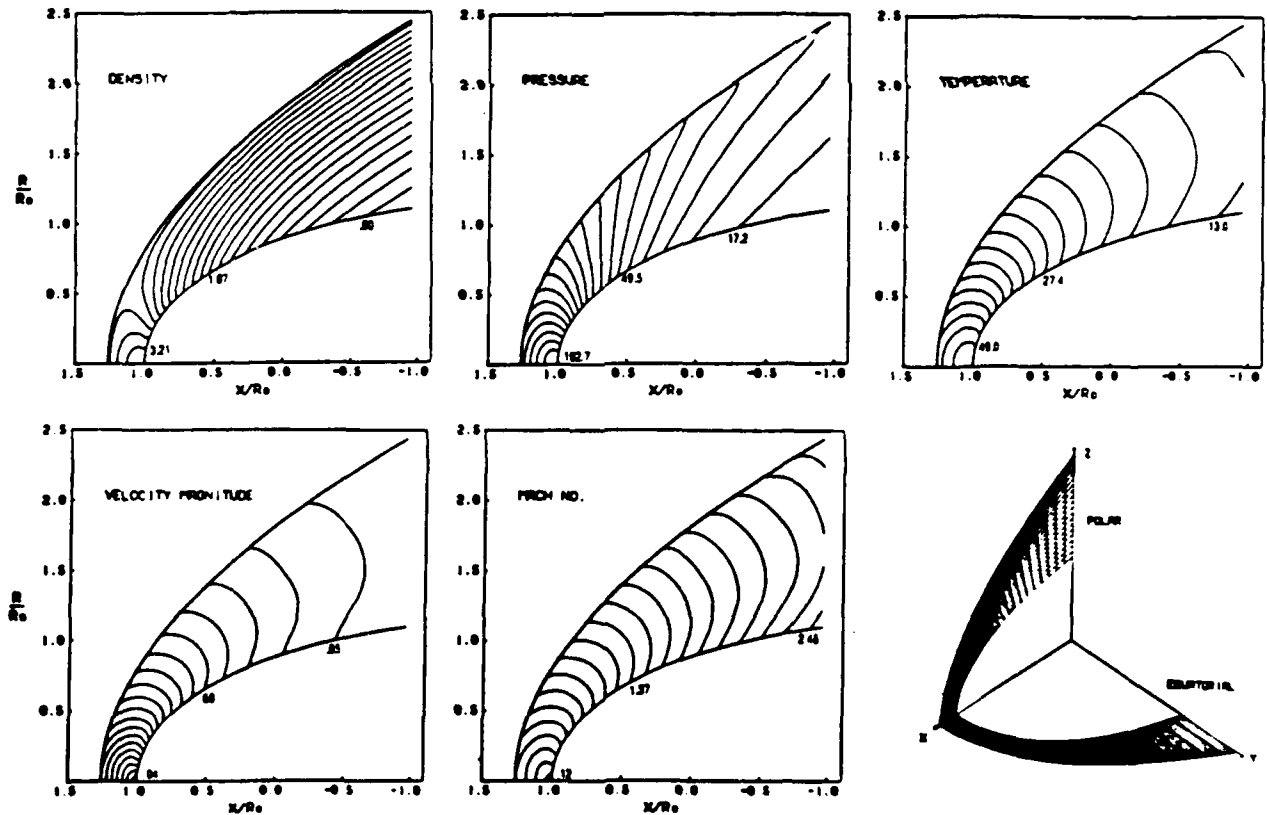


Figure 6. Predicted bow shock and corresponding magnetopause locations in the terminator plane and in the 10 equally-spaced azimuthal planes employed in the three-dimensional model for an equatorially broadened Jovian magnetopause having an elliptic cross section with $a/b = 1.75$ for $M_{S\infty} = 10$ and $\gamma = 2.0$.



(b) Equatorial plane



(a) Noon-midnight polar meridian plane

Figure 7. Contours of density, pressure, temperature, velocity magnitude normalized by free stream values, and Mach number in the equatorial and polar meridian planes for the Jovian magnetopause with $a/b = 1.75$, $M_{S\infty} = 10$ and $\gamma = 2.0$.

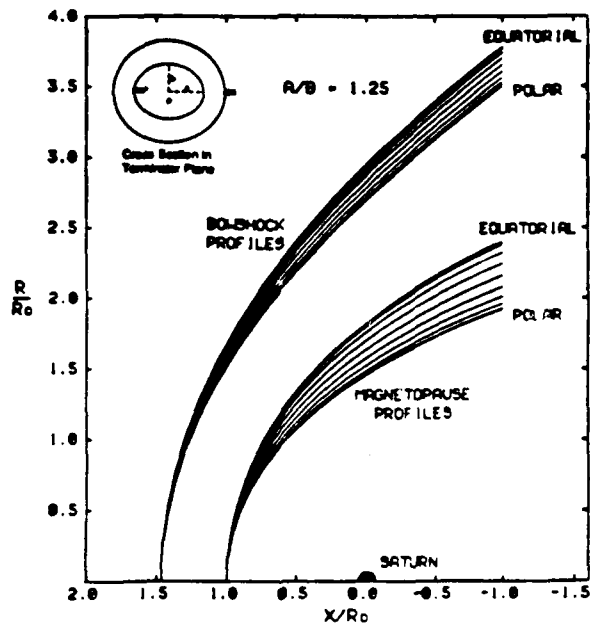


Figure 8. Predicted bow shock and corresponding magnetopause locations in the terminator plane and in the 10 equally-spaced azimuthal planes employed in the three-dimensional model for an equatorially broadened Saturnian magnetopause having an elliptic cross section with $a/b = 1.25$ for $M_{S\infty} = 12$ and $\gamma = 2.0$.

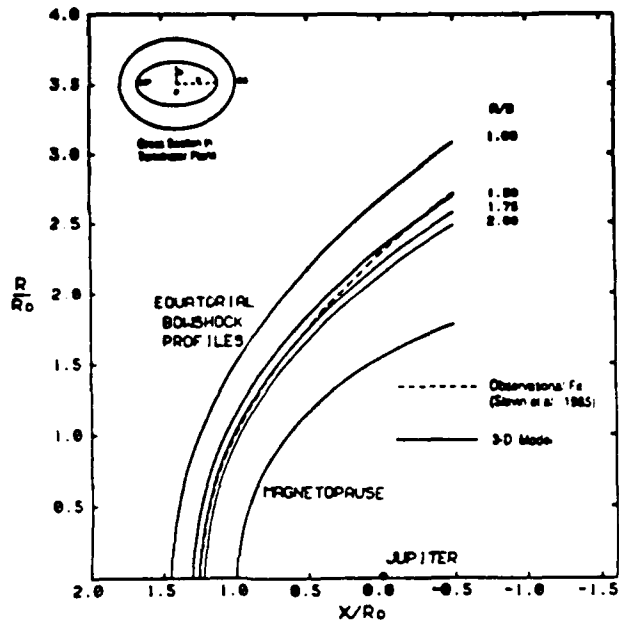


Figure 9. Comparison of a least-square fitted conic curve representing the observational data for the Jovian bow shock in the planetary equatorial plane with three-dimensional bow shock predictions for magnetopause shapes having elliptic cross sections with different ratios a/b of major to minor axes representing various amounts of equatorial broadening for $M_{S\infty} = 10$ and $\gamma = 2.0$.

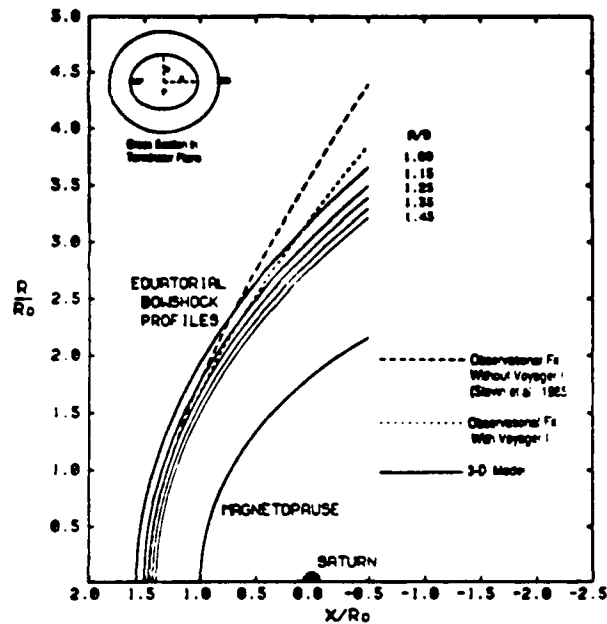


Figure 10. Comparison of a least-square fitted conic curve representing the observational data for the Saturnian bow shock in the planetary equatorial plane with three-dimensional bow shock predictions for magnetopause shapes having elliptic cross sections with different ratios a/b of major to minor axes representing various amounts of equatorial broadening for $M_{S\infty} = 12$ and $\gamma = 2.0$.